

University of Windsor

Scholarship at UWindor

Electronic Theses and Dissertations

Theses, Dissertations, and Major Papers

2011

Experimental Study on Heat Transfer and Flow Characteristics of Air Cooling through Cross-flow Microchannel Heat Exchanger

Engr Sarbadaman Dasgupta
University of Windsor

Follow this and additional works at: <https://scholar.uwindsor.ca/etd>

Recommended Citation

Dasgupta, Engr Sarbadaman, "Experimental Study on Heat Transfer and Flow Characteristics of Air Cooling through Cross-flow Microchannel Heat Exchanger" (2011). *Electronic Theses and Dissertations*. 181.

<https://scholar.uwindsor.ca/etd/181>

This online database contains the full-text of PhD dissertations and Masters' theses of University of Windsor students from 1954 forward. These documents are made available for personal study and research purposes only, in accordance with the Canadian Copyright Act and the Creative Commons license—CC BY-NC-ND (Attribution, Non-Commercial, No Derivative Works). Under this license, works must always be attributed to the copyright holder (original author), cannot be used for any commercial purposes, and may not be altered. Any other use would require the permission of the copyright holder. Students may inquire about withdrawing their dissertation and/or thesis from this database. For additional inquiries, please contact the repository administrator via email (scholarship@uwindsor.ca) or by telephone at 519-253-3000ext. 3208.

Experimental Study on Heat Transfer and Flow Characteristics of Air Cooling through
Cross-flow Microchannel Heat Exchanger

by

Engr Sarbadaman Dasgupta

A Thesis
Submitted to the Faculty of Graduate Studies
through Mechanical Engineering
in Partial Fulfillment of the Requirements for
the Degree of Master of Applied Science at the
University of Windsor

Windsor, Ontario, Canada

2011

© 2011 Engr Sarbadaman Dasgupta

Experimental Study on Heat Transfer and Flow Characteristics of Air Cooling through
Cross-flow Microchannel Heat Exchanger

by

Engr Sarbadaman Dasgupta

APPROVED BY:

Dr. Reza Riahi, Outside Program Reader
Department of Mechanical, Automotive, and Materials Engineering

Dr. Gary W. Rankin, Inside Program Reader
Department of Mechanical, Automotive, and Materials Engineering

Dr. Amir Fartaj, Advisor
Department of Mechanical, Automotive, and Materials Engineering

Dr. Jennifer Johrendt, Chair of Defense
Department of Mechanical, Automotive, and Materials Engineering

June 27, 2011

DECLARATION OF ORIGINALITY

I hereby certify that I am the sole author of this thesis and that no part of this thesis has been published or submitted for publication.

I certify that, to the best of my knowledge, my thesis does not infringe upon anyone's copyright nor violate any proprietary rights and that any ideas, techniques, quotations, or any other material from the work of other people included in my thesis, published or otherwise, are fully acknowledged in accordance with the standard referencing practices. Furthermore, to the extent that I have included copyrighted material that surpasses the bounds of fair dealing within the meaning of the Canada Copyright Act, I certify that I have obtained a written permission from the copyright owner(s) to include such material(s) in my thesis and have included copies of such copyright clearances to my appendix.

I declare that this is a true copy of my thesis, including any final revisions, as approved by my thesis committee and the Graduate Studies office, and that this thesis has not been submitted for a higher degree to any other University or Institution.

ABSTRACT

Air-side heat transfer and flow characteristics were studied through an air-to-deionized water cross-flow serpentine microchannel heat exchanger during air cooling. In the single phase, twenty distinct operating conditions were maintained within the range of air and deionized water-side Reynolds number $283 \leq Re_a \leq 1384$ and $105 \leq Re_w \leq 159$ respectively, retaining the constant inlet temperatures of both fluids ($T_{a,i} = 38 \pm 0.5^\circ\text{C}$ and $T_{w,i} = 9 \pm 0.5^\circ\text{C}$). Heat transfer and fluid flow key parameters were evaluated from experimental data. Heat balance performance was observed within 4% throughout the experiment, and major thermal resistance was found in the air-side, ranging from 89% - 94% of overall thermal resistance. The effects of Re_w and Re_a on air-side Nusselt number (Nu_a), Colburn factor (j_a), friction factor (f_a), and other parameters were examined, and general correlations were achieved. The Nu_a - Re_a - Pr_a relationship of the current study is compared to other correlations, and several recommendations are proposed.

DEDICATION

Dedicated to

My Parents:

Father: Late Advocate Dwijabar Dasgupta, M. A. B.Ed. L.L.B.

Mother: Bithika Dasgupta

They are the source of my all inspiration and strength.

ACKNOWLEDGEMENTS

Firstly, I would like to convey my heartfelt gratitude to my supervisor Dr. Amir Fartaj for giving me the opportunity to perform this study. His continuous patience, motivation, enthusiasm, support, advice, and diligent supervision were key factors in its completion. His wide knowledge, understanding, encouragement and personal guidance have helped me to be successful.

I am grateful to my other committee members, Dr. Gary W. Rankin and Dr. Ahmadrza Riahi, for their encouragement, insightful comments, and advice. Dr. Gary W. Rankin's course lectures and advice helped me in estimating the experimental uncertainties for this study.

I wish to express my warm and sincere thanks to Mr. Mesbah G. Khan for the installation and commissioning of the present experimental setup; his good advice and demonstrations were of great value in helping me to carry out the experiment. I am deeply indebted to Faisal A. Siddique for sharing his technical and theoretical knowledge on experimental works. I also wish to thank all of my colleagues: Serena-Al-Obaidi, Abdul Quaiyum, Mohammed Saadi, Mohammed Ismail, and Shahram Fotwat for their assistance and co-operation during experiment.

I would like to extend my thanks to Ms. Rose Gignac and Ms. Barbara Tattersall for their secretarial services, Mr. Andrew Jenner for technical support and services, and the Mechanical Department for GA opportunity.

Lastly, I offer my love and blessings to my wife Lipika, daughter Joyoty, and son Sommojoty for their inspiration, continued support, and encouragement for my research work.

TABLE OF CONTENTS

DECLARATION OF ORIGINALITY	iii
ABSTRACT	iv
DEDICATION	v
ACKNOWLEDGEMENTS	vi
LIST OF ORIGINAL PUBLICATIONS AND PRESENTATION	xi
LIST OF TABLES	xiii
LIST OF FIGURES	xiv
NOMENCLATURE	xvi
CHAPTER	
I INTRODUCTION	1
1.1 Motivation.....	2
1.2 Objectives	5
II REVIEW OF LITERATURE	6
2.1 Fluid flow and heat transfer characteristics of MCHX.....	8
2.2 Air-side flow and heat transfer characteristics of MCHX	9
2.3 Air –side flow and heat transfer characteristics of CHX	10
2.3.1 Data reduction method.....	10
2.3.2 The effect of tube rows, fin geometry and tube diameter	11
2.3.3 Correlations and comparison	12
2.4 The effect of tube row arrangements on heat transfer	13
2.5 Scope of the current study	15
III EXPERIMENTAL SETUP AND OPERATIONAL PROCEDURE	17
3.1 Experimental setup	17
3.1.1 Air handling system	18
3.1.2 Test chamber and MCHX core	18
3.1.3 Liquid circulation system	22
3.1.4 Data acquisition system	23
3.2 Experimental methodology and operating conditions	24
3.3 Data collection for different parameters	25

	3.3.1 Air-side measurements	26
	3.3.2 Deionized water-side measurements	30
IV	THEORETICAL CONSIDERATIONS AND DATA REDUCTION	32
	4.1 Interest of key parameters.....	32
	4.2 Assumptions for current study.....	35
	4.3 Data reduction and analysis	36
	4.3.1 Deionized water-side parameters evaluation	37
	4.3.2 Overall MCHX's parameters evaluation	38
	4.3.3 Air-side parameters evaluation	39
V	RESULTS AND DISCUSSIONS	42
	5.1 Heat transfer characteristics.....	43
	5.1.1 Heat transfer energy balance	43
	5.1.2 Effect of Reynolds number on heat transfer rate	45
	5.1.2.1 Comparison to the heat transfer correlation with experimental data	47
	5.1.3 Effect of Reynolds number on Nusselt number.....	48
	5.1.3.1 Comparison to the Nusselt number –Reynolds number correlation with data.....	49
	5.1.3.2 Comparison of Nusselt number-Reynolds number-Prandtl number with others.....	50
	5.1.4 Effect of Reynolds number on Colburn factor	53
	5.2 Fluid flow analysis.....	55
	5.2.1 Effect of Reynolds number on air-side pressure drop	55
	5.2.2 Effect of Reynolds number on friction factor.....	56
	5.3 MCHX performance characteristics	58
	5.3.1 Effect of Reynolds number on overall thermal resistance	58
	5.3.2 Effect of Reynolds number on effectiveness	60
	5.3.3 Effect of Reynolds number on NTU.....	62
	5.3.4 Effective-NTU relationship	64
VI	CONCLUSIONS AND RECOMMENDATIONS	66
	6.1 Conclusions.....	66
	6.2 Recommendations.....	66
	APPENDIX-A.....	72
	EXPERIMENTAL UNCERTAINTY ANALYSIS.....	72
	A.1 Uncertainty analysis methodology.....	72

A.1.1 Uncertainty analysis for independent parameters	73
A.1.2 Uncertainty analysis for dependent parameters	74
A.2 Uncertainties of key dimensional parameters	74
A.2.1 Uncertainty estimation for air-side hydraulic diameter	75
A.3 Uncertainties estimation for one operating conditions	76
A.3.1.1 Uncertainty estimation for air inlet temperature.....	78
A.3.1.2 Uncertainty estimation for air outlet temperature.....	81
A.3.1.3 Uncertainty estimation for air-side pressure drop.....	83
A.3.1.4 Uncertainty estimation for air velocity	85
A.3.1.5 Uncertainties estimation for thermophysical properties of air	85
A.3.1.6 Uncertainty estimation for air mass flow rate.....	86
A.3.1.7 Uncertainty estimation for air-side Reynolds number	87
A.3.1.8 Uncertainty estimation for air-side heat transfer rate	88
A.3.1.9 Uncertainty estimation for air-side Prandtl number	89
A.3.2.1 Uncertainty estimation for water inlet temperature	89
A.3.2.2 Uncertainty estimation for water outlet temperature	91
A.3.2.3 Uncertainty estimation for thermophysical properties of water.....	93
A.3.2.4 Uncertainty estimation for water mass flow rate	94
A.3.2.5 Uncertainty estimation for water-side heat transfer rate.....	94
A.3.2.6 Uncertainty estimation for water-side Reynolds number	95
A.3.2.7 Uncertainty estimation for water-side Prandtl number.....	96
A.3.2.8 Uncertainty estimation for deionized water-side Peclet number.....	97
A.3.2.9 Uncertainty estimation for water-side Nusselt number	97
A.3.2.10 Uncertainty estimation for water-side heat transfer coefficient.....	98
A.3.2.11 Uncertainty estimation for deionized water-side thermal resistance	99
A.3.3.1 Uncertainty estimation for LMTD	99
A.3.3.2 Uncertainty estimation for average heat transfer rate	101
A.3.3.3 Uncertainty estimation for overall thermal resistance	102
A.3.3.4 Uncertainty estimation for effectiveness	102
A.3.3.5 Uncertainty estimation for NTU	103
A.3.4.1 Uncertainty estimation for air-side heat transfer coefficient	104
A.3.4.2 Uncertainty estimation for air-side Nusselt number	105

A.3.4.3 Uncertainty estimation for air-side Stanton number.....	105
A.3.4.4 Uncertainty estimation for air-side Colburn factor.....	107
A.3.4.5 Uncertainty estimation for air-side friction factor	107
A.4 Overall uncertainties range for all operating conditions.....	109
REFERENCES	111
VITA AUCTORIS	117

LIST OF ORIGINAL PUBLICATIONS AND PRESENTATION

Some of the methodologies, procedures and observations in the experiment of the current study are disseminated and documented in the following journal and conference publications and presentations:

Dasgupta, E. S., Siddiqui, F.A. and Fartaj, A.2011. Experimental study on air side heat transfer & fluid flow characteristics of microchannel heat exchanger. SAE International Journal of Materials and Manufacturing, Vol. 4, pp.1198-1210, doi:10.4271 /2011-01-1166.

Dasgupta, E. S., Siddiqui, F.A. and Fartaj, A. 2011. Experimental study on air side heat transfer & fluid flow characteristics of microchannel heat exchanger. Published by the Society of the Automotive Engineers Inc.PA, DOI: 10.4271/2011-01-1166. (Originally presented at the SAE 2011 World Congress, April 14, 2011 Detroit, MI, USA, SAE Paper # 2011-01-1166.

Dasgupta, E. S., Siddiqui, F.A., Quaiyum, A., Serena Al-Obaidi, S. and Fartaj, A. 2011. Experimental Study on Air Cooling via a Multiport Mesochannel Cross-Flow Heat Exchanger. ASME 9th International Conference on Nanochannels, Microchannels, and Minichannels (ICNMM), Paper # ICNMM2011-58257, Edmonton, Alberta, CANADA, June 19-22, 2011.

Siddiqui, F.A., **Dasgupta, E. S.** and Fartaj, A. 2011. Experimental investigation of air-side heat transfer and fluid flow performances of multi-port serpentine crossflow mesochannel heat exchanger. Int. Journal of Heat and Fluid Flow (under review), Paper # HFF – D-11- 00055.

Serena Al-Obaidi, Fartaj, A., **Dasgupta, E. S.** and Quaiyum, A.2011. Second Law Analysis of a Multiport Serpentine Microchannel Heat Exchanger. Int. Journal of Exergy (under review), Paper #26300.

LIST OF TABLES

2.1	Mehendale et al. (1999) channel classification scheme	6
2.2	Kandlinkar et al. (2006) channel classification scheme	6
3.1a	Specifications of microchannel heat exchanger core (liquid side)	21
3.1b	Specifications of microchannel heat exchanger core (air-side)	22
3.2	Operating conditions	25
3.3	Differential pressure transducer for air-side	30
5.1	Coefficients of determination, curve fit coefficients of Fig.5.2	45
5.2	Coefficients of determination, curve fit coefficients of Fig.5.4	49
A.1	Uncertainties of key dimensional parameters	75
A.2	The mean value of parameters at one operating condition	76
A.3	Overall experimental uncertainty	110

LIST OF FIGURES

2.1	(a) Microchannel slab (b) Inline tube bank arrangement	15
3.1	The schematic diagram of experimental setup	17
3.2	Test chamber	19
3.3	Microchannel heat exchanger core	20
3.4	Single microchannel heat exchanger slab	21
3.5	Air inlet thermocouple grid	27
3.6	Air inlet thermocouple grid	28
3.7	Air inlet temperature profile	29
3.8	Air outlet temperature profile	29
5.1	Heat balance	44
5.2	The effect of Re_a and Re_w on heat transfer rate (\dot{Q})	46
5.3	Comparison to $\dot{Q} - Re_a$ correlation with experimental data	47
5.4	The effect of Re_a and Re_w on air-side Nusselt number (Nu_a)	48
5.5	Comparison to $Nu_a - Re_a$ correlation with experimental data	50
5.6	Comparison to $Nu_a - Re_a - Pr_a$ correlation with experimental data	52
5.7	The effect of Re_a and Re_w on air-side Colburn factor (j_a)	53
5.8	Comparison to $j_a - Re_a$ correlation with experimental data	54
5.9	The effect of Re_a and Re_w on air-side pressure drop (ΔP_a)	56
5.10	The effect of Re_a and Re_w on air-side friction factor (f_a)	57
5.11	Comparison to $f_a - Re_a$ correlation with experimental data	58
5.12	The effect of Re_a and Re_w on overall thermal resistance (R_{Total})	59
5.13	Comparison to $R_{Total} - Re_a$ correlation with experimental data	60

5.14	The effect of Re_a and Re_w on effectiveness (ϵ)	61
5.15	Comparison to ϵ - Re_a correlation with experimental data	62
5.16	The effect of Re_a and Re_w on NTU	63
5.17	Comparison to NTU- Re_a correlation with experimental data	64
5.18	The effect of NTU on effectiveness	65

NOMENCLATURE

A	Area, m ²
A _a	Total heat transfer area on the air-side, m ²
A _f	Fin surface area, m ²
A _{fr,a}	Frontal area on the air-side, m ²
A _{min,a}	Minimum free flow area on the air-side, m ²
COMHX	Compact heat exchanger
c _p	Specific heat capacity at constant pressure, J/kg.°C
d	Diameter of the tube, m
D _{h,a}	Air-side hydraulic diameter, m
D _{h,w}	Water-side hydraulic diameter, m
F	LMTD Correction factor for multi-pass cross-flow heat exchanger
f	Fanning friction factor
G _a	Air-side mass velocity, kg/s.m ²
HEX	Heat exchanger
h _a	Air-side heat transfer coefficient, W/m.°C
h _w	Liquid side heat transfer coefficient, W/m.°C
j	Colburn factor
k	Thermal conductivity, W/m.°C
L	Flow Length, m
ΔT _{lm,cf}	Log mean temperature difference for counter-flow, °C
\dot{m}_a	Mass flow rate of air, kg/s
\dot{m}_w	Mass flow rate of deionized water, kg/s

max	Maximum
MCHX	Microchannel heat exchanger
min	Minimum
NTU	Number of transfer unit
Nu	Nusselt number
P	Temperature effectiveness
P	Pressure, Pa
Pr	Prandtl number
\dot{Q}	Heat transfer rate, W
Re	Reynolds number
St	Stanton number
T	Temperature, °C
U	Overall heat transfer coefficient, W/m ² . °C
V	Frontal velocity

GREEK SYMBOLS

ΔP	Pressure difference, Pa
δ	Thickness, m
ε	Effectiveness
η	Efficiency
μ	Fluid dynamic viscosity, kg/m.s
ρ	Density, kg/m ³

SUBSCRIPTS

a	air-side
f	fin
in	Inlet
i	Tube inside
l	Liquid side
o	Tube outside
out	Outlet or exit

CHAPTER I

INTRODUCTION

Modern civilization is very concerned about two key issues: energy and environment. ‘Energy’ plays a significant role in modern civilization, steering all sorts of activities. Energy exists in the various forms: solar energy, gravitational potential energy, nuclear energy, heat energy, and so on. We use energy directly and benefit from the numerous products and services that are produced or processed through the use of energy. Energy can be converted from one form to another. Energy conversion, transmission, and utilization are essential for engineering applications such as power generation, process industries, manufacturing plants, automotive industries, HVAC fields, and other areas.

Heat transfer is the most common phenomenon in many practical applications in energy conversion, transmission, and utilization. Heat transfer is the transfer of energy across a system boundary caused by a temperature difference. The device that performs the heat transfer is called a ‘heat exchanger’. Heat exchangers play a very important role in energy conversion, transmission, and utilization. Energy efficient heat exchangers can save a significant amount of energy by improving power conversion efficiency; this can lead to reductions in the size, cost and greenhouse gas emissions. Energy consumption by the HVAC sector in most industrialized countries accounts for one-third of total energy consumption (Li-Zhi Zhang, 2008). Research is being conducted throughout the world with a view to providing energy efficient, compact, and inexpensive heat exchangers. A heat exchanger consists of heat transfer elements such as a core or a matrix containing the heat transfer area, and fluid distribution elements such as headers, manifolds, tanks, nozzles, or pipes. The surface area, which is in direct contact with both fluids, is called

the primary or direct surface. The extended surface area is called the extended, secondary, or indirect surface (Shah and Sekulić, 2003). Heat exchangers can be classified in many ways: by geometric configuration of the heat transfer surface, flow arrangement, and other considerations.

Two considerations are always taken into account, in addition to other factors, in heat exchanger design: compactness and heat transfer rate. Conventional compact heat exchangers having an area density of about $700\text{m}^2/\text{m}^3$ are prepared by extending the heat transfer area, but extension of the heating surface area is limited. As such, it does not meet increasing heat transfer demands very effectively. Over the years, a lot of research has been conducted proposing numerous suggestions for increasing the heat transfer rate. Tuckerman and Pease (1981) introduced a microchannel heat sink for removal of heat from integrated circuits. Narrow flow passages, especially micro or meso scale, have been popular among researchers in recent decades. As $\text{Nu} = hD_h/k_f$, for fully developed laminar flow in duct with a constant cross-sectional area, an increase in 'h' can be achieved by reducing D_h (microchannels) or increasing the thermal conductivity of fluid, k_f (nanofluids, higher thermal conductivity than base fluids). But nanofluids are very costly and are hazardous. Reducing the hydraulic diameter (D_h) is a possible means of increasing the heat transfer coefficient (h value). Thus, microchannel ($D_h \leq 1\text{mm}$) is considered to be a promising technology in the heat exchanger field. Modern manufacturing industries are capable of producing microchannels to facilitate the mass production of microchannel heat exchangers. Microchannel heat exchangers have achieved great attention in the research field due to their much higher area density, lower fluid quantity, very compact size, and higher heat transfer rate and energy efficiency.

Cross-flow heat exchangers are categorized under the flow arrangement classification, and they are used extensively in the industry as liquid-to-air heat exchangers; examples are automotive radiators, heater cores, condensers and evaporators of HVAC systems, aircraft oil coolers, unit air heaters, intercoolers of compressors, among others. Heat transfer rates per unit surface area of air-side in cross-flow heat exchangers are always low compared to the rates of the liquid side due to the low thermal conductivity of air (relative to most liquids), so large area density is expected on the air-side (Kays and London, 1984). As such, secondary surface areas are increased to achieve greater surface area density on the air-side. However, the thermal resistance of the air-side usually overrules the entire thermal resistance. In the present study, the air-side fluid flow and heat transfer characteristics of crossflow (air to deionized water) of microchannel heat exchangers were investigated experimentally. Cold deionized water at $9 \pm 0.5^\circ\text{C}$ was passed through microchannels while hot air at $38 \pm 0.5^\circ\text{C}$ was forced to flow through finned passages of the heat exchanger core to cool it.

1.1 Motivation

Sources of energy are not infinite, and ever-increasing energy demands are contributing to its scarcity. Thus, researchers and scientists are trying to develop energy efficient heat exchangers. Space constraints are another key issue in many industrial applications. Removal of heat from high heat flux generating surfaces, such as those found in microelectronics, is becoming a challenge. Compact heat exchangers consisting of microchannel flow passages can confront such requirements for their elevated heat transfer characteristics. Motivating considerations for this research were as follows:

- Microchannel heat exchangers are efficient and compact
- Higher heat transfer coefficients are expected for greater convection heat transfer
- The area density (surface area to volume ratio) is more than that of conventional heat exchangers, leading to higher volumetric heat flux
- Higher heat transfer coefficient and greater volumetric heat flux make it possible to build small size, low weight, and low fluid inventory heat exchangers with the same heat transfer functions
- Such heat exchangers can be replaced by conventional heat exchangers such as automotive radiators, HVAC condensers, evaporators, economisers, etc.
- Such heat exchangers can yield significant savings on energy, space, and cost
- Low heat exchange loss leads to low energy consumption, which will contribute to keeping the environment healthy

1.2 Objectives

Generally, the thermal resistance of the air-side is the major part of the total thermal resistance of the air-to-water cross-flow heat exchanger, and it plays the leading role in the performance of heat exchangers. The objectives of the present study are to investigate the air-side heat transfer and fluid flow characteristics of microchannel heat exchanger (MCHX). The heat transfer correlation of the current study is compared to available correlations. The following are the objectives for this study:

- To evaluate the key parameters of heat transfer and fluid flow, including the heat transfer coefficient, Nusselt number, Stanton number, Colburn factor, Reynolds number, friction factor, effectiveness, and NTU
- To examine the effect of the air-side Reynolds number on heat transfer and fluid flow key parameters
- To obtain the general correlations of air-side heat transfer and fluid flow
- To compare the $Nu_a-Re_a-Pr_a$ correlations of the current study to such correlations that are available in the literature

CHAPTER II

REVIEW OF LITERATURE

Heat exchanger is one of the most important devices in many engineering applications. From the last couple of decades, an extensive studies as well as experiments conducted on compact heat exchangers containing of narrow size flow passages. Mehendale et al. (1999) proposed the channel classification scheme which is extensively used in these areas (Table 2.1).

Table 2.1: Mehendale et al. (1999) channel classification scheme

Microchannels	1-100 μm
Meso-channel	100 μm -1mm
Compact passages	1-6 mm
Conventional passages	> 6 mm

Kandlinkar et al. (2006) also introduced the channel classification scheme (Table 2.2).

Table 2.2: Kandlinkar et al. (2006) channel classification scheme

Conventional passages	> 3 mm
Minichannels	3 mm $\geq D \geq 200 \mu\text{m}$
Microchannels	200 $\mu\text{m} \geq D \geq 10 \mu\text{m}$
Transitional Microchannels	10 $\mu\text{m} \geq D \geq 1 \mu\text{m}$
Transitional Nanochannels	1 $\mu\text{m} \geq D \geq 0.1 \mu\text{m}$
Nanochannels	0.1 $\mu\text{m} \geq D$

Scientists and researchers have been looking at energy efficient compact heat exchangers for quite some time. Heat exchangers containing narrow flow passages such as microchannels have attracted much researcher due to its elevated heat transfer

characteristics. Tuckerman and Pease (1981) introduced the concept of microchannel flow passage to remove the heat from the silicon integrated circuits. Consequently numerous studies were performed to investigate the heat transfer and flow behaviors in microchannel flow passages. Owhaib and Palm (2004) investigated experimentally single phase convective heat transfer in circular microchannels. Steinke and Kandlikar (2004) reviewed the different likely techniques to augment heat transfer in microchannels. Morini (2004) reviewed the different researcher's experimental results on single phase convective heat transfer in microchannels. Hetsroni et al. (2005) compared the heat transfer in microchannels among experimental results with theory and numerical results with different microchannel geometries. Harris et al. (2000) designed a crossflow micro heat exchanger to expedite the heat transfer from liquid to gas which could be the utilizable in a wide range of applications especially in the areas of automotive, home heating and aerospace. Kandlikar et al. (2006) provided well information on multiphase fluid flow and heat transfer characteristics in microchannels. The main advantages of microchannel heat exchangers compared to conventional compact heat exchangers with same heat transfer duty are: 1) smaller size, 2) lighter weight, 3) larger heat transfer area density (m^2/m^3), 4) lower fluid quantity, 5) higher heat transfer coefficient and 6) energy efficiency. All these features are lucrative for designing the heat exchangers in engineering applications such as automotive radiators, heater cores, HVAC condensers and evaporators. Microchannel heat exchangers will be the potential candidate for future HVAC and automotive heat exchangers which will save the size, weight, cost and energy significantly.

Air is commonly used with water or other liquid in the compact heat exchangers in crossflow orientation. A good number of literatures are available for flow & heat transfer characteristics in liquid side of crossflow compact heat exchangers especially for microchannel heat exchangers, but air-side flow & heat transfer characteristics for microchannel heat exchangers are rare in open literature. Some literatures spotlighting on air-side characteristics are available for conventional compact heat exchangers. It has been focused in the available literatures that flow behaviors and heat transfer characteristics in the air-side of crossflow compact heat exchangers are influenced mainly by extended surface geometry, temperature gradient, and mass velocity. However, brief reviews of some available relevant literatures are mentioned below:

2.1 Fluid flow and heat transfer characteristics of MCHX

Experimental & numerical investigations on fluid flow and heat transfer characteristics especially in liquid side of microchannel heat exchangers are reported in several literatures. Cao et al. (2010) investigated thermal performance of crossflow Microchannel Heat Exchangers experimentally. They used deionized water and air as working fluid and passing hot air on the other side of the exchanger. They found volumetric heat transfer coefficient $11.1\text{MW/m}^3\cdot\text{K}$ corresponding pressure drop $< 6\text{ kPa}$ and Reynolds number ~ 64 , when DI is used as working fluid, and volumetric heat transfer coefficient $0.67\text{MW/m}^3\cdot\text{K}$ corresponding pressure drop $\sim 30\text{ kPa}$ and Reynolds number ≈ 1026 , when air is used as working fluid. They also provided correlations for average Nu and Re as well as compared it with other researcher's results. Qi et al. (2009) proposed two retrofitted compact and high efficient microchannel heat exchangers for mobile air conditioning system, and they compared it experimentally with two used base

line heat exchangers. The advantages of proposed microchannel heat exchangers were: a) compactness (17.2% and 15.1% volume reduction for evaporator and condenser, respectively), b) weight (2.8% and 14.9% lighter for evaporator and condenser, respectively) and c) cooling capacity and COP increasing about 5% and 8% respectively under high vehicle speed. Khan et al. (2010) investigated experimentally the pressure drop and friction factors as well as their relations corresponding with Reynolds numbers of flowing fluid (50% Ethylene glycol & 50% water mixture) through the multi-port straight microchannel test slab. Experimental results indicated that Δp follows a linear variation with lower value of Re, and it varies non-linearly with higher Re (>700). The experimental average Poiseuille number ($f.Re$) is about 5% above the theoretical value ($f.Re = 64$, in laminar flow regime) within the range $380 \leq Re \leq 1650$. Jokar et al. (2010) experimentally studied the single phase fluid flow & heat transfer behaviors in meso-channel heat exchangers by flowing fifty percent glycol-water mixture through meso-channels while air is passing on the others side of heat exchanger. They founded that correlations for conventional flow passages do not properly match with their obtained experimental results.

2.2 Air-side flow and heat transfer characteristics of MCHX

Li et al. (2011) investigated on air-side thermal hydraulic performance of an integrated fin flat tube aluminum microchannel heat exchanger experimentally. They used 11 heat exchanger samples with different flow depth, fin height, fin pitch and fin thickness. The air-sides general correlations for j and f factor were proposed as well as compared with that of the multi-louver fin and wavy fin conventional heat exchangers.

2.3 Air-side flow and heat transfer characteristics of CHX

A lot of researchers studied the air-side performances of compact heat exchangers with extended surfaces in experimentally as well as numerically. Reviews of some of such type of literature are given here.

2.3.1 Data reduction method

CC Wang (2000) presented the air-side side performance of fin and tube heat exchangers with various fin geometry including the data reduction method and correlations. Wang et al. (2000) focused on data reduction method to evaluate the air-side heat transfer and fluid flow characteristics of fin-and-tube heat exchangers in their literature. They proposed to calculate the air –side heat transfer coefficient from overall thermal resistance equation, and to solve the equation they suggested to compute UA value from ϵ -NTU relationship equation, tube-side heat transfer coefficient from Gnielinski (1976) semi-empirical correlation for smooth tube , and air-side overall surface efficiency from Schmidt(1949) equation. They mentioned that water velocity should be maintained high to keep the water-side thermal resistance less than 15% of the overall thermal resistance for obtaining accurate air-side data. They recommended as :1) the energy balance in the air-side and tube-side should be less than 5%, 2) the temperature drop in the tube-side should be higher than 2% for better accuracy 3) selection of proper ϵ -NTU relationship equation for calculating UA value 4) suggested equation for determining friction factor negating the entrance & exit losses. Junqi et al. (2006) followed similar data reduction method as Wang et al. for calculating air-side heat transfer characteristics, but for calculating pressure drop in terms of friction factor calculation they considered the air as an incompressible fluid. The data reduction and

calculation method of Nuntaphan et al., Dong et al. (2007), and Wang & Chi (2000) were similar manner as data reduction method as Wang et al. D. Taler and Jokar et al. calculated the UA value from the heat transfer equation for multi-pass and cross-flow heat exchanger based on the average heat transfer rate, logarithmic mean temperature difference ΔT_{lm} , correction factor F. All followed the iterative procedure to determine the fin efficiency and overall surface efficiency because the fin efficiency is the function of heat transfer coefficient.

2.3.2 The effect of tube rows, fin geometry and tube diameter

Wang and Chi (2000) studied on the air-side heat transfer and friction characteristics of fin and tube heat exchangers with 18 samples. They presented the effect of j factors and f factors due to the number of tube rows, fin pitch and tube diameter. They found that the heat transfer characteristics were strongly connected with the fin pitch; heat transfer enhanced with decreasing fin pitch while numbers of tube rows were 1 or 2 and $300 < Re < 3000$. The effect of fin pitch is insignificant on heat transfer for number of tube rows ≥ 4 and $Re > 2000$. The effect of tube row on heat transfer duty is particularly marked at low Reynolds number for large tube rows and small fin pitch. Junqi et al. (2006) studied experimentally the air-side thermal and hydraulic characteristics of wavy fin and flat tube cross-flow heat exchangers with different fin geometry by using air and water as the working fluid. Numbers of test were performed within the Reynolds number range from 800 to 6500 with different fin geometry at the constant water flow rate of $2.5\text{m}^3/\text{h}$ through the tube. Heat transfer characteristics in terms of Colburn factor j and friction factor f were stated as a function of Reynolds number. j and f factor increased with the increasing of fin spaces at same Reynolds

number, and j factor increased with fin height where as little effect of fin height on f factor . They also proposed the correlations for heat transfer and pressure drop for wavy fins and these correlations can predict 95% of experimental results within $\pm 10\%$. Tang et al. (2009) studied experimentally on air-side heat transfer and friction factor characteristics of five kinds fin-and-tube heat exchangers with 12 number tube rows and 18 mm outside tube diameter within the range of Reynolds number from 4000 to 10000. They found that crimped spiral fin showed the higher heat transfer rate and pressure drop compared with other four types fins. Park and Jacobi (2009) studied experimentally the air-side thermal-hydraulic performance of flat-tube aluminum heat exchangers with serpentine louvered, wavy, and plain fins maintaining the air face velocities from 0.5m/s to 2.8m/s for dry and wet surface conditions. They founded that the effect of fin spacing on j and f influenced the other fin design parameters at high Reynolds number in case of louver fin geometry, but fin spacing did not make any significant impact on j and f factor for wavy-fin tube heat exchangers.

2.3.3 Correlations and comparison

Paeng et al. (2008) investigated air-side convective heat transfer coefficients in fin and tube heat exchanger experimentally and numerically. The velocity of air is increased from 1.13m/s to 1.61m/s in five steps corresponding with Reynolds numbers range from 1082 to 1649. They derived Nusselt number equations by experimental data as well as numerical computation. The relative errors between these two equations are about 6%, and experimental data almost match with numerical computation simulation when air-side Nusselt number is 0.69. They also compared their results with some of previous works with same Reynolds number range, and the relative errors of the equation

experimentally derived and others are the range from 0.4% to 32.4%. Tang & Yang (2005) studied the thermal performance of a single – row fin and tube heat exchanger in cross flow orientation (Water-air) experimentally. Their findings are: a) Maximum difference between the heat transfer rate given up by the water and that absorbed by the air is less than 5% at $Re_w > 1200$ and less than 12% at $Re_w < 1200$, b) Water-side thermal resistance is less than 10% of the total thermal resistance within the Reynolds number range of 1200 to 6000, c) Thermal resistance of water-side is nearly equal to air-side at $500 < Re_w < 1200$. They derived equation for Nusselt numbers for air & water-side. Their obtained water side Nusselt number – Reynolds number correlation was consistent with Dittus-Boelter (1930), Petukhov (1970) and Gnielinski (1976) correlations. They mentioned that there are few appropriate correlations for air-side are available in the open literature. However, they showed the Nusselt number - Reynolds number correlations based on their experiment. D. Taler (2005) determined the correlations for heat transfer characteristics in cross-flow compact heat exchangers by two numerical methods. In the first method, only the air-side correlations for predicting the heat transfer coefficient were determined by using the Gnielinski and Dittus-Boelter correlations for tube-side heat transfer coefficient. In the second method, the correlations for heat transfer coefficient were determined for both air-side and tube-side simultaneously. They formulated the correlations for air-side Nusselt number with Reynolds number and Prandtl number and Colburn j factor with Reynolds number.

2.4 The effect of tube row arrangements on heat transfer

Fluid flow over the tube banks in cross-flow orientation is encountered in heat exchanger design for many engineering applications. The tube rows of a bank is usually

arranged either inline or staggered along the direction of fluid flow. In these tube rows arrangement a wake region may be formed behind the tube when fluid flowing over the tube. The effect of tube row arrangement on heat transfer is stated in several literatures. They observed that the local Nusselt number in the wake region is very low that would lead to weak convective heat transfer in this region. Similar results were obtained by Tian et al.(2009) during numerical studies on wavy fin-and-tube heat exchangers which had three-row round tubes in staggered or inline arrangements. El-Shaboury and Ormiston (2005) numerically studied on forced-convection heat transfer of cross-flow in banks of plain tubes in square and non-square inline arrangements. They found that the heat transfer rate around the first tube in the bundle is always higher than the tubes following it. Taler (2005) studied numerically on heat transfer of double rows, two-pass automotive radiator in laminar flow region. The major and minor diameters of oval shaped tubes were 11.82 mm and 6.35 mm respectively. Their numerical simulation revealed that the regions behind the tubes contributed very small to the performance of the heat exchanger. The heat transfer rate is observed very low in the second row due to presence of the wakes in the front and behind the tube. Fig.3.1 illustrates two different flow channel arrangements. 3.1(a) shows the flow channels located in the flat slab which type is used in the current study, and 3.1(b) shows the inline tube arrangements into conventional heat exchanger.

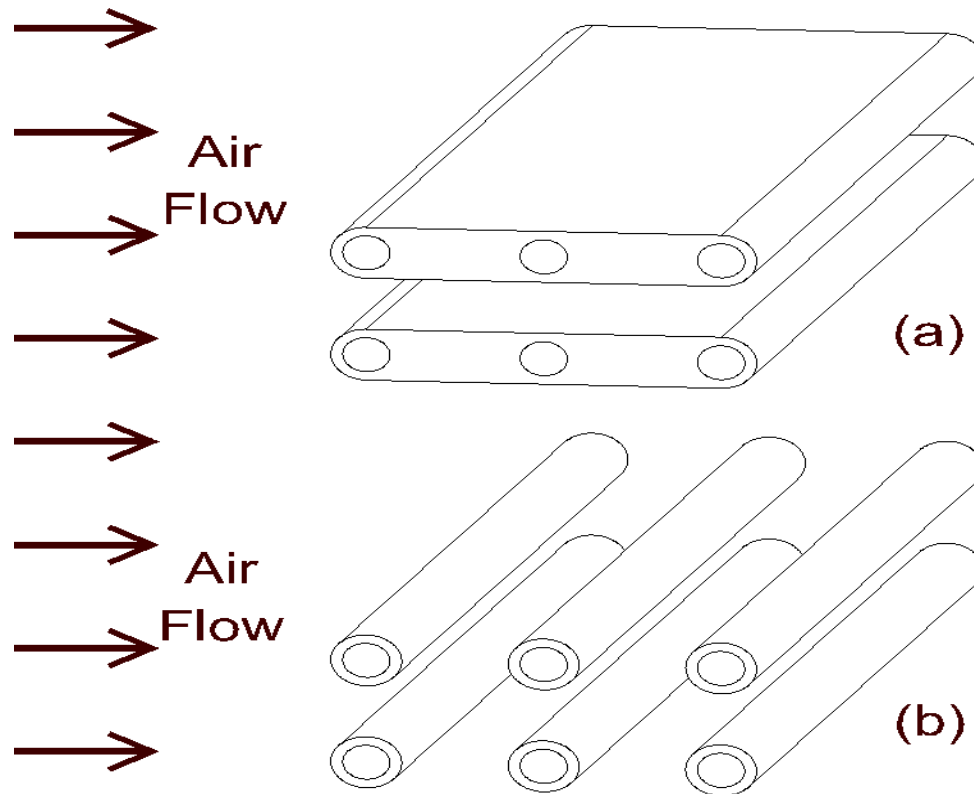


Figure-2.1: (a) Microchannel Slab; (b) Inline Tube Bank Arrangement

The heat exchanger used in the current study is built up by multiport microchannel slabs. The multiport microchannel slab has no gap in between the flow channels which offers flat heat transfer areas at the top and the bottom faces of each slab. This allows the flowing air to make very well contact with the heating surfaces, and it provides almost uniform temperature distribution throughout the heat exchanger core. Thus it is expected that leads to higher heat transfer over the conventional heat exchangers of isolated tube rows.

2.5 Scope of the current study

The cooling of air through the microchannel heat exchanger in deionized water to air cross-flow orientation was studied experimentally. A microchannel heat exchanger core is made up of 15 extruded aluminum slabs. Each slab contains 68 microchannels of

1mm circular diameter. The experimental setup consisted of a closed-loop thermal wind tunnel, an air-blower, a liquid circulating pump, a variety of measuring instruments, a data acquisition system and a microchannel heat exchanger core as the test specimen. Using chilled water in the cooling coil to cool the air is the usual practice in HVAC fields. Both hot air and cold deionized water inlet temperatures were maintained constant at $38 \pm 0.5^\circ\text{C}$ and $9 \pm 0.5^\circ\text{C}$ respectively. Hot air at different velocities (1 m/s to 5 m/s) was allowed to pass through the finned passages of the heat exchanger core, while cold deionized water at a certain level of mass flow rate was passed through the microchannels. Four levels of deionized water mass flow rates were maintained in the study.

The method of data reduction and calculation was followed in accordance with previous studies; special attention was given to the studies of Wang et al. (2000), D. Taler (2005) and Jokar et al. (2010). The air-side heat transfer and flow characteristic key parameters such as Reynolds number (Re_a), friction factor (f_a), Nusselt number (Nu_a), Prandtl number (Pr_a), Stanton number (St_a), Colburn factor (j_a), and overall thermal resistance (R_{Total}), effectiveness, NTU were obtained from experimental data. The effect of air-side Reynolds number on Nusselt number, Colburn factor, friction factor, and other parameters were examined. The air-side heat transfer correlation in the form of Nusselt number as the function of Reynolds number and Prandtl number ($Nu_a-Re_a-Pr_a$) was achieved. The heat transfer correlation of the current study is compared to other such correlations, available in the open literature. The investigations were performed in laminar regimes with air and water-side Reynolds number ranges of 283 to 1384 and 110 to 152 respectively.

CHAPTER III

EXPERIMENTAL SETUP AND OPERATIONAL PROCEDURE

3.1 Experimental setup

The current study was performed in the well-equipped single phase air to liquid crossflow experimental setup which is capable to investigate fluid flow and heat transfer characteristics of several working fluids in the liquid side under a wide range of operating conditions. The major components of the experimental setup (Fig. 3.1) for this study includes a closed loop integrated thermal wind tunnel, test chamber, variable speed gear pump, circulation heater, data acquisition system composed of large number of measuring instruments and the serpentine finned microchannel heat exchanger core.

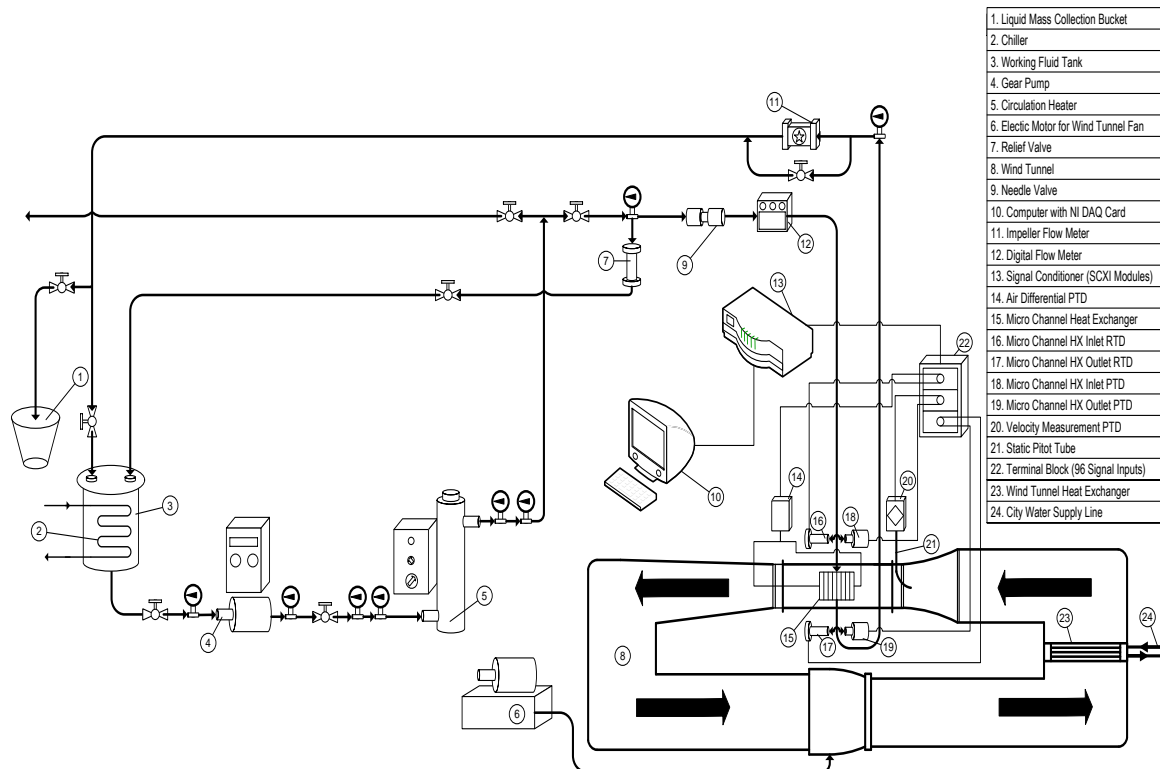


Figure 3.1: The schematic diagram of experimental setup

3.1.1 Air handling system

A closed loop thermal wind tunnel (8) having 5440 mm length, 750 mm width, 1640 mm height and 10 mm wall thickness is the largest component of the experimental setup. The contraction ratio of wind tunnel is 6.25. A variable speed electric motor is used to operate blower fan for accomplishing different air velocities through the wind tunnel duct via test section. The wind tunnel is capable to provide the air velocity up to 30 m/s without any obstruction and up to 11m/s with the heat exchanger core of current study. One heat exchanger (23) is in built with the wind tunnel to cool or heat the air before entering the test section. Building cold and hot water supply (24) are used in this heat exchanger to regulate the inlet air temperature ($T_{a,i}$).The test chamber is installed at the upper middle part of the wind tunnel. Two T-type thermocouple grids are installed in the wind tunnel at upstream and downstream of the test chamber respectively to measure the air inlet and outlet temperature of test section precisely.

3.1.2 Test chamber and MCHX core

The internal cross section of the test chamber across the air flow is square shape (305 mm x 305 mm) and a length of 610 mm along the flow direction, and it is shown in the Fig. 3.2. The test chamber is well fitted with the wind tunnel's loading platform. The well fitted test chamber cross section makes sure stable air flow from wind tunnel to test section without disturbance to minimize experimental uncertainties. The test chamber is built in 6.5 mm thick Plexiglas having a low thermal conductivity of 0.19 W/m.°C. The test chamber is also covered by additional insulation to ensure the negligible heat transfers due to conduction from test chamber to surroundings or vice versa. The microchannel heat exchanger core in the current study is installed in the middle (halfway

along the 610 mm length in the test chamber) of the test chamber. A 12 inch pitot static probe (21) along with a thermocouple probe is installed at the center of air entry cross section of test chamber to measure the inlet air velocity.

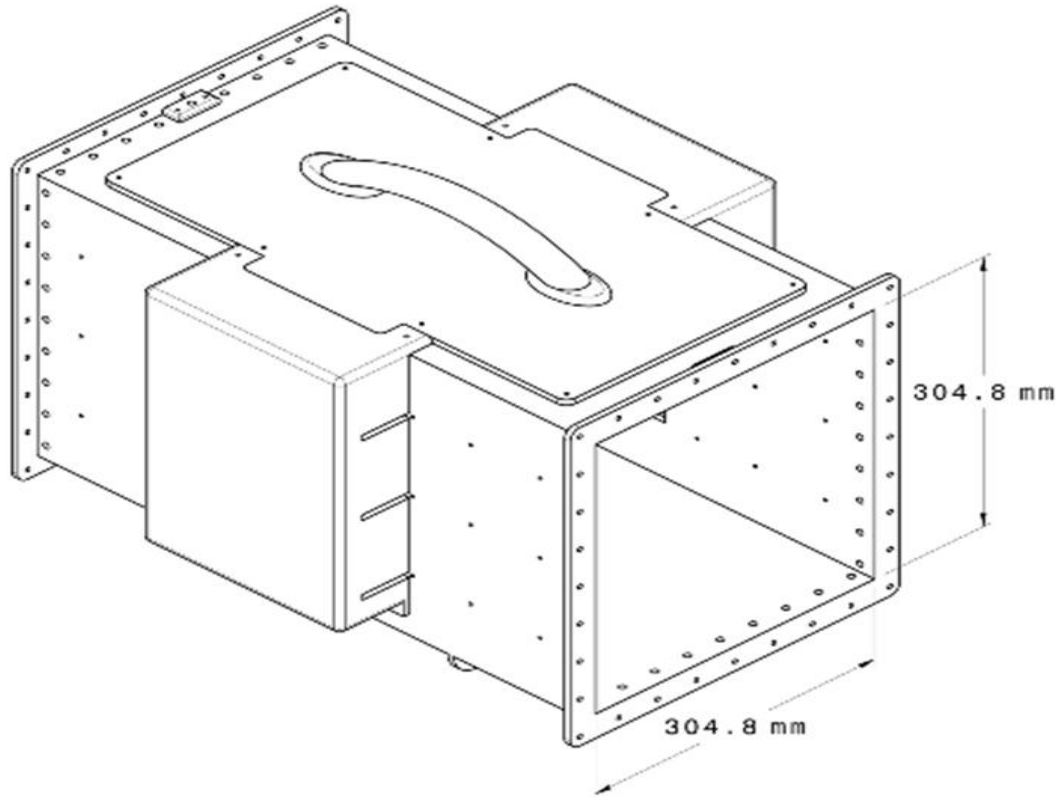


Figure 3.2: Test chamber

The microchannel heat exchanger in the current study is made up of fifteen extruded multiport serpentine aluminum slabs having 68 circular channels in each slab which is shown in the Fig. 3.3. Each slab (Fig. 3.4) has 2 mm height having channel's inner circular diameter set at 1 mm, and the airside frontal area is 304 mm x 304 mm. The channels in the slab were built using precision micro multiport extrusion technique. The microchannel heat exchanger has 3 circuits with total 15 passes, and it can be capable of withstanding the working pressure up to 15 MPa. The liquid side working fluid comes into heat exchanger core through the inlet pipe, distributes in to three inlet manifolds

from the inlet header and passes through three circuits (three independent serpentine slab sections), and each circuit has five passes. After taking part in heat transfer, the liquid leaves from heat exchanger core through the outlet pipes via exit manifolds and exit header.

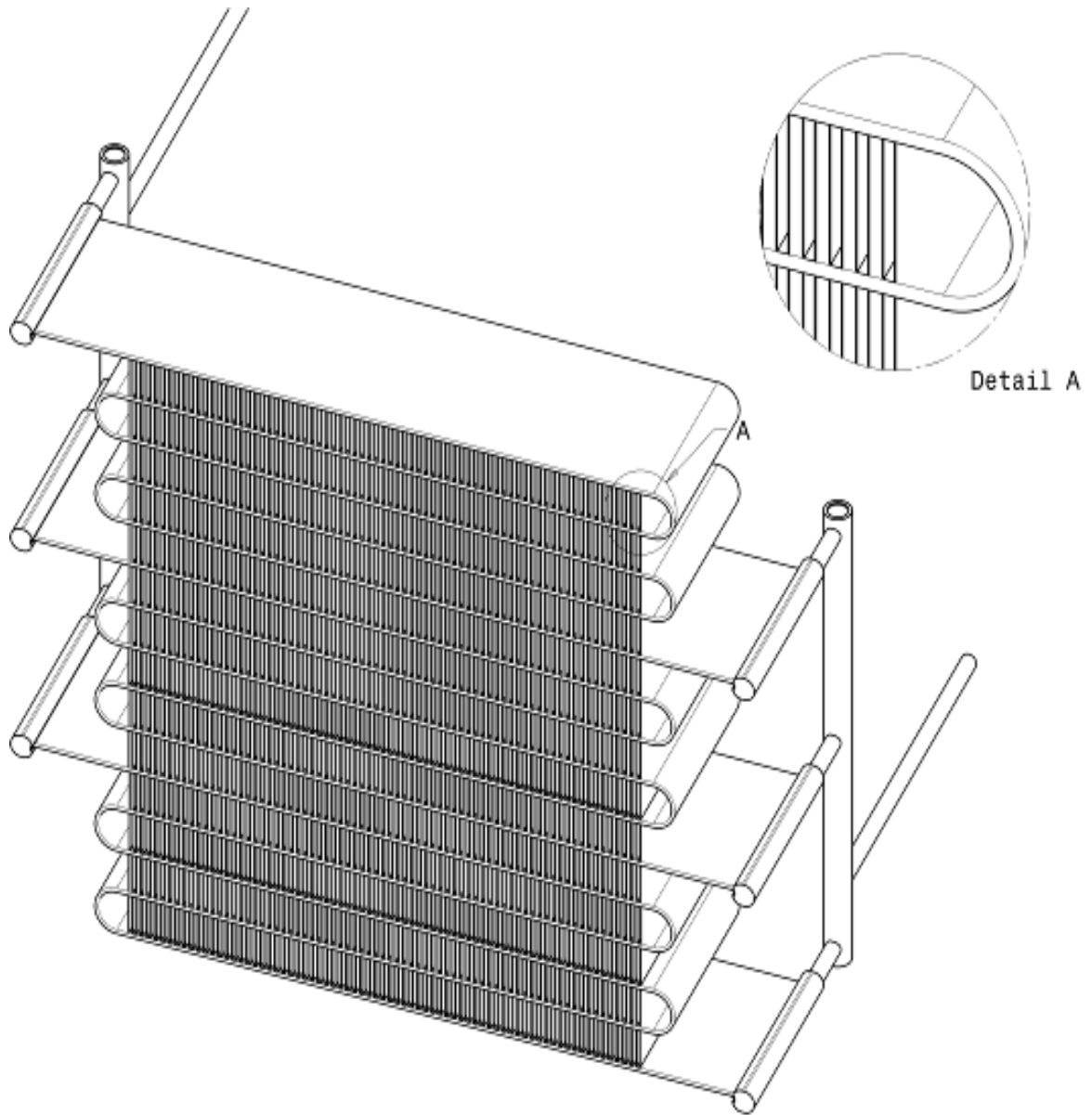


Figure 3.3: Microchannel heat exchanger core

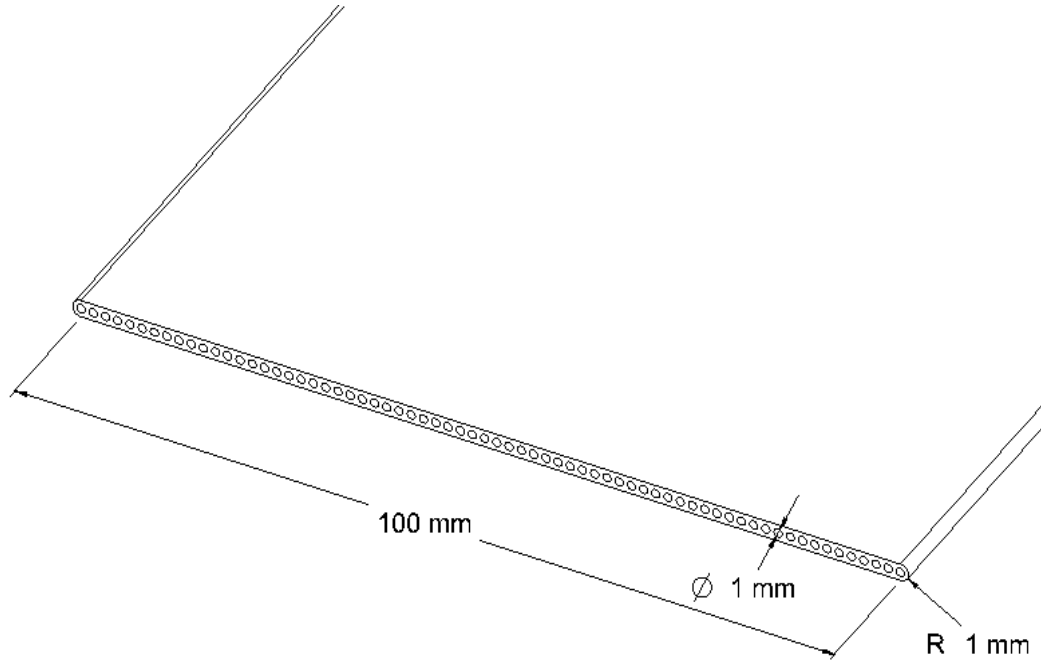


Figure 3.4: Single microchannel heat exchanger slab

The specifications of liquid and air-side of microchannel heat exchanger core are shown in Table- 3.1a and Table-3.1b respectively.

Table 3.1a: Specifications of MCHX (liquid side)

No. of slabs (N_{MS})	15
No. of channels per slab (N_{CS})	68
Micro channel diameter ($D_{MS}=D_{h,w}$)	$1 \times 10^{-3}m$
Microchannel slab height (S_h)	$2 \times 10^{-3}m$
No. of flow circuits (N_{FC})	3
No. of flow passes per circuit	5
Total flow passes	15
Total heat transfer area in water-side (A_w)	$974.7 \times 10^{-3}m^2$

Table 3.1b: Specifications of MCHX core (air-side)

Hydraulic diameter ($D_{h,a}$)	$3.49 \times 10^{-3}m$
Fin type	Deep wavy
Fin height (F_h)	$16 \times 10^{-3}m$
Fin spacing (F_s)	$2 \times 10^{-3}m$
Fin thickness (F_t)	$0.1 \times 10^{-3}m$
Fin density (F_d)	12 fins per 25.4mm
Minimum free flow area ($A_{min,a}$)	$70.9 \times 10^{-3}m$
Frontal size ($A_{fr,a}$)	$0.304m \times 0.304m$
Air flow length (L_a)	$100 \times 10^{-3}m$
Total fin area ($A_{f,a}$)	$7.88m^2$
Total heat transfer area in air-side (A_a)	$8.13m^2$
Contraction ratio (σ_a)	0.818

3.1.3 Liquid circulation system

The deionized water was used as the cold side working fluid of the microchannel heat exchanger in the current study. It was drawn from reservoir tank by a gear pump as well as forced to circulate through microchannel heat exchanger core where heat was transferred from hot air to cold deionized water, and again came back to the reservoir

tank. The major components of the liquid circulating system are: reservoir tank, gear pump, inline circulation heater, piping network, flow control fittings, flow monitoring and measuring instruments. The inline circulation heater is not used in the present study. The flow control fittings contain pressure relief by pass valves, ball valve, needle valves, micro-filters etc. The flow monitoring and measuring instruments includes digital flow meter, impeller flow meter, pressure and temperature gauges, resistance temperature detector, and pressure transducer. The gear pump is generally used such kind of experimental setup where constant volume flow rate is expected irrespective of the upstream pressure change. The gear pump is operated by a frequency controlled 5.6 kW electric motor which is accomplished the desired liquid flow rate in the system.

The micro-filter is installed before the digital flow meter which prevents unwanted access of foreign particles in to the heat exchanger core. The digital flow meter simultaneously measures the volume flow rate, temperature and pressure of the flowing liquid. Liquid circulation system can capable to handle various liquid such as water, ethylene glycol water mixture, engine oil etc. Out of two sets of Pressure transducer (PTD) and Resistance Temperature Detector (RTD), one set is installed at the inlet and another at exit of the core. The liquid flow direction is shown in the Fig. 3.1. The liquid circulation system can be operated in closed loop and open loop; in the present study it is used in the closed loop operation. The bucket stop watch method is also used to verify the accuracy of deionized water mass flow rate.

3.1.4 Data acquisition system

The data acquisition system (DAQ) contains data acquisition software (LabView), a 128- channel 16-bit data acquisition card, a terminal block to connect all instruments

and sensors cables and a signal conditioner. Some auxiliary equipment are also incorporated with the DAQ system: uninterruptable power supply unit for ensuring continuous power supply and DC power supply unit to supply 24V DC power to instruments for excitation. The 128 –channels are working in multiplex mode and the DAQ system is accomplished to measure as well as monitor the experimental data from 96 different points through 96 channels. All PTDs, thermocouples, RTDs, etc. are connected to DAQ system through these channels. The DAQ system is capable to take sample at the rate of 100 kHz. The sample rate is selected in the present study at 1 kHz for accuracy and consistency.

3.2 Experimental methodology and operating conditions

The air-side heat transfer and flow behaviors of cross-flow serpentine slab microchannel heat exchanger were investigated experimentally during air cooling. The cold deionized water at $9 \pm 0.5^\circ\text{C}$ was forced to pass through the microchannel heat exchanger core at four levels of mass flow rates from 0.0169 kg/s to 0.025 kg/s corresponding to Reynolds number 105 to 159. The constant Deionized water inlet temperature is maintained to remove heat from liquid tank through a chillier. The hot air at five face velocities from 1m/s to 5 m/s were allowed to flow in to the finned passages of heat exchanger core maintaining constant air inlet temperature at $38 \pm 0.5^\circ\text{C}$ for each deionized water mass flow rate. The operating conditions are specified in the Table 3.2. The air inlet temperature was kept constant by built in heat exchanger of wind tunnel through mixing of building cold and hot water supply. The range of air-side Reynolds number was in the region of 283– 1384. Generally two kinds of cooling coils are installed in the air handling duct for air cooling in HVAC system: chilled liquid cooling coil and

direct expansion cooling coil. Air cooling through chilled liquid (water or water-antifreeze liquid mixture) cooling coil is widely used in air-conditioning system. The range of face velocity of air such kind of cooling system is 2 m/s to 3 m/s for most commercial and residential applications. The operating conditions of the current study were chosen to focus these air face velocities.

Table 3.2: Operating conditions

Parameters	
Air inlet temperature ($T_{a,i}$)	$9 \pm 0.5^{\circ}\text{C}$
Deionized water inlet temperature ($T_{w,i}$)	$38 \pm 0.5^{\circ}\text{C}$
Deionized water mass flow rate (\dot{m}_w)	0.0169 kg/s, 0.0188 kg/s, 0.02 kg/s and 0.024 kg/s
Deionized waterside Reynolds number range(Re_w)	110- 152
Air velocity at each deionized water mass flow rate (V_a)	1m/s, 2 m/s, 3 m/s, 4 m/s and 5 m/s
Air-side Reynolds number range(Re_a)	283- 1384

3.3 Data collection for different parameters

A number of measuring and monitoring instruments are connected with data acquisition system. The selections of instruments and sensors were based on their

accuracy and ability for connectivity with data acquisition system. The accuracy information of instruments and sensors were collected from manufacturer's data and instrument specifications. The overall instruments error were estimated from the root sum square of all identified errors such as resolution, absolute error, linearity, repeatability, hysteresis, zero offset, various drifts etc. The highlights of major instruments are presented here.

3.3.1 Air-side measurements

Air inlet and outlet Temperature Measurement

Two T-type (TTT-30) thermocouple grids, one consisting of 9 (3x3) thermocouples (Fig. 3.5) and the other consisting of 25 (5x5) thermocouples (Fig. 3.6) are installed in the upstream and downstream of the wind tunnel test chamber respectively to measure the air inlet and outlet temperature of test section precisely. Inlet air enters directly into the heat exchanger core without any disturbance, but the outlet air goes through the narrow passages (in between fins) facing difficulties as well as taking part in the heat transfer before exiting from the core. Hence, the temperature variations within inlet cross-section are smaller than outlet cross-section; as such more thermocouples are placed in the outlet cross-section. One inlet and one outlet temperature distribution profile for an operating condition are shown in Fig. 3.7 and Fig. 3.8 respectively.

The Curie temperature or Curie point is the temperature at which ferromagnetic or ferrimagnetic materials become paramagnet on heating. T - type thermocouple are used in experimental setup because it is built of two non-magnetic elements (copper and copper –nickel alloy) which have not any Curie point, so there is no sudden change in

characteristics during experiment. The used T-type thermocouple (TTT-30) has wide operating range of $-200\text{ }^{\circ}\text{C}$ to $350\text{ }^{\circ}\text{C}$ and accuracy $\pm 0.8^{\circ}\text{C}$.

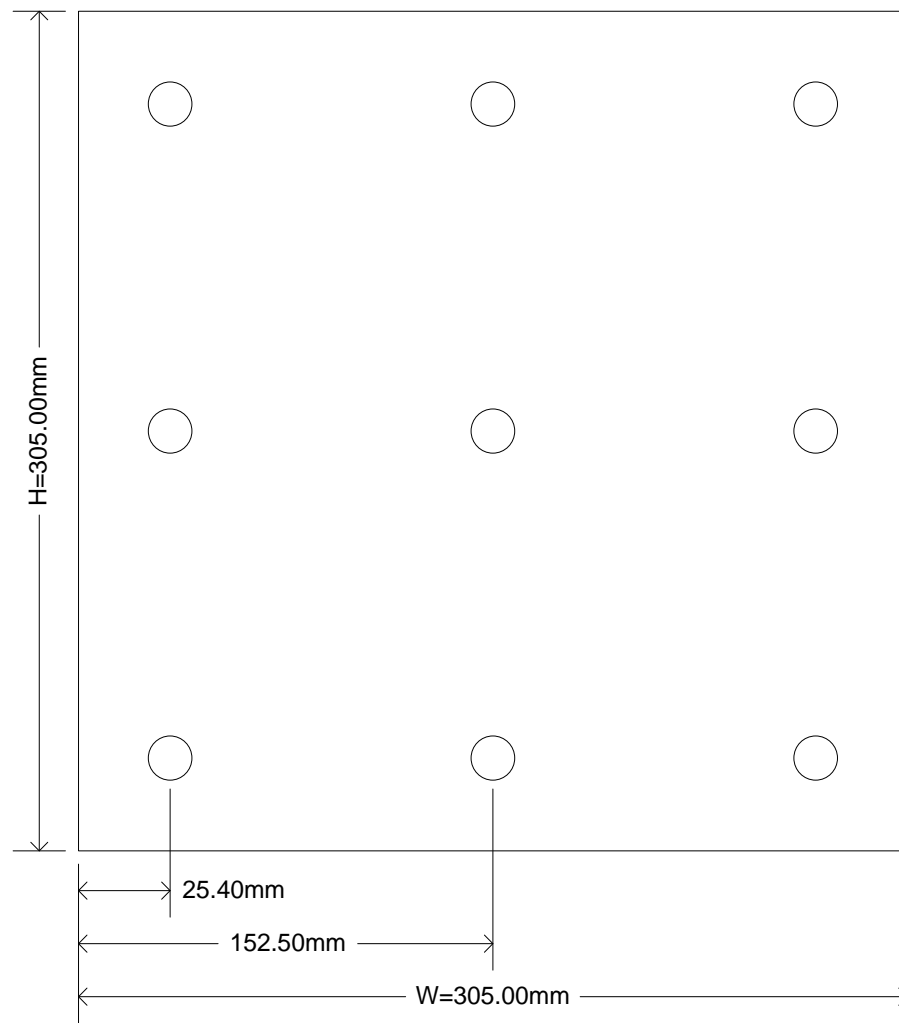


Figure 3.5: Air inlet thermocouple grid

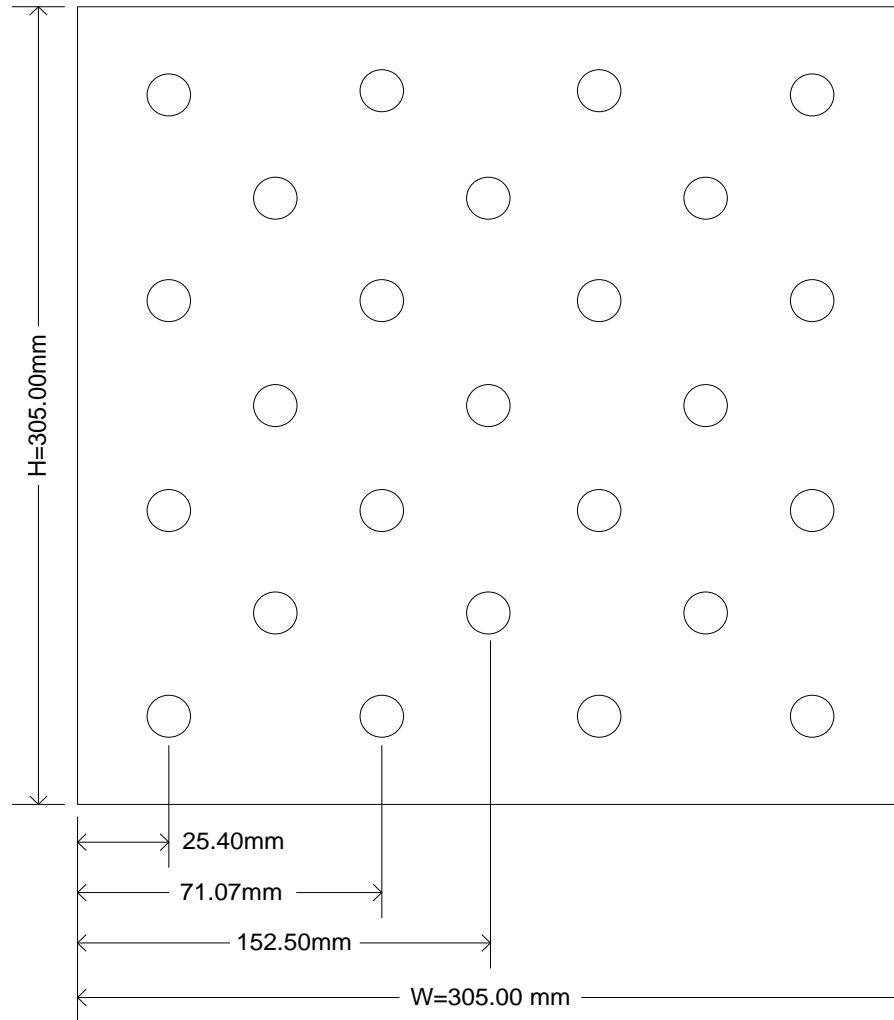


Figure 3.6: Air outlet thermocouple grid

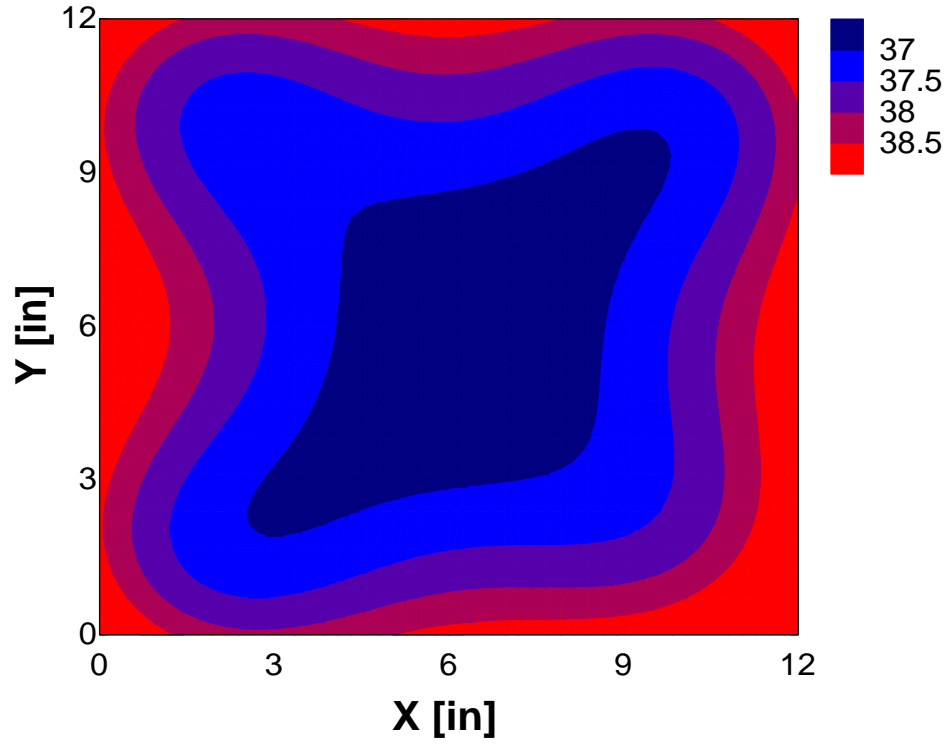


Figure 3.7: Air inlet temperature profile ($\bar{T}_{a,i} = 38.1\text{ }^{\circ}\text{C}$)

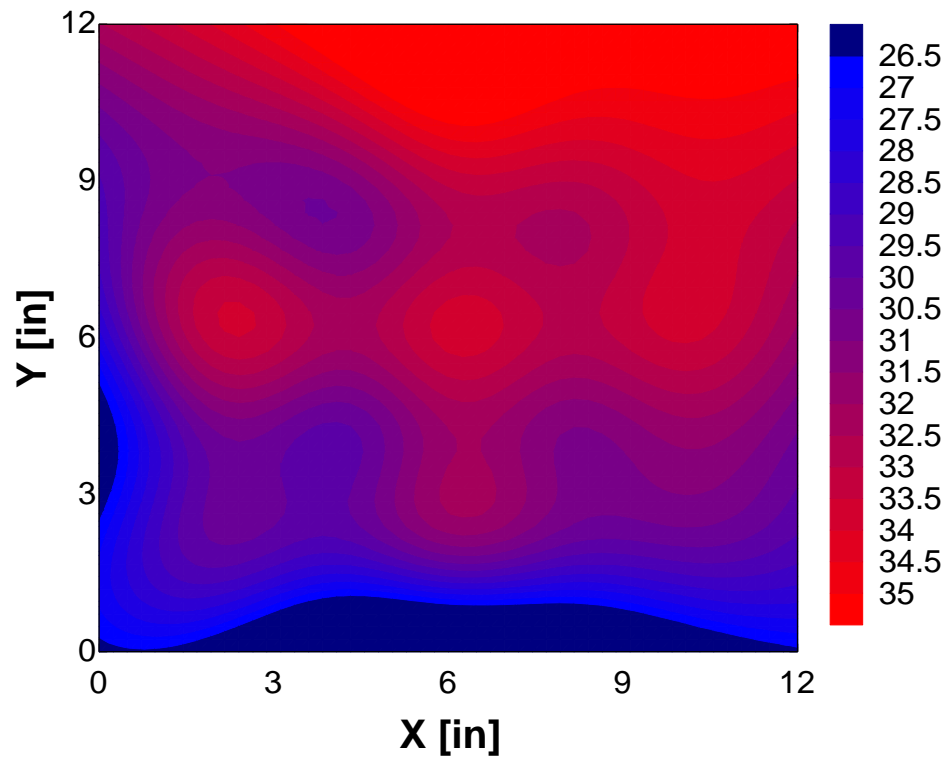


Figure 3.8: Air Outlet Temperature Profile ($\bar{T}_{a,o} = 31.5\text{ }^{\circ}\text{C}$)

Differential Pressure Measurement

Three pressure transducers are installed in the air-side to measure the differential pressure at top, middle and bottom between entry and exit through microchannel heat exchanger core. The specifications of used differential pressure transducer are mentioned in Table-3.3.

Table 3.3: Differential pressure transducers for air-side

Model	Qty	Capacity/range	Accuracy	Manufacturer	Purpose (diff. pressure)
PX653-03D5V	1	0- 748 Pa	$\pm 0.25\%$ FS	Omega	Top
PX277-01D5V	1	0 – 249 Pa	$\pm 1\%$ FS	Omega	Middle
PX653-0.5D5V	1	0 – 125 Pa	$\pm 0.25\%$ FS	Omega	Bottom

Air Velocity Measurement

A pitot static probe (12 inch, Model Po12A-CF) is installed at the center of the air inlet cross section to measure the air velocity into microchannel heat exchanger core. A digital manometer (Flow Kinetics) is connected with the pitot static probe for monitoring and measurement of inlet air velocity.

3.3.2 Deionized water-side measurements

Two ultra-precise resistance temperature detectors (pt100 – PM1/10-1/4xxx): one for inlet and another one for outlet are placed to measure the inlet and exit deionized water temperature. The RTDs have excellent accuracy ($\pm 0.012^\circ\text{C}$) over a wide temperature range (-100°C to 400°C). The RTD shows almost linear relationship between

temperature and resistance and thermal response time. One digital (FV4000) and one impeller flow meter (FPR-303) are connected with liquid handling circuit to measure the deionized water flow rate. The accuracies of digital and impeller are $\pm 0.5\%$ FS and $\pm 1\%$ FS respectively. Two pressure transducers (PX 309-005G5V) are installed to measure the inlet and exit pressure of microchannel heat exchanger core. The pressure transducer has accuracy $\pm 0.25\%$ FS with reverse polarity and overvoltage protection. All instruments were calibrated according to maintain all standard procedures and supplier's recommendations.

CHAPTER IV

THEORETICAL CONSIDERATIONS AND DATA REDUCTION

The evaluation of fluid flow and heat transfer characteristics are based on the theoretical background and their relationships. The interest of parameters and data reduction and analysis procedures are mentioned in this chapter.

4.1 Interest of key parameters

The thermal and hydraulic behaviors are expressed in terms of dimensionless numbers which are used extensively in fluid mechanics and heat transfer area for analyzing, comparing and representing their characteristics. The dimensionless number such as Reynolds number (Nu), Fanning friction factor (f), Nusselt number (Nu) , Stanton number (St) and Colburn factor (j) are considered key dimensionless parameters in this study.

Reynolds Number (Re)

Osborne Reynolds, a British engineer and physicist, discovered that the flow regimes depends mostly on the ratio of inertia forces to viscous forces of flowing fluid. This ratio is defined as the Reynolds number which is named after him. The Reynolds number is expressed as

$$Re = \frac{\text{Inertia Forces}}{\text{Viscous Forces}} = \frac{\rho V L_c}{\mu} \quad (4.1)$$

Where ρ is the fluid density, V is the upstream velocity, L_c is characteristics length of the geometry, and μ is the dynamic viscosity of fluid. Flow regimes such as laminar, transition and turbulent, are represented by Reynolds number. In the large Reynolds number the inertia forces are greater relative to viscous forces which cannot prevent the quick and random fluctuations of the fluid. This is categorized under turbulent flow

regime. Small and moderate Reynolds numbers fall in the laminar flow regime where the viscous forces are big enough to suppress the fluctuations due to inertia forces and to retain the fluid ‘in line’.

Fanning Friction Factor (f)

Fanning friction factor (f) also called friction coefficient (C_f), named after the American engineer John Fanning. It is defined as the ratio of wall friction forces to the inertia forces. Fanning friction factor can be expressed as

$$f = \frac{\text{Wall Friction Force}}{\text{Inertia Force}} = \frac{2\tau_w}{\rho V^2} = \frac{f_D}{4} \quad (4.2)$$

Where τ_w is wall shear stress and f_D is the Darcy-Weisbach friction factor. Fanning friction factor is widely used to express the fluid flow behaviors.

Nusselt Number (Nu)

The Nusselt number is viewed as the dimensionless heat transfer coefficient, and it is named after Wilhelm Nusselt, a German engineer. The Nusselt number is defined as the ratio of convection heat transfer to conduction heat transfer. It is expressed as

$$Nu = \frac{\text{Convection Heat Transfer}}{\text{Conduction Heat Transfer}} = \frac{hL_c}{k} \quad (4.3)$$

Where h is the heat transfer coefficient and k is the thermal conductivity of the fluid. A Nusselt number =1, represents heat transfer across the particular layer by pure conduction. The heat transfer occurs due to convection through a fluid layer when fluid in movement. Hence convection heat transfer can be increased by increasing fluid flow. It is usual practice to nondimensionalize the heat transfer coefficient h with Nusselt number. In practical heat transfer applications it is difficult to evaluate the heat transfer coefficient directly due to complex geometrical shapes and heat transfer areas. Nusselt number is

evaluated from experiment, and subsequently heat transfer coefficient is computed from their relationship equation.

Stanton Number (St)

The Stanton number (St) is also a dimensionless heat transfer coefficient which is the ratio of convection heat transfer (per unit duct surface area) to the enthalpy rate change of the fluid reaching the wall temperature (per unit of flow cross-sectional area). It is named after Sir Thomas Edward Stanton, a British engineer who introduced this dimensionless number. It is expressed as

$$St = \frac{\text{Heat Transfer}}{\text{Thermal Capacity}} = \frac{h}{\rho c_p V} \quad (4.4)$$

The relation among the Nusselt number, Stanton number, Prandtl number and Reynolds number can be expressed as

$$Nu = St \cdot Re \cdot Pr \quad (4.5)$$

Equation (4.5) is always valid regardless of flow passage geometry, boundary condition, flow types, and so on ((Shah and Sekulić 2003).

The quantitative determination of friction coefficient f (to compute the shear stress at wall) and Nu (to compute the heat transfer rate) are essential for forced convection analysis. The relation is developed based on the similarity between momentum and heat transfer in boundary layers, and it is known as Reynolds analogy (Çengel and Ghajar 2010). The Stanton number (St) is used to express Reynolds analogy as

$$\frac{f}{2} = St = \frac{Nu}{Re \cdot Pr} = \frac{Nu}{Re} \quad (4.6)$$

Where, $Pr \approx 1$, thus, Reynolds analogy is limited use due to Prandtl number value is considered 1.

Colburn Factor (j)

The Colburn factor j is also a dimensionless heat transfer coefficient, and it is named after Allan Philip Colburn, an American engineer. The Colburn factor is the modified Stanton number where moderate variations in the Prandtl numbers are taken in to account. It is defined as

$$j = St \cdot Pr^{\frac{2}{3}} = \frac{Nu \cdot Pr^{-\frac{1}{3}}}{Re} \quad (4.7)$$

Colburn factor is used to express Chilton –Colburn analogy as

$$\frac{f}{2} = St \cdot Pr^{\frac{2}{3}} = j \quad 0.6 < Pr < 60 \quad (4.8)$$

The effect of Reynolds number on Colburn factor j and Fanning friction factor f are extensively showed in open literature to express heat transfer and flow behaviors of heat exchangers.

4.2 Assumptions for current study

The following assumptions were made during experimentation, data reduction and analysis:

1. Steady state condition for all experimental runs: Maintained steady state condition for all experimental runs. The duration of experimental run was minimum one hour for each particular operating condition to make steady state and to take data through DAQ system.
2. No change of kinetic and potential energy in the core: The inlets and outlets of heat exchanger core were at same elevation, and no kinetic energy was added in the heat exchanger. Hence, it is logical to consider that there was no change of kinetic and potential energy in the microchannel heat exchanger core.

3. Negligible heat loss to the surroundings due to conduction, convection and radiation: The test chamber is built of very low thermal conductive materials. Additional thermal insulations were provided to prevent heat loss to the surroundings.
4. Negligible thermal resistance in the heat exchanger core due to fouling: The microchannel heat exchanger core is almost new. As such, it is considered to ignore the thermal resistances due to fouling in calculation process.
5. No condensation effect on heat transfer in the air-side: The air-side temperatures and pressures conditions were not allowed to form condensations on air-side heating surfaces.

4.3 Data reduction and analysis

A 128-channel 16 bit data acquisition (DAQ) system allowed continuous monitoring of different parameters and data collection at any time during the experimentation. The data were collected at a steady state condition for the current study to compute the heat transfer and fluid flow key parameters of microchannel heat exchanger core such as average heat transfer rate (\dot{Q}), overall thermal resistance ($R_{total} = 1/UA$), Number of transfer unit (NTU), Effectiveness (ϵ), air-side Nusselt number (Nu_a), Stanton number (St_a), Colburn factor (j_a), Reynolds number (Re_a), Fanning friction factor (f_a) and water-side Nusselt number (Nu_w) and Reynolds number (Re_w). Thermodynamic properties of air and water are calculated based on the average inlet and outlet temperatures of the air and water respectively.

4.3.1 Deionized water-side parameters evaluation

Reynolds number (Re_w)

The deionized water was forced to flow through 3 x 68 microchannels of three microchannel slabs. The deionized water Reynolds number is computed as the following equation:

$$Re_w = \frac{G_w D_{h,w}}{\mu_w} \quad (4.9)$$

Where $D_{h,w}$ (=1mm) is the hydraulic diameter of microchannel, and G_w is the mass velocity of water which is expressed as

$$G_w = \frac{\dot{m}_w}{nA_w} \quad (4.10)$$

Combining Eq. (4.7) and (4.8), water-side Reynolds number equation becomes as

$$Re_w = \frac{\dot{m}_w D_{h,w}}{nA_w \mu_w} \quad (4.11)$$

Nusselt Number (Nu_w) and Heat Transfer Coefficient (h_w)

The water-side heat transfer coefficient (h_w) is computed from Gnielinski correlation mentioned by Kakac and Hongtan 2002 for thermally developing and hydrodynamically developed laminar flow in smooth circular tubes as,

$$Nu_w = \left[3.66^3 + 1.61^3 \left(\frac{Pe \cdot d}{L} \right)_w \right]^{1/3} \quad (4.12)$$

Where, Pe is the Péclet number. Péclet number is a dimensionless heat transfer number which is the ratio of bulk heat transfer to conduction heat transfer. It can be expressed as

$$Pe_w = (Re \cdot Pr)_w \quad (4.13)$$

d = channel diameter (= $D_{h,w}$ = 1mm) and L = channel length.

Hence, the water-side heat transfer coefficient (h_w) is calculated from the Nusselt number definition expression as,

$$h_w = \left(\frac{Nu.k}{D_h} \right)_w \quad (4.14)$$

4.3.2 Overall MCHX's parameters evaluation

Heat Transfer Rates (\dot{Q}_a and \dot{Q}_w)

The heat transfer rate can be evaluated from the overall energy balance for hot air and cold water as

$$\dot{Q}_a = \dot{m}_a c_p (T_{a,i} - T_{a,o}) \quad (4.15)$$

$$\dot{Q}_w = \dot{m}_w c_p (T_{w,o} - T_{w,i}) \quad (4.16)$$

The arithmetic average of \dot{Q}_a and \dot{Q}_w is used to compute the air-side heat transfer parameters as on following equation

$$\dot{Q} = \frac{\dot{Q}_a + \dot{Q}_w}{2} \quad (4.17)$$

Overall Thermal Resistance (R_{total})

For a multi-pass and cross-flow heat exchanger the heat transfer rate can be expressed as,

$$\dot{Q} = UAF\Delta T_{lm,cf} \quad (4.18)$$

Where, $\Delta T_{lm,cf}$ is the log mean temperature difference for counter-flow, and F = Log Mean Temperature Difference correction factor for cross-flow heat exchanger. The LMTD correction factor F is nondimensional, and it depends on the temperature effectiveness P, heat capacity rate ratio R and flow arrangement. Rearranging equation (4.16), the overall thermal resistance ($R_{total} = 1/UA$) can be evaluated as

$$R_{total} = \frac{1}{UA} = \frac{F\Delta T_{lm,cf}}{\dot{Q}} \quad (4.19)$$

Effectiveness (ε) and NTU

The effectiveness (ε) of a heat exchanger is defined as the ratio of the actual heat transfer rate to the maximum possible heat transfer rate. The effectiveness (ε) is expressed as

$$\varepsilon = \frac{\dot{Q}}{\dot{Q}_{max}} = \frac{\dot{Q}}{(\dot{m}c_p)_{min}\Delta T_{max}} \quad (4.20)$$

The minimum heat capacity rate ($\dot{m}c_p$) is found at water-side. The maximum temperature difference is obviously observed between air inlet ($T_{a,i}$) and water inlet ($T_{w,i}$). The equation (4.18) becomes as

$$\varepsilon = \frac{\dot{Q}}{(\dot{m}c_p)_w (T_{a,i} - T_{w,i})} \quad (4.21)$$

The number of transfer units (NTU) is a dimensionless parameter which is extensively used for heat exchanger analysis. The NTU is defined as

$$NTU = \frac{UA}{C_{min}} = \frac{UA}{(\dot{m}c_p)_w} \quad (4.22)$$

4.3.3 Air-side parameters evaluation

Reynolds Number (Re_a)

Air-side Reynolds number (Re_a) is computed from the definition as

$$Re_a = \frac{G_a D_{h,a}}{\mu_a} \quad (4.23)$$

Where, G is the core mass velocity which is expressed as

$$G_a = \frac{\dot{m}_a}{A_{min}} \quad (4.24)$$

The air-side hydraulic diameter in Eq. (4.23) is evaluated by the following expression for matrix flow passages (Kays and London, 1984):

$$D_{h,a} = \frac{4L_a A_{min,a}}{A_a} \quad (4.25)$$

Where, L_a is the air-side flow length of the exchanger core, k_a is the thermal conductivity of air, and $A_{min,a}$ is the minimum free flow area of air through the exchanger core.

Fanning Friction Factor (f_a)

Fanning friction factor f_a (also called friction coefficient $C_{f,a}$) is evaluated on the following equation proposed by Kays and London, 1984, for flow to finned –tube banks.

$$f_a = \left(\frac{A_{min,a}}{A_a} \right) \left(\frac{\rho_{a,b}}{\rho_{a,i}} \right) \left[\left(\frac{2\Delta P_a \rho_{in,a}}{G_a^2} - (1 + \sigma_a^2) \left(\frac{\rho_{a,i}}{\rho_{a,o}} - 1 \right) \right) \right] \quad (4.26)$$

Heat Transfer Coefficient (h_a)

The overall thermal resistance can also be expressed as

$$R_{total} = R_a + R_{wall} + R_w \quad (4.27)$$

Where, $R_a (= \frac{1}{(\eta h A)_a})$ and $R_w (= \frac{1}{(h A)_w})$ are the convection thermal resistances of air and

water-side respectively. The thermal conductivity of aluminum is very high, so the thermal resistance for aluminum wall (R_{wall}) is negligible, and it is not considered in the overall thermal resistance. The thermal resistances in the air and liquid side due to

fouling are ignored in Eq. (4.27) since the microchannel heat exchanger core is new.

Combining Eq. (4.19) and Eq. (4.27), the overall thermal resistance equation can be expressed as

$$\frac{1}{UA} = \frac{1}{(\eta h A)_a} + \frac{1}{(h A)_w} \quad (4.28)$$

The air-side overall surface efficiency (η_a) which is used in Eq. (4.28) can be expressed as

$$\eta_a = 1 - \frac{A_f}{A_a} (1 - \eta_f) \quad (4.29)$$

$$\text{Where, } A_a = A_p + A_f \quad (4.30)$$

In the above Eq. (4.30) A_a is the total heat transfer area in the air-side, A_p is the primary surface area (exposed between fins), A_f is the surface area of fin, and η_f is the fin efficiency. The fin efficiency is evaluated from the following equation since plain rectangular wavy fins are used in the microchannel heat exchanger of the present study:

$$\eta_f = \frac{\tanh(ml)}{ml} \quad (4.31)$$

Where, fin parameter (m) is expressed as

$$m = \left(\frac{2h_a}{k_f \delta_f} \right)^{\frac{1}{2}} \quad (4.32)$$

In Eq. (4.30), k_f is the thermal conductivity of the fin material, and δ_f is the thickness of the fin. As the fin efficiency is the function of air-side heat transfer coefficient (h_a), an iterative method is applied to calculate the fin efficiency.

Nusselt Number (Nu_a)

Nusselt number is noticed as the dimensionless convection heat transfer coefficient. The air-side Nusselt number (Nu_a) expression as

$$Nu_a = \frac{h_a D_{h,a}}{k_a} \quad (4.33)$$

Stanton number (St_a)

The Stanton number is the dimensionless number representing heat transfer coefficient. It is expressed as

$$St_a = \frac{h_a}{G_a c_{p,a}} \quad (4.34)$$

Colburn Factor (j_a)

The Colburn factor is the modified Stanton number where moderate variation of Prandtl number takes into account. The air-side Colburn factor (j_a) is evaluated from following equation:

$$j_a = St_a \cdot Pr_a^{\frac{2}{3}} \quad (4.35)$$

CHAPTER V

RESULTS AND DISCUSSIONS

The main purposes of the current study were to obtain the heat transfer and fluid flow key parameters and their relationships. The special attentions were given on air-side of the microchannel heat exchanger during air cooling. The heat transfer and fluid flow important parameters such as average heat transfer rate (\dot{Q}), air-side Nusselt number (Nu_a), Colburn factor (j_a), pressure drop across the heat exchanger (ΔP_a) and friction coefficient (f_a) as well as the parameters concerned with the heat exchanger performance i.e. effectiveness (ϵ), number of transfer unit (NTU), and overall thermal resistance (R_{total}) were evaluated through experiment with a wide range of predefined operating conditions which are mentioned in Table 3.2.

The cold deionized water was passed in to the microchannels to cool the hot air during the hot air flowing through the finned spaces of the microchannel heat exchanger core. The hot air and the cold deionized water were maintained at a constant temperature of $38 \pm 0.5^\circ\text{C}$ and $9 \pm 0.5^\circ\text{C}$ respectively. The mass flow rates of deionized water were varied four levels (0.0169kg/s to 0.024kg/s) while the air face velocities were altered five steps (i.e. 1m/s to 5m/s) at each deionized water mass flow rates.

The Reynolds number ranges were found in the air and water-side as $283 \leq Re_a \leq 1384$ and $110 \leq Re_w \leq 152$ respectively. The following sections deliberated the effects of air and water-side Reynolds number on the mentioned heat transfer and fluid flow key parameters, and the general correlations were developed.

5.1 Heat transfer characteristics

The air-side heat transfer characteristics of the microchannel heat exchanger are investigated as well as discussed in this section. The effects of air and water-side Reynolds number on heat transfer key parameters are plotted in following sub-sections, and general correlations were achieved.

5.1.1 Heat transfer energy balance

The rate of heat energy released from the hot air and the rate of heat energy gained by cold deionized water should ideally be almost equal (i.e. $\dot{Q}_a \approx \dot{Q}_w$) but practically it is not occurred. In heat transfer process, there is always some difference between heat transfer rates of hot and cold side due to several reasons such as thermal resistances, heat gain or loss from or to the surroundings due to use of inadequate/improper heat insulation, experimental errors, etc. The difference between the rate of heat released by the hot air and the rate of heat gained by the cold deionized water in terms of percentage is referred to heat balance (HB) in the current study. The HB with respect to \dot{Q}_a is expressed as

$$HB_a = \frac{\dot{Q}_a - \dot{Q}_w}{\dot{Q}_a} \times 100 \quad (5.1)$$

The HB with respect to average heat transfer rate \dot{Q} is expressed as

$$HB_{avg} = \frac{\dot{Q}_a - \dot{Q}_w}{\dot{Q}} \times 100 \quad (5.2)$$

As per the recommendation of ASME PTC (ASME PTC 30-1991), the HB_{avg} value should not exceed 15%.

The \dot{Q}_a , \dot{Q}_w and \dot{Q} (the average heat transfer rate) were evaluated from the Eq.(4.15), (4.16) and (4.17) respectively. The heat balances with respect to air-side heat

transfer rate (HB_a) and water-side heat transfer rate (HB_{avg}) were computed from the Eq.(5.1) and (5.2) respectively. The effect of air-side Reynolds number on these two forms of heat balances are plotted in the Figure 5.1. The differences between the rate of heat released by the hot air and the rate of heat gained by the cold deionized water was within 4% which indicated that the heat loss to the surroundings was negligible due to proper heat insulation of the test section. The narrow size channels in the water-side offer more convective heat transfer, and the flat geometry of the microchannels slabs make good contact with the flowing hot air. These would lead to proficient heat balance in the current study.

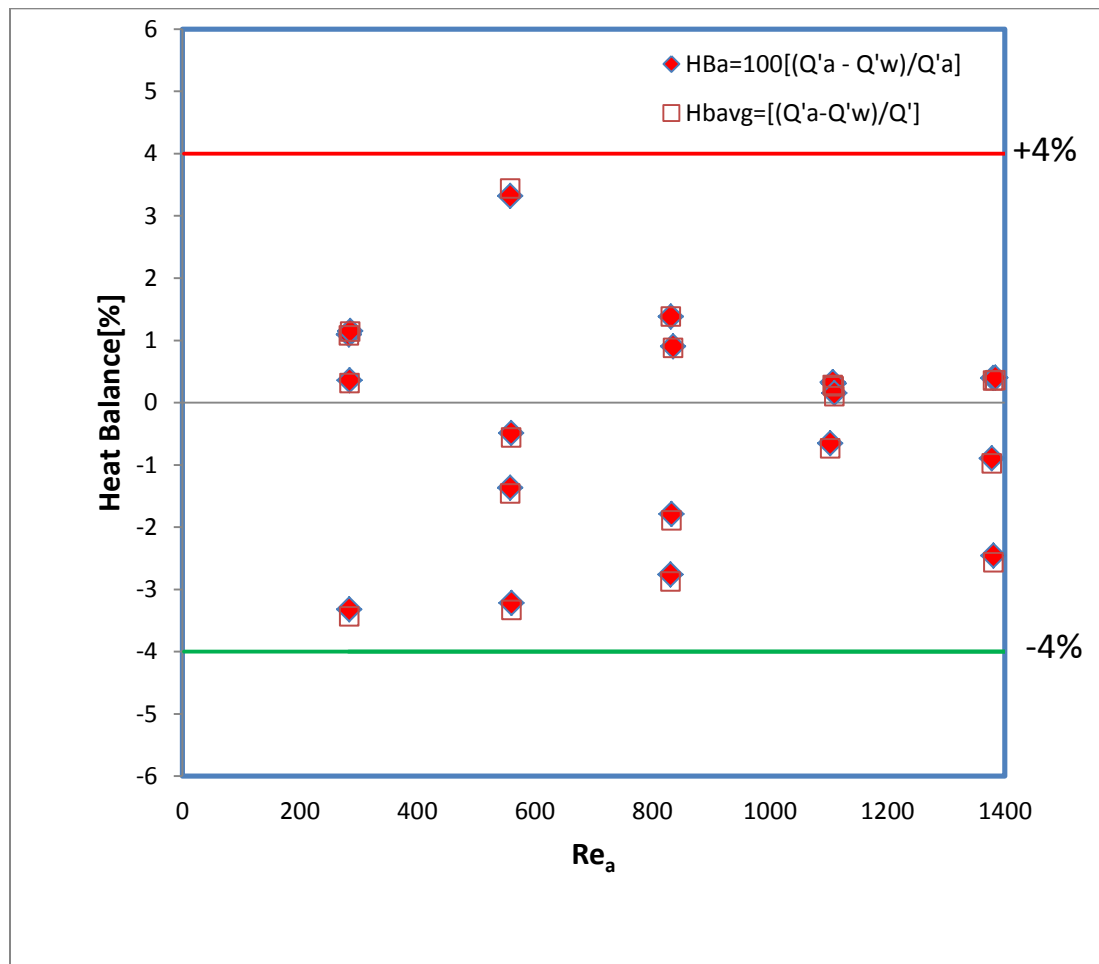


Figure 5.1: HB balance between hot air and cold deionized water

5.1.2 Effect of Reynolds number on heat transfer rate

The air-side Reynolds number was computed from the Eq. (4.23), and the experimental operations were performed in the laminar regime with the Reynolds number range of 283 to 1384. The water-side Reynolds number was calculated from the Eq. (4.11) within the range of 110-152. The heat transfer rates of air and water-side were evaluated from the overall energy balance Eq. (4.15) and Eq. (4.16) for hot air and cold water respectively. The arithmetic average of \dot{Q}_a and \dot{Q}_w were used to calculate the overall heat transfer rate from Eq. (4.17). The effect of air and water-side Reynolds number on heat transfer rate is presented in the Fig. 5.2. The heat transfer rate (\dot{Q}) increases with the increasing of air-side Reynolds number (Re_a) non-linearly as expected. All data are well fitted in the power law curve with good coefficient of determination value ($R^2 > 0.92$) at the following form

$$\dot{Q} = C_1 Re_a^{C_2} \quad 283 \leq Re_a \leq 1384 \quad (5.3)$$

Table 5.1: Coefficients of determination, curve fit coefficients of Fig. 5.2.

Re_w	C_1 (Watt)	C_2	R^2
110	539.37	0.1756	0.924
121	614.49	0.1703	0.950
129	608.84	0.1819	0.959
152	550.20	0.2128	0.953

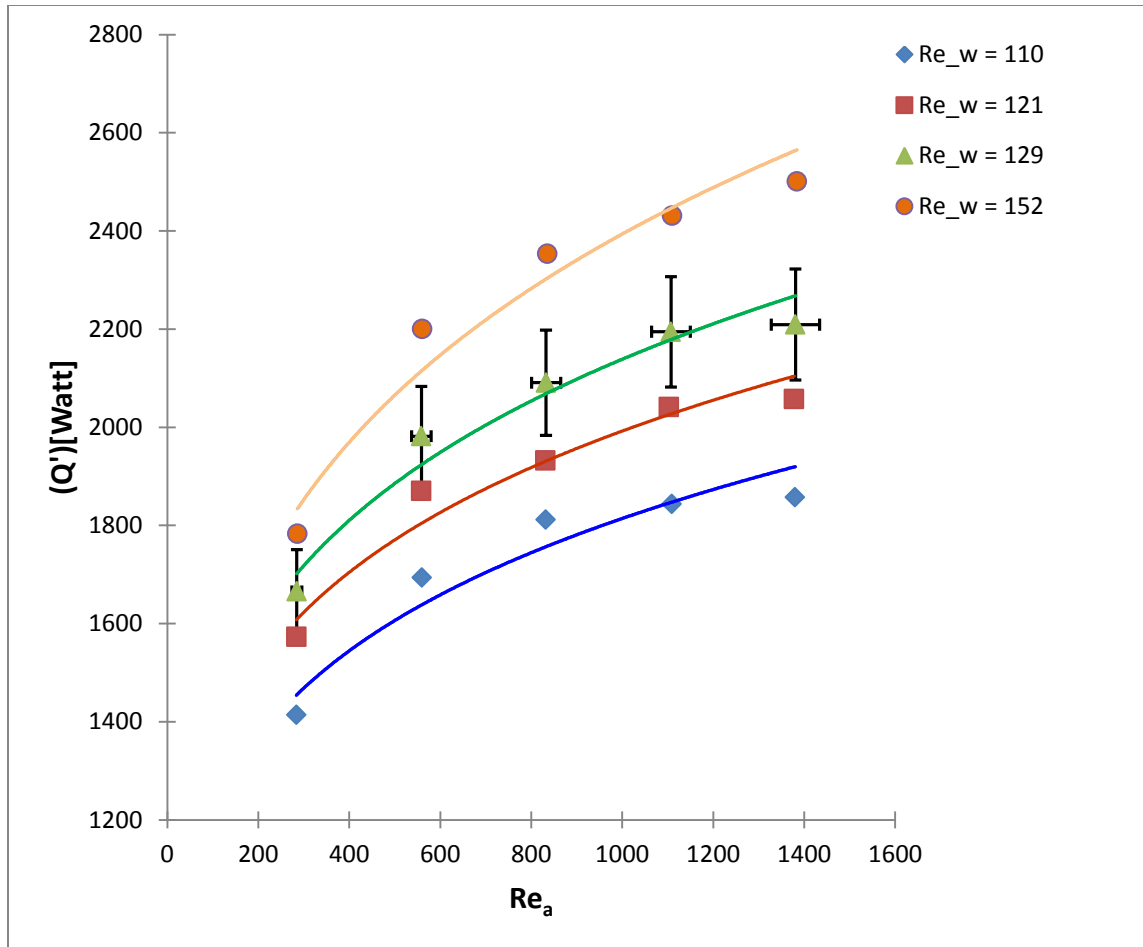


Figure 5.2: The effect of air and water-side Reynolds number (Re_a and Re_w) on average heat transfer rate (\dot{Q})

The coefficients of determinations values are mentioned in the Table-5.1. The initial slopes of all curves have much greater than the ends. The end slope is much higher for highest water-side Reynolds number curve. The Fig. (5.2) also indicates the significance effect of water-side Reynolds number on heat transfer rate. The higher water-side Reynolds number shows higher heat transfer rate in a particular air-side Reynolds number. The convection heat transfer increases with increasing the mass flow rates of water as desired.

5.1.2.1 Comparison to the heat transfer correlation with experimental data

All data points are plotted in the Fig.5.3, and the general correlation for average heat transfer rate and air-side Reynolds number is obtained as

$$\dot{Q} = 575.83 Re_a^{0.1855} \quad 283 \leq Re_a \leq 1384 \quad (5.4)$$

The Fig.5.2 depicts that 90% experimental data fall within $\pm 10\%$ of the current correlation of the Reynolds number range of $283 \leq Re_a \leq 1384$. Therefore, the general correlation equation [Eq.(5.3)] can predict 90% of experimental data within $\pm 10\%$.

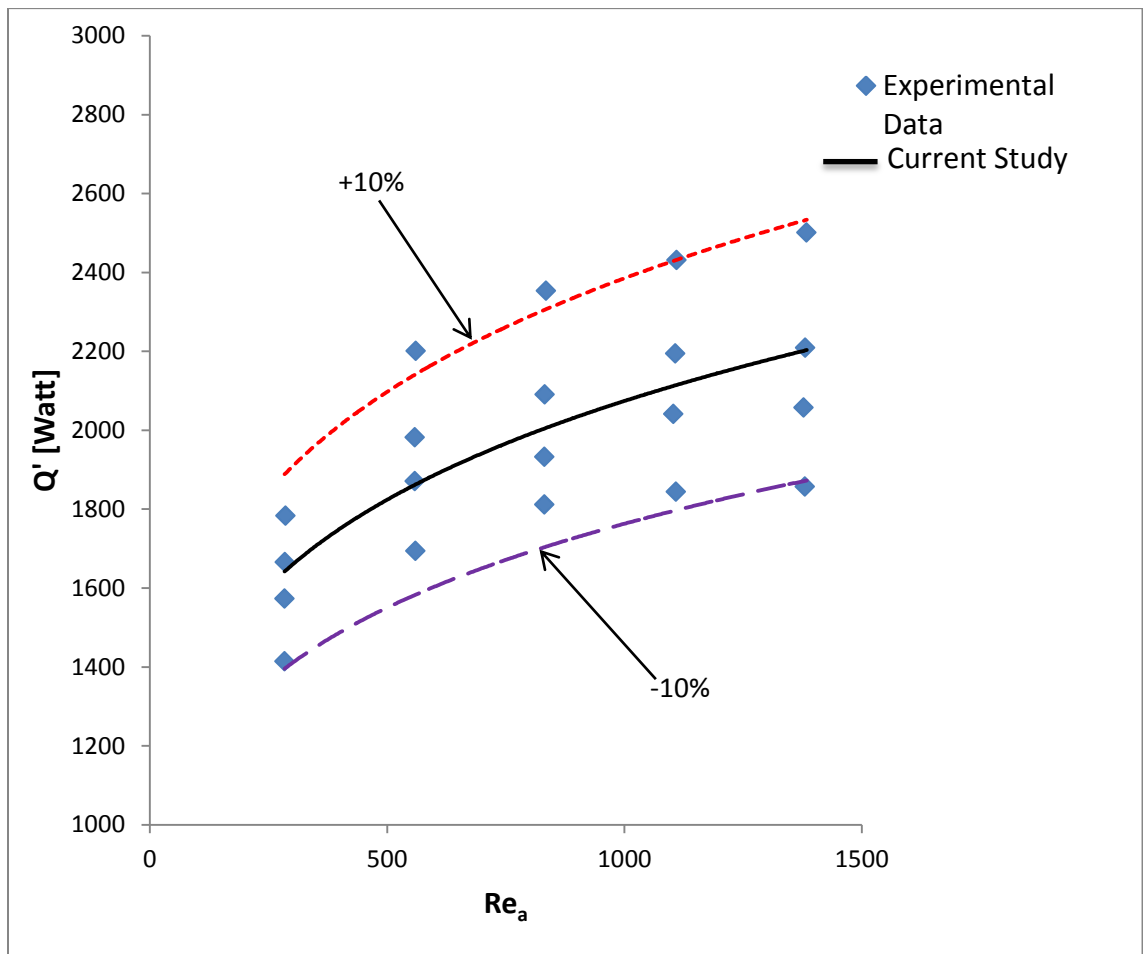


Figure: 5.3: Comparison to the current correlation with experimental data

5.1.3 Effect of Reynolds number on Nusselt number

Nusselt number is a dimensionless heat transfer coefficient which is generally used to represent the heat transfer. It is widely expressed the heat transfer in terms of Nusselt number as the function of Reynolds number. Air-side Nusselt numbers were computed from Eq. (4.33). The effect of air-side as well as water-side Reynolds number (Re_a and Re_w) on air-side Nusselt number (Nu_a) in the region of air-side Reynolds number 283-1384 are plotted in Fig. 5.4.

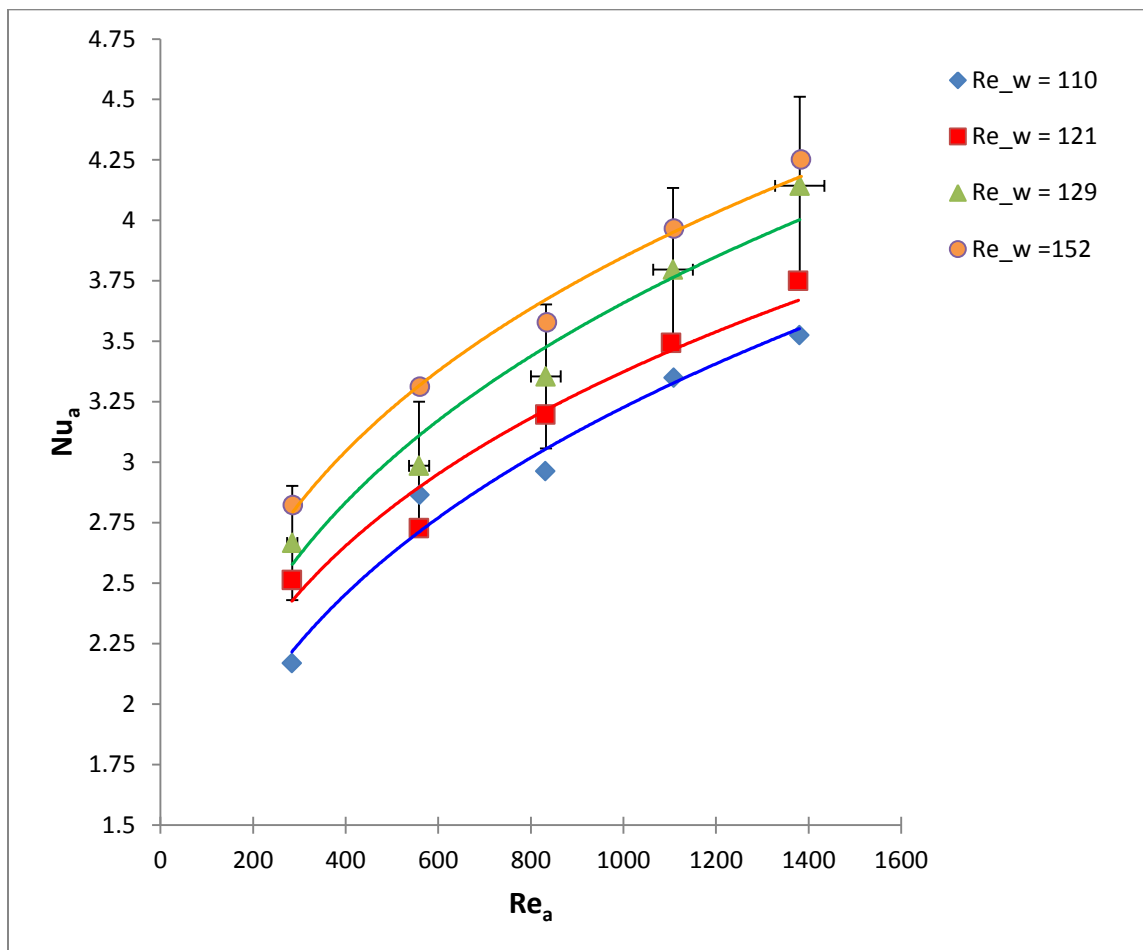


Figure 5.4: The effect of air and water-side Reynolds number ($Re_{e,a}$ and $Re_{e,w}$) on air-side Nusselt number(Nu_a)

In Figure 5.4, all experimental data are rationally fitted in the power law curve with good coefficient of determination value ($R^2 > 0.95$) in the following form

$$Nu_a = C_1 Re_a^{C_2} \quad 283 \leq Re_a \leq 1384 \quad (5.5)$$

Table 5.2: Coefficients of determination, curve fit coefficients corresponding

Re_w	C_1	C_2	R^2
110	0.4107	0.2984	0.9692
121	0.5527	0.2619	0.9516
129	0.5335	0.2787	0.9576
152	0.6587	0.2556	0.9890

Fig. 5.4 illustrates that air-side Nusselt number (Nu_a) increases with the increasing of air-side Reynolds number in power law curve. The Nusselt number (Nu_a) is larger at higher water-side Reynolds number (Nu_w) for a certain air-side Reynolds number since more heat is transferred due to convection at higher water-side Reynolds number (Re_w).

5.1.3.1 Comparison to the Nusselt number –Reynolds number correlation with data

The Nu_a - Re_a general correlation is obtained by combining all operating conditions (all data points) through the power law curve as in the form $Nu_a = C (Re_a)^n$ [$0 < n < 1$ and $C > 0$].

$$Nu_a = 0.5303(Re_a)^{0.274} \quad 283 \leq Re_a \leq 1384 \quad (5.6)$$

The Nu_a - Re_a correlation in the current study [Eq. (5.6)] can predict almost all experimental data points within $\pm 10\%$, and this is shown in the Fig.5.5.

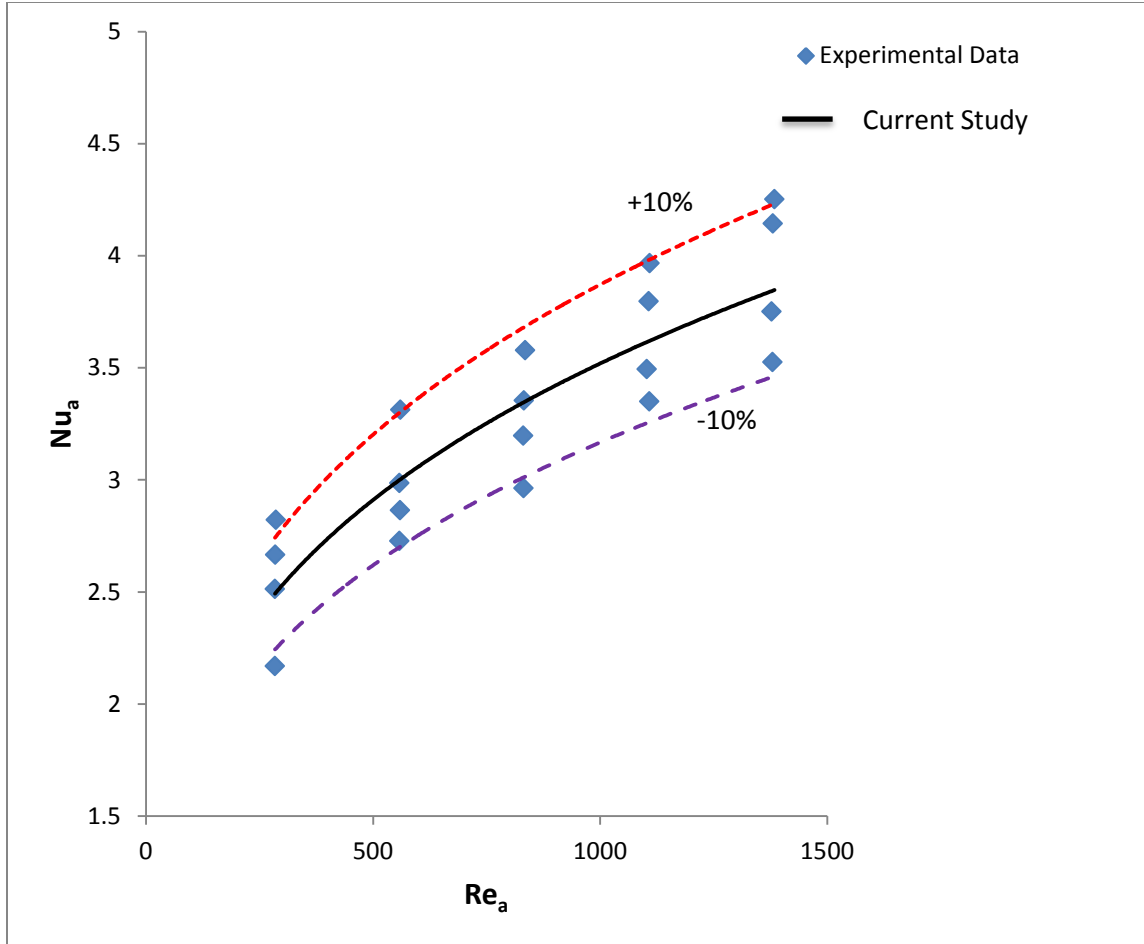


Figure 5.5: Comparison of correlation (Nu_a - Re_a) and experimental data

5.1.3.2 Comparison of Nusselt number-Reynolds number-Prandtl number with others

The heat transfer expression in the form of Nusselt number as the function of Reynolds number and Prandtl number is commonly used. The effect of air-side Reynolds number and Prandtl number on air-side Nusselt number are plotted in the Fig.5.6. The air-side heat transfer general correlation is obtained in the form of Nusselt number as the function of air-side Reynolds number and Prandtl number as

$$Nu_a = 0.5925Re_a^{0.2743} Pr_a^{\frac{1}{3}} \quad 283 \leq Re_a \leq 1384 \text{ and } 0.70 < Pr_a < 0.72 \quad (5.7)$$

The air-side heat transfer correlations for microchannel heat exchangers are rare in open literature. The Nu_a - Re_a - Pr_a correlation [Eq. (5.7)] in the current study is compared to two correlations which are proposed for the air-side of conventional cross-flow heat exchanger. Taler (2005) developed air-side heat transfer correlation for automotive radiators in the Reynolds number range of $200 \leq Re_a \leq 1500$, as

$$Nu_a = 0.05683 Re_a^{0.6289} Pr_a^{\frac{1}{3}} \quad 200 \leq Re_a \leq 1500 \text{ and } 0.5 < Pr_a < 100 \quad (5.8)$$

The radiator had two rows of oval shape tube with inline arrangement having $d_{\min}=6.35\text{mm}$ and $d_{\max}=11.82\text{mm}$. Tang and Yang (2005) experimentally investigated the heat transfer characteristics of a single row aluminum fin and tube cross-flow heat exchanger, and they recommended the heat transfer correlation for air-side as

$$Nu_a = 0.05683 Re_a^{0.6289} Pr_a^{\frac{1}{3}} \quad 120 \leq Re_a \leq 480 \text{ and } 0.5 < Pr_a < 100 \quad (5.9)$$

The effect of air-side Reynolds number and Prandtl number on air-side Nusselt number of the current study is compared to the correlations of Taler (2005) and Tang & Yang (2005) in Figure 5.6. The figure illustrates that the value of air-side Nusselt number of the current study is higher up to the air-side Reynolds number range of 1384 but the Taler correlation shows higher Nusselt number after this Reynolds number range. The figure also shows that the slope of the Taler correlation curve is higher compared to the correlation of the current study.

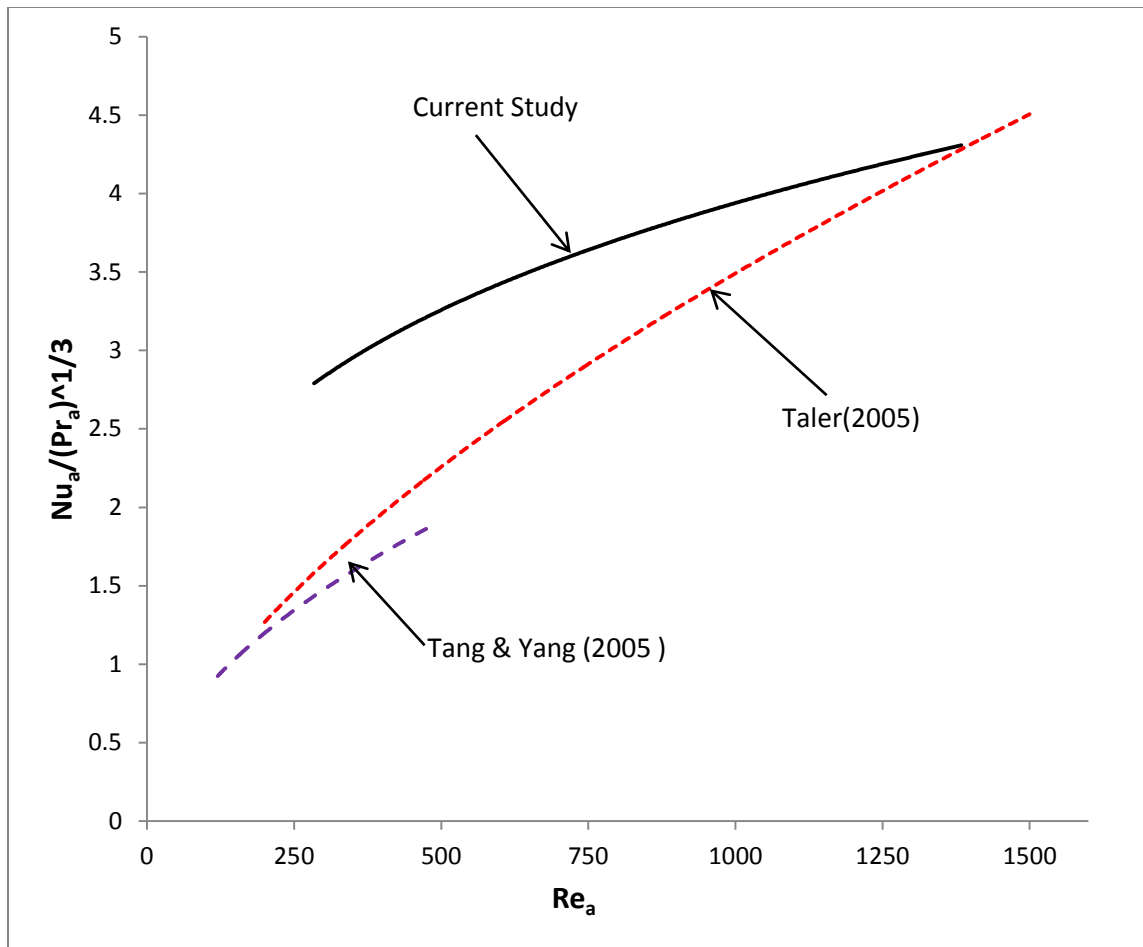


Figure 5.6: Comparison to the current correlation ($Nu_a-Re_a-Pr_a$) with other correlations

Taler (2005) also conducted the numerical simulation of the heat exchanger by using the CFD program. The higher heat transfer rate was observed near the base of the fin and at the frontal part of tube circumference in the first row. The weak heat transfer rate was witnessed behind the tube where low velocity wake region exist. The heat transfer rate was found especially low at the second row tubes due to the presence of wakes in the front and behind the tube. However, such wake effects are insignificant for multiport microchannel slab geometry in the current study since channels are embedded in the slab. The multiport microchannel slab offers flat heating surface at the top and

bottom faces of the slab. Thus it allows the flowing air to make very well contact with the heating surfaces as well as provides uniform temperature distribution throughout the heat exchanger core. These could lead to higher heat transfer over the mentioned radiator of isolated tube rows for experimental Reynolds number range.

5.1.4 Effect of Reynolds number on Colburn factor

The air-side Colburn factor (j_a) is also a heat transfer dimensionless parameter which is often used to express to characterize the heat transfer of heat exchangers. The Colburn factors were evaluated in the current study from Eq. (4.35). The Colburn factor (j_a) versus Re_a are plotted in Fig.5.7 for all operating conditions. The figure shows the effect of air and water-side Reynolds number on air-side Colburn factor.

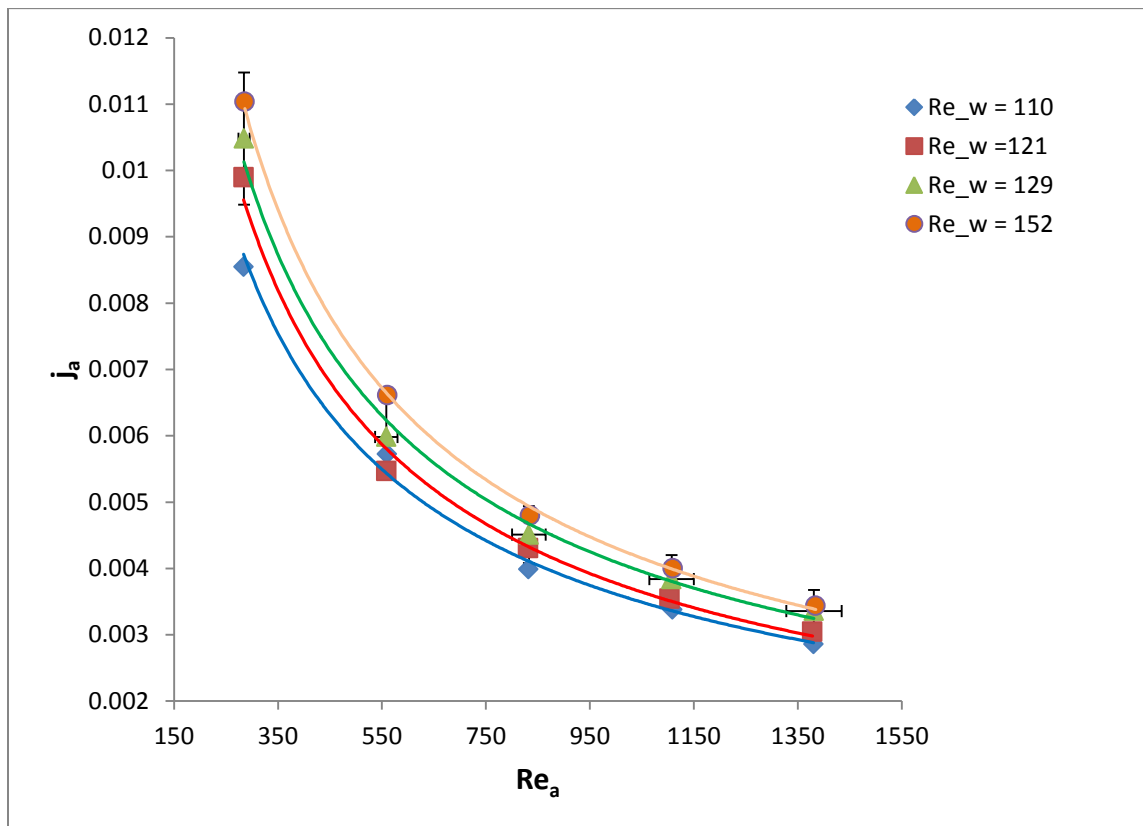


Figure 5.7: The Effect of air and water-side Reynolds number (Re_a and Re_w) on air-side Colburn factor (j_a)

The Fig.5.7 illustrates that the air-side Colburn factor (j_a) decreases with increasing air-side Reynolds number in power law curve with negative exponent. The value of j_a is higher at higher water-side Reynolds number for a particular Re_a . The figure also indicates that the ends of the all four curves are much closer than beginning. The j_a - Re_a general correlation is obtained by combining all operating conditions (all data points) through the power law curve as

$$j_a = 0.5925(Re_a)^{-0.726} \quad 283 \leq Re_a \leq 1384 \quad (5.10)$$

The Fig.5.8 shows the experimental data and the correlation of current study. The current j_a - Re_a correlation [Eq. (5.10)] can predict all experimental data within $\pm 10\%$.

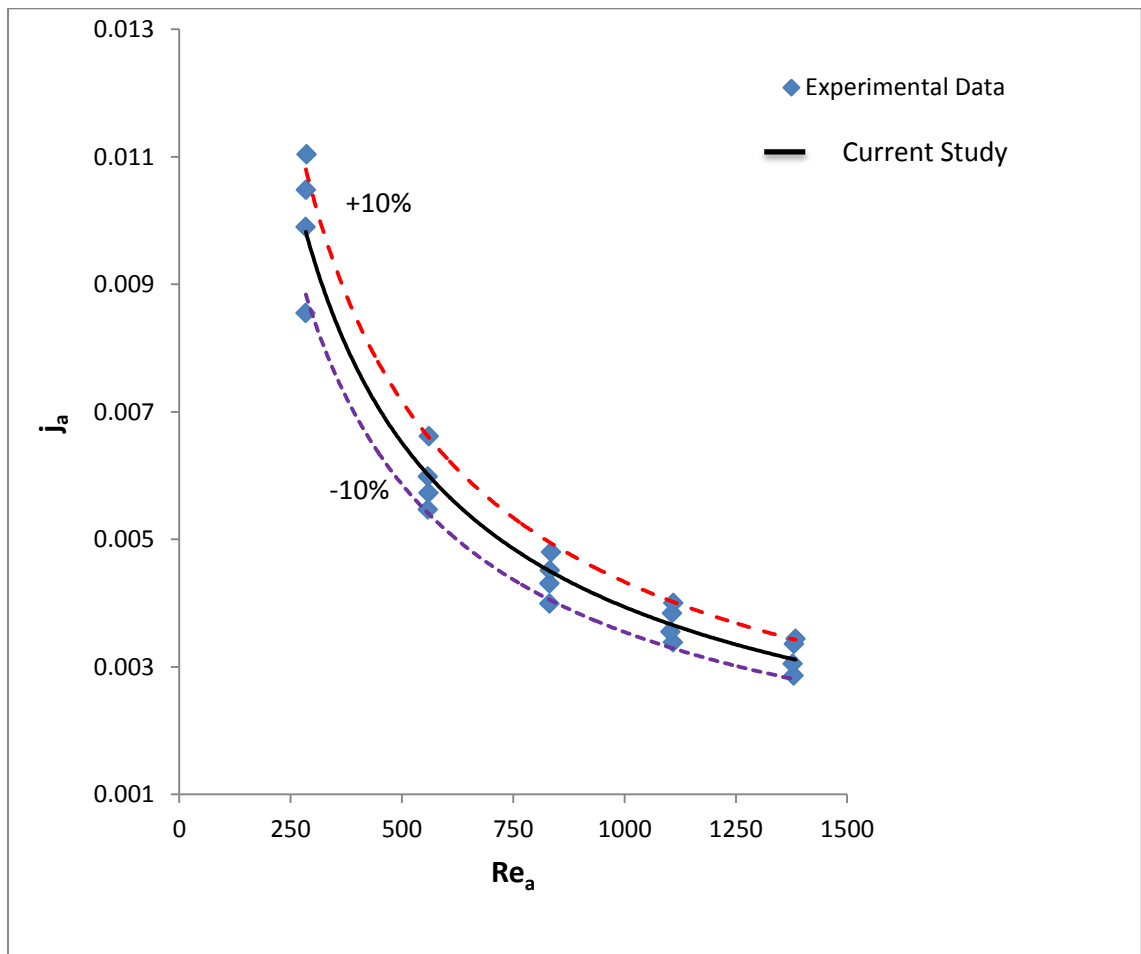


Figure 5.8: Comparison to current j_a - Re_a correlation with experimental data

5.2 Fluid flow analysis

Air-side flow characteristics are analyzed in this section. During the experiment the hot air was passed into the microchannel heat exchanger core where it transferred heat to the cold deionized water via finned and slab surfaces. The effects of air and water-side Reynolds number on air-side pressure drop and friction factor are examined here as well as general correlations are proposed.

5.2.1 Effect of Reynolds number on air-side pressure drop

The air-side pressure drop (ΔP_a) across the microchannel heat exchanger core was measured through the data acquisition system in combination with differential pressure transducers. The air-side Reynolds number (Re_a) was computed by the air-side hydraulic diameter of the microchannel heat exchanger core. The Eq. (4.25) was used to compute the air-side hydraulic diameter ($D_{h,a}$) which is proposed by Kays and London(1984) for air-side matrix flow passages. The air-side pressure drop (ΔP_a) versus air-side Reynolds number (Re_a) is plotted in the Fig.5.9. The figure indicates the effect of air and water-side Reynolds number on air-side pressure drop. The air-side pressure drop (ΔP_a) increases with increasing the air-side Reynolds number in non-linearly with power law curve because higher air velocity increases the frictional losses. There is a minor effect of water-side Reynolds number (Re_w) on air-side pressure drop since the water mass flow rates does not make significant change on air density. There is a slight gap among the curves at the beginning but little more gaps are observed at end of the curves. A general ΔP_a - Re_a correlation is obtained by combining all experimental data as

$$\Delta P_a = 0.0068 Re_a^{1.3825} \quad 283 \leq Re_a \leq 1384 \quad (5.11)$$

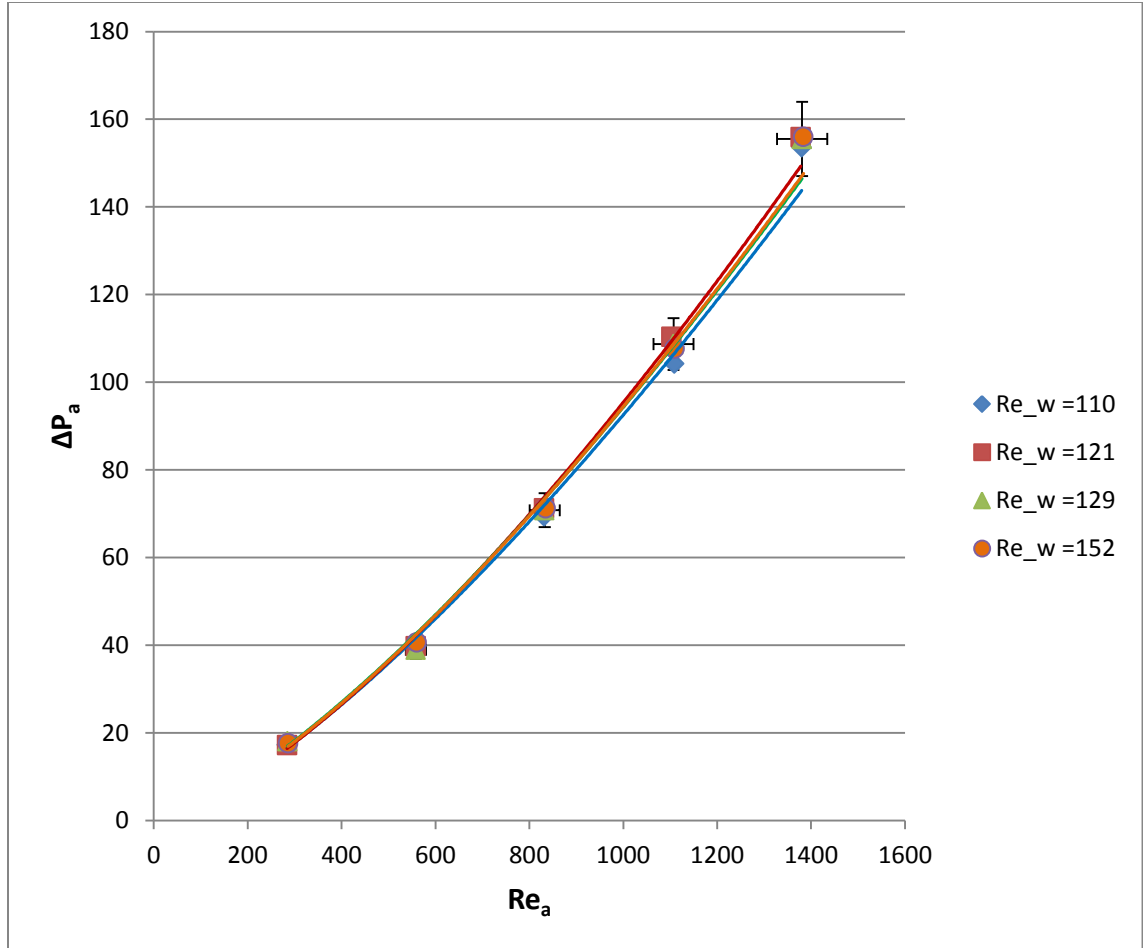


Figure 5.9: The effect of air and water-side Reynolds number (Re_a and Re_w) on air-side core pressure drop (ΔP_a)

5.2.2 Effect of Reynolds number on friction factor

The pressure drop in terms of friction factor is frequently used to analyze flow characteristics. The air-side friction factor in the current study was evaluated from the Eq. (4.26) which is suggested by Kays and London (1984) for air-side matrix flow passages. The effects of air-side and water-side Reynolds number (Re_a and Re_w) on air-side friction factor (f_a) are plotted in Fig.5.10. The Fig.5.10 depicts that the air-side friction factor increases with increasing air-side Reynolds number in power law curve with negative exponent.

The figure also illustrates that the effects of water-side Reynolds numbers have a minor influence on air-side friction factor, and all curves are little bit separate from each other at the beginning but they are very close at end.

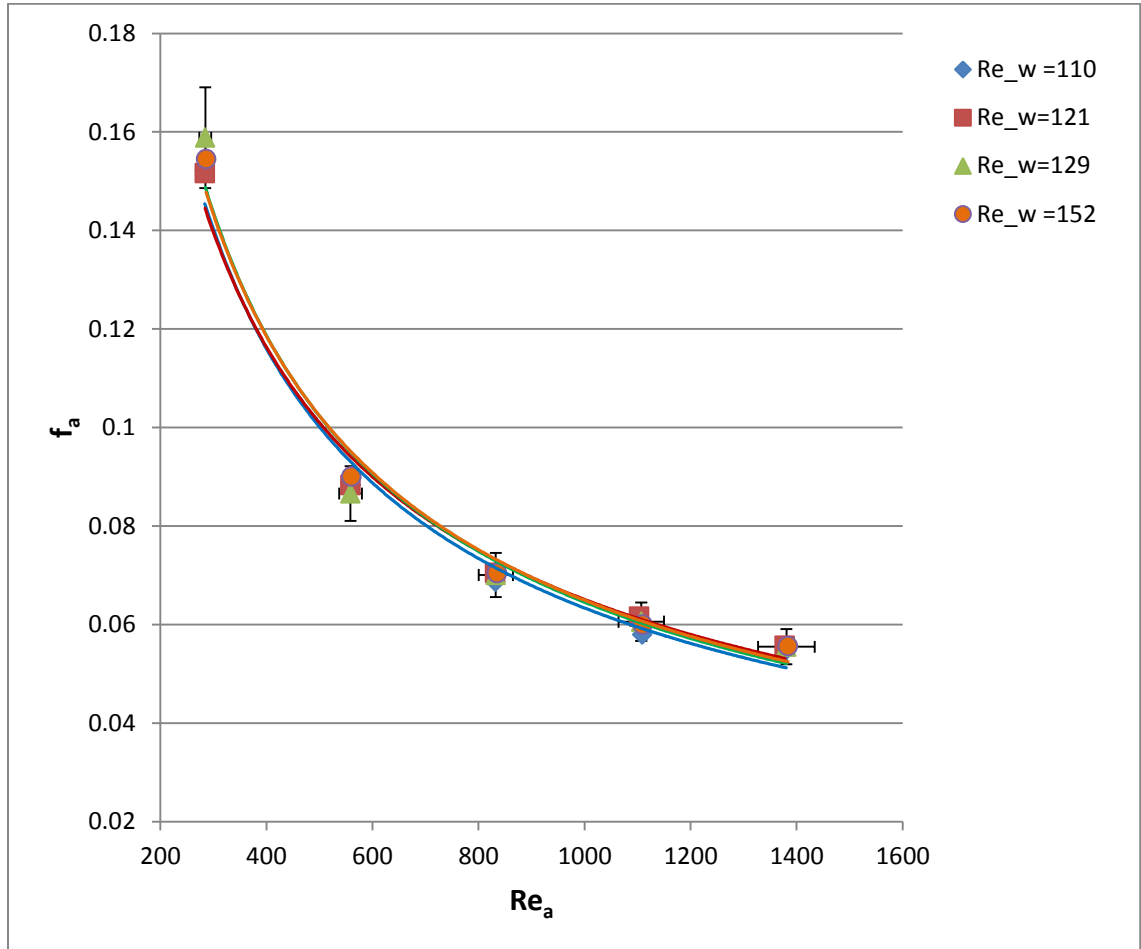


Figure 5.10: The effect of air and water-side Reynolds number (Re_a and Re_w) on air-side friction factor (f_a)

The f_a - Re_a general correlation is obtained by combining all operating conditions through the power law curve as

$$f_a = 5.6619(Re_a)^{-0.646} \quad 283 \leq Re_a \leq 1384 \quad (5.12)$$

The Fig.5.11 shows the experimental data and the f_a - Re_a correlation of current study.

The current f_a - Re_a correlation [Eq. (5.12)] can predict all experimental data within $\pm 10\%$.

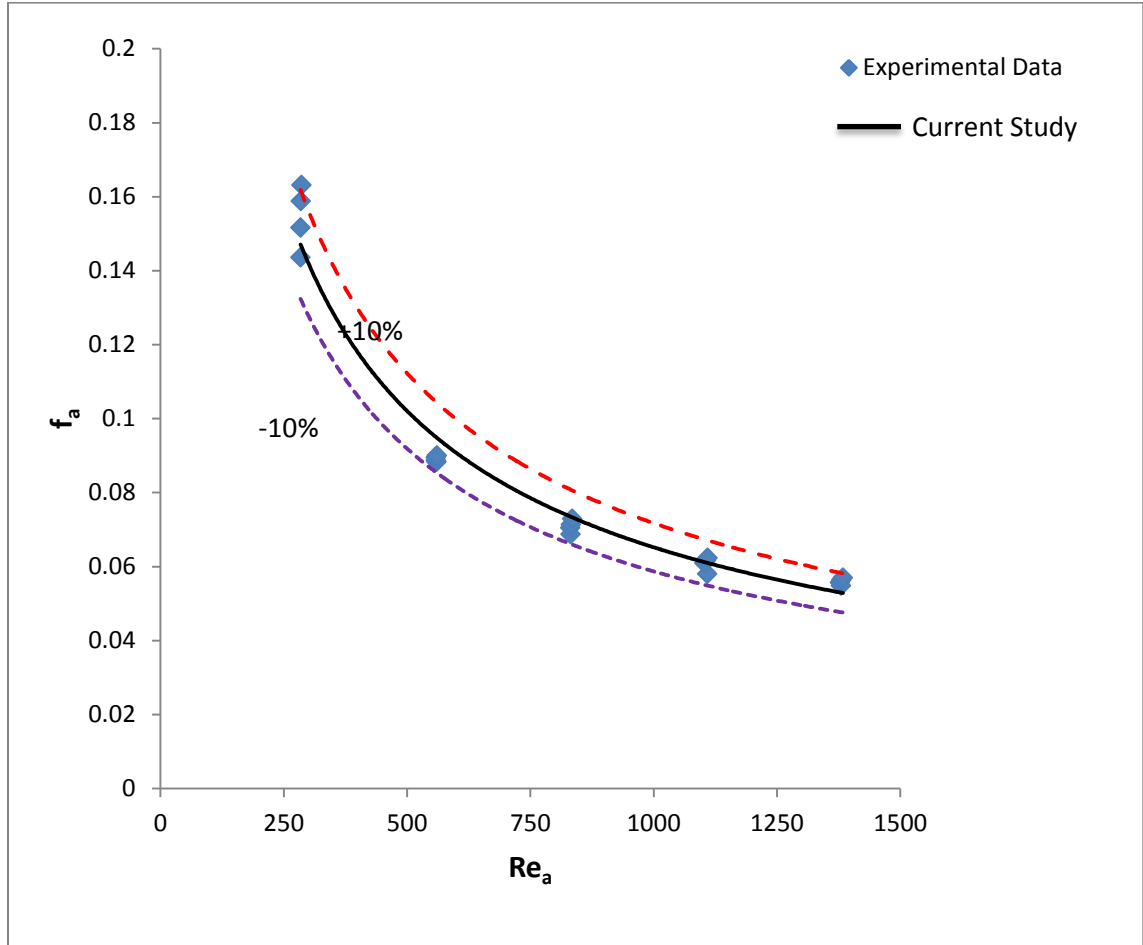


Figure 5.11: Comparison to current f_a - Re_a correlation with experimental data

5.3 MCHX performance characteristics

The parameters concerned with microchannel heat exchanger performances such as overall thermal resistance, effectiveness, NTU are examined in this section. The air-side and water-side Reynolds number on these parameters as well as other issues are analyzed and discussed in the following subsections.

5.3.1 Effect of Reynolds number on overall thermal resistance

The air-side thermal resistance dictates the overall thermal resistance on typical air to liquid cross-flow exchangers (Wang, C.C. 2000).The overall thermal resistance is

evaluated from the Eq. (4.19). The influence of air and water-side Reynolds number on overall thermal resistance is illustrates in Fig.5.12. The overall thermal resistance (R_{total}) decreases with the increasing of air-side Reynolds number Re_a in power law relation with negative exponent. The lower water-side Reynolds number (Re_w) has higher thermal resistance at a certain air-side Reynolds number (Re_a). The air-side thermal resistance is found the major part of overall thermal resistance. The range of air-side thermal resistance became 89% - 94% of overall thermal resistance those are quite consistent with other findings.

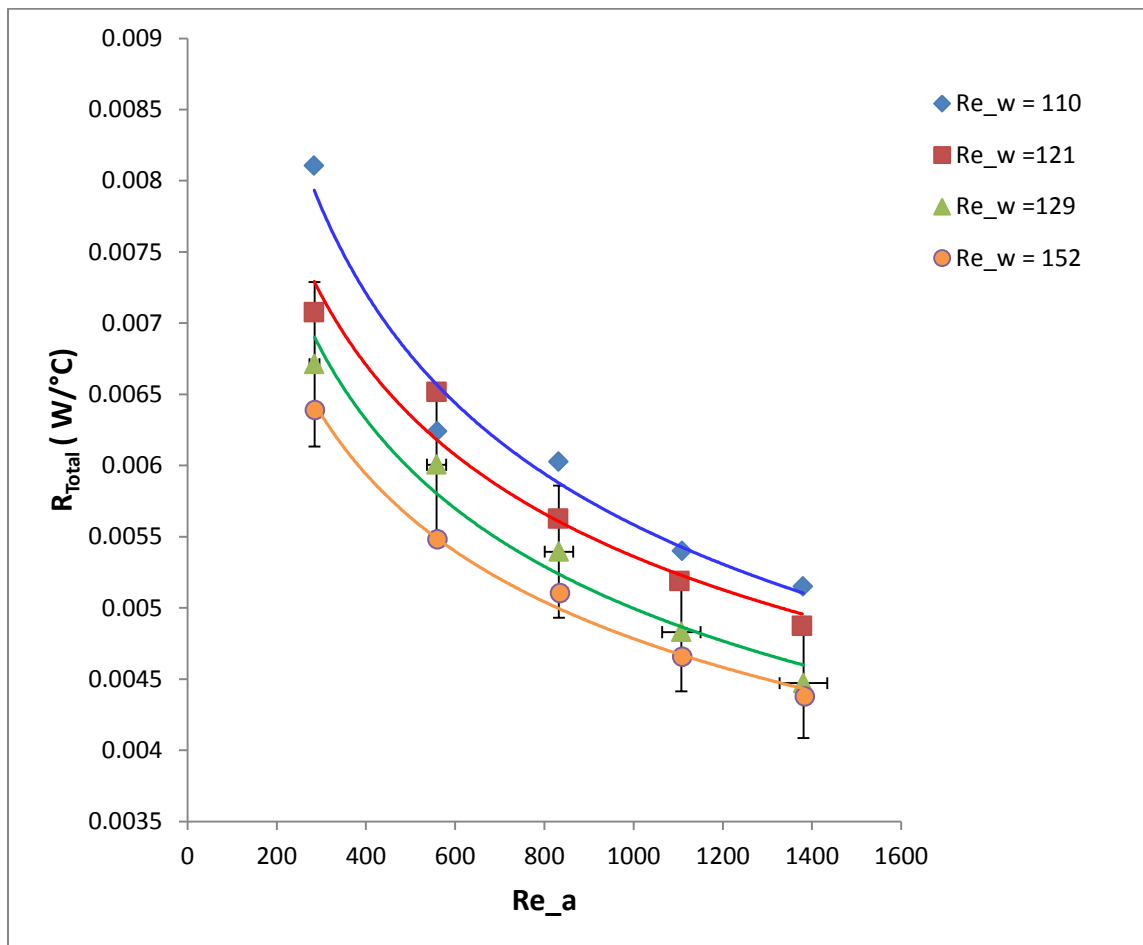


Figure 5.12: The effect of air and water-side Reynolds number (Re_a and Re_w) on overall thermal resistance (R_{Total})

The R_{Total} - Re_a general correlation is obtained by combining all operating conditions (all data points) through the power law curve as

$$R_{Total} = 0.03 (Re_a)^{-0.254} \quad 283 \leq Re_a \leq 1384 \quad (5.13)$$

The R_{total} - Re_a correlation in the current study [Eq. (5.13)] can predict almost all experimental data points within $\pm 10\%$, and this is shown in the Fig.5.13.

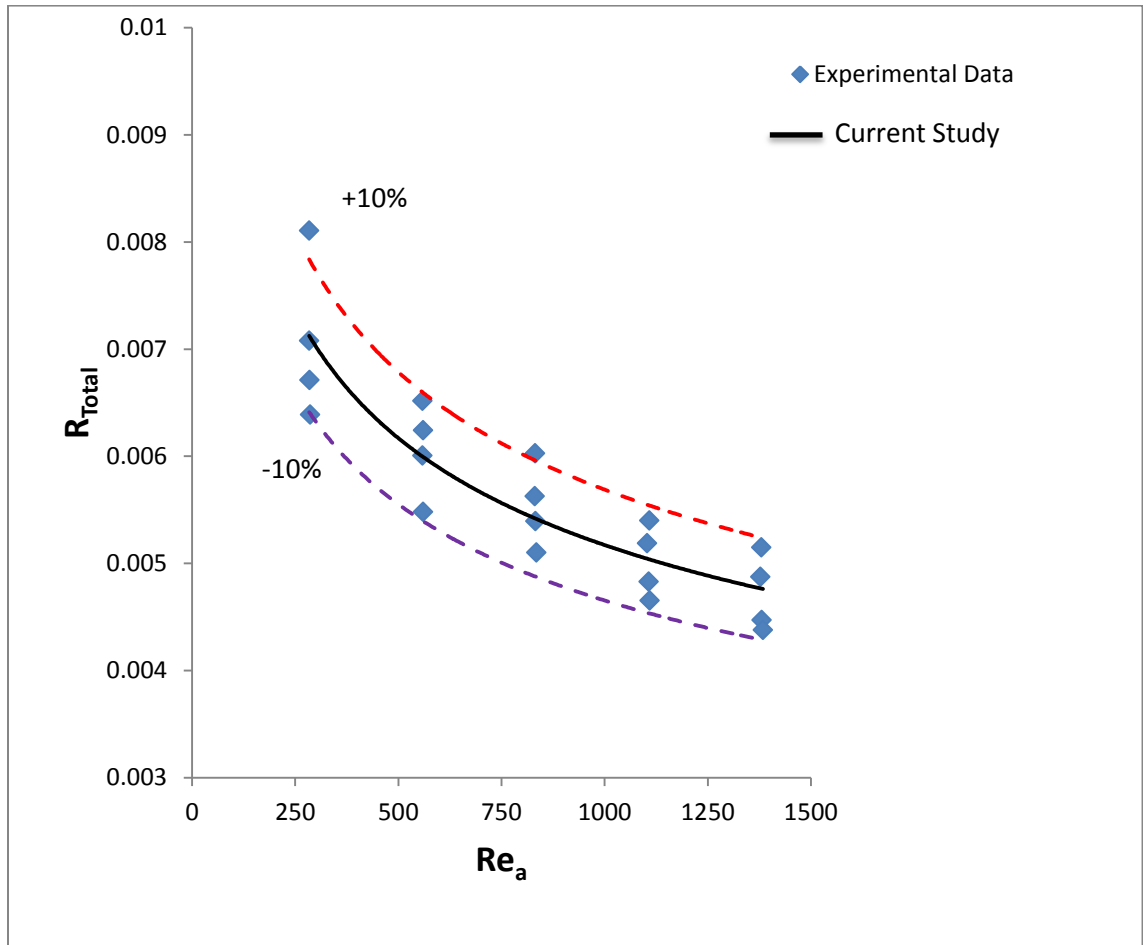


Figure 5.13: Comparison to current R_{Total} - Re_a correlation with experimental data

5.3.2 Effect of Reynolds number on effectiveness

The effectiveness (ϵ) of MCHX of the current study is calculated from the Eq. (4.21). The effectiveness versus air-side Reynolds number is plotted in the Fig.5.14. The

figure illustrates the effect of air and water-side Reynolds number (Re_a and Re_w) on effectiveness (ϵ). The effectiveness increases with increasing of air-side Reynolds number in power law curve. Initially, the slopes of the curves are greater than end. The water-side Reynolds number has significance influence on effectiveness. The lower water-side Reynolds number has higher effectiveness for a particular air-side Reynolds number because the lower water mass flow rate reduces the minimum heat capacity rate $[(\dot{m}c_p)_{min}]$ which leads to higher effectiveness.

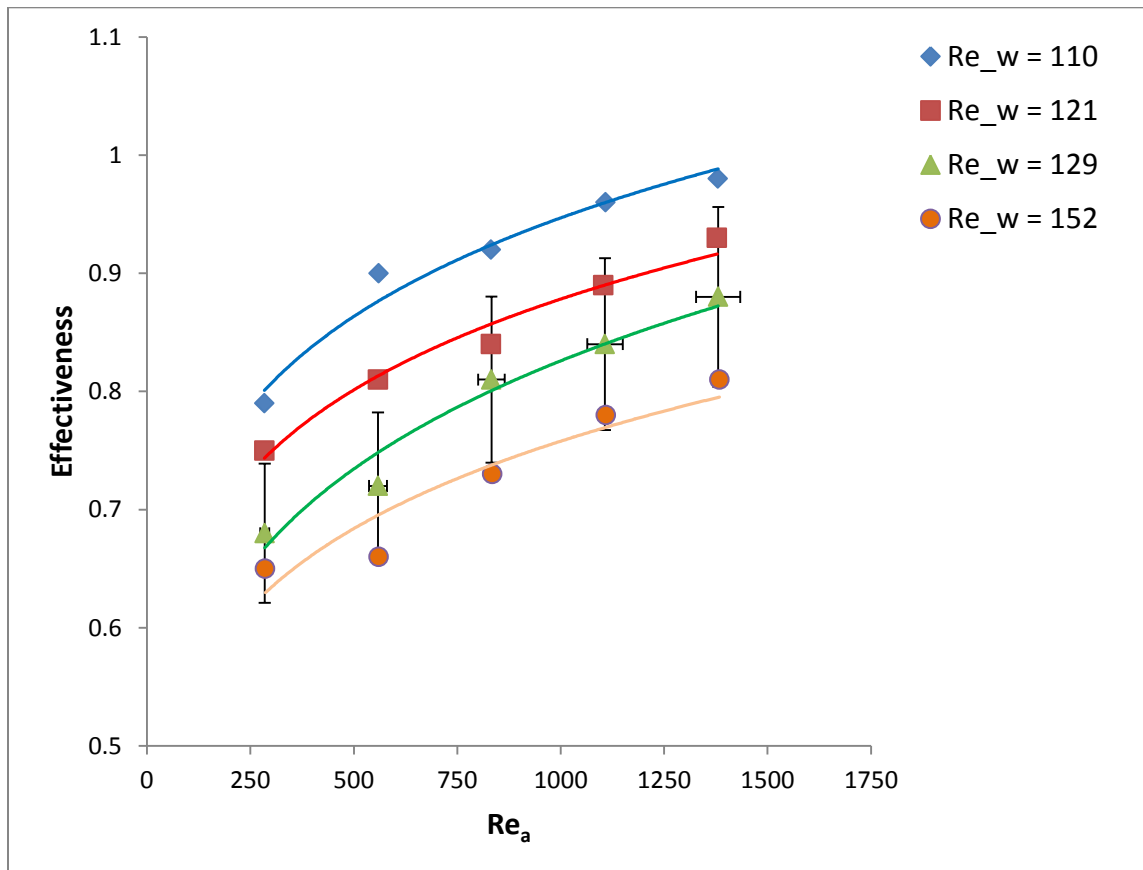


Figure 5.14: The effect of Re_a and Re_w on effectiveness (ϵ)

The ϵ - Re_a general correlation is obtained by combining all operating conditions (all data points) through the power law curve as

$$\epsilon = 0.3113(Re_a)^{0.1453} \quad 283 \leq Re_a \leq 1384 \quad (5.14)$$

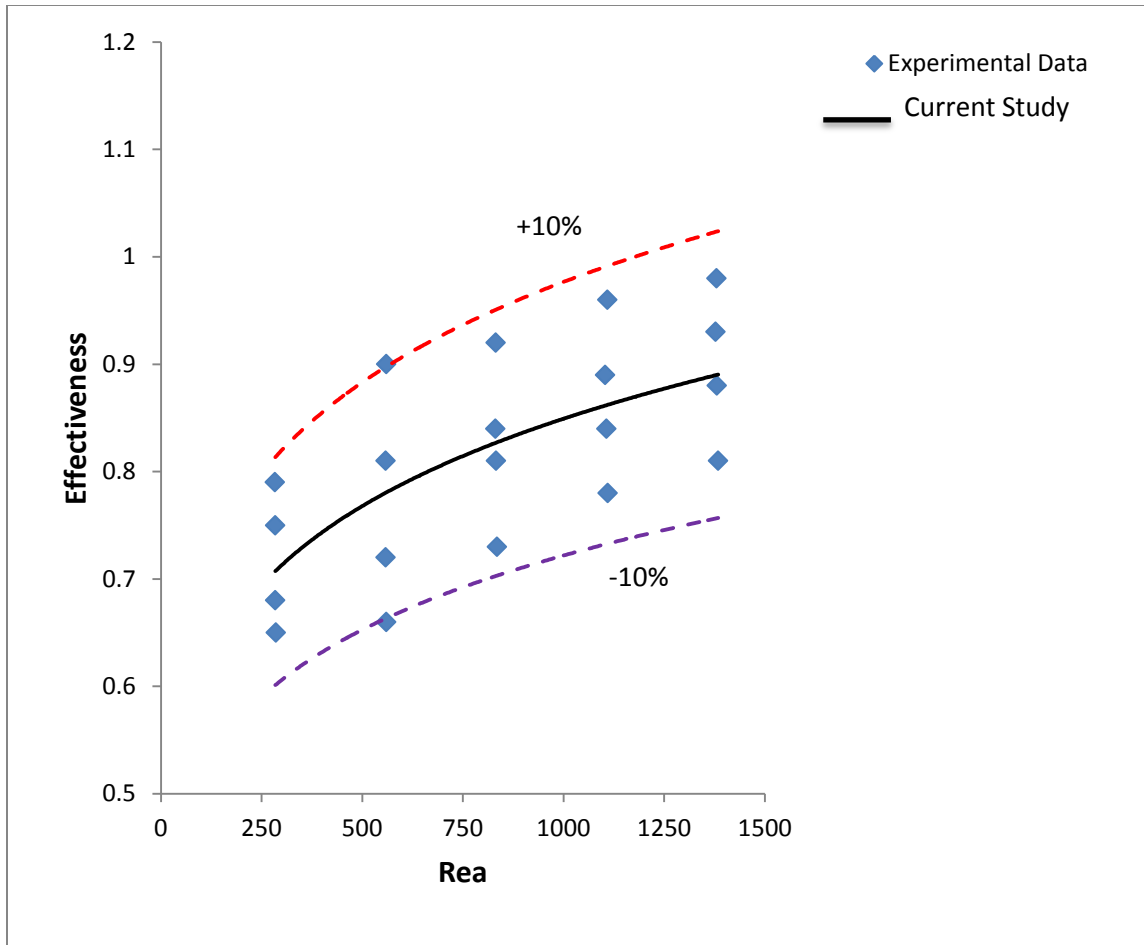


Figure 5.15: Comparison to current ε - Re_a correlation with experimental data

5.3.3 Effect of Reynolds number on NTU

The NTU values of MCHX are evaluated from the Eq. (4.22), and these NTUs are plotted against air-side Reynolds number in the Fig.5.16. The figure indicates the effects of air and water-side Reynolds number on NTU. The NTU increases with increasing of air-side Reynolds number non-linearly. The curves are closer at the beginning than the ending. The Fig. 5.16 also shows that water-side Reynolds number has much influence on NTU. The NTU value is higher at higher water-side Reynolds number for certain air-side Reynolds number because the impact of mass flow rate of water on NTU value. The general correlation is obtained from the experimental data by power law method as

$$NTU = 0.3336(Re_a)^{0.279} \quad 283 \leq Re_a \leq 1384 \quad (5.15)$$

The NTU- Re_a correlation equation [Eq. (5.15)] can predict all experimental data within $\pm 10\%$, and it is shown in Fig.5.17.

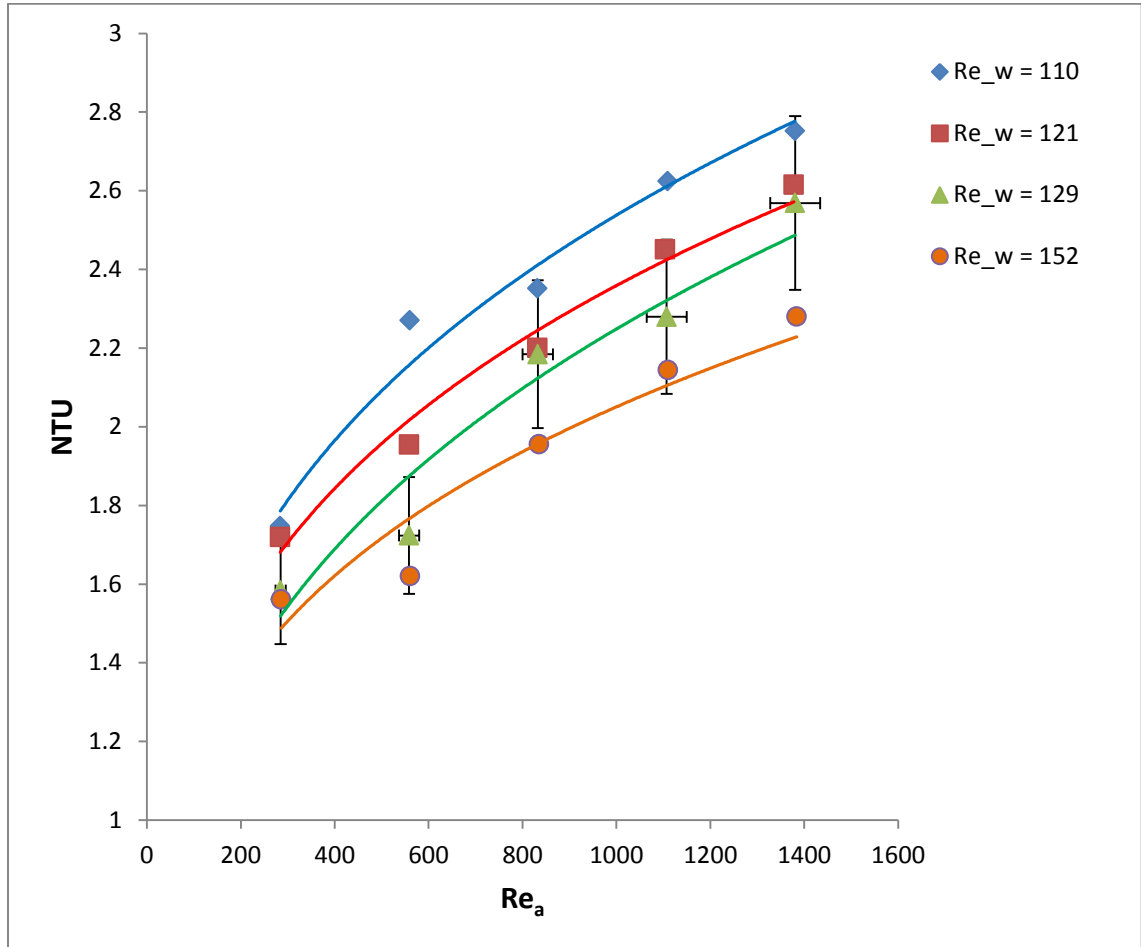


Figure 5.16: The effect of air and water-side Reynolds number (Re_a and Re_w) on NTU

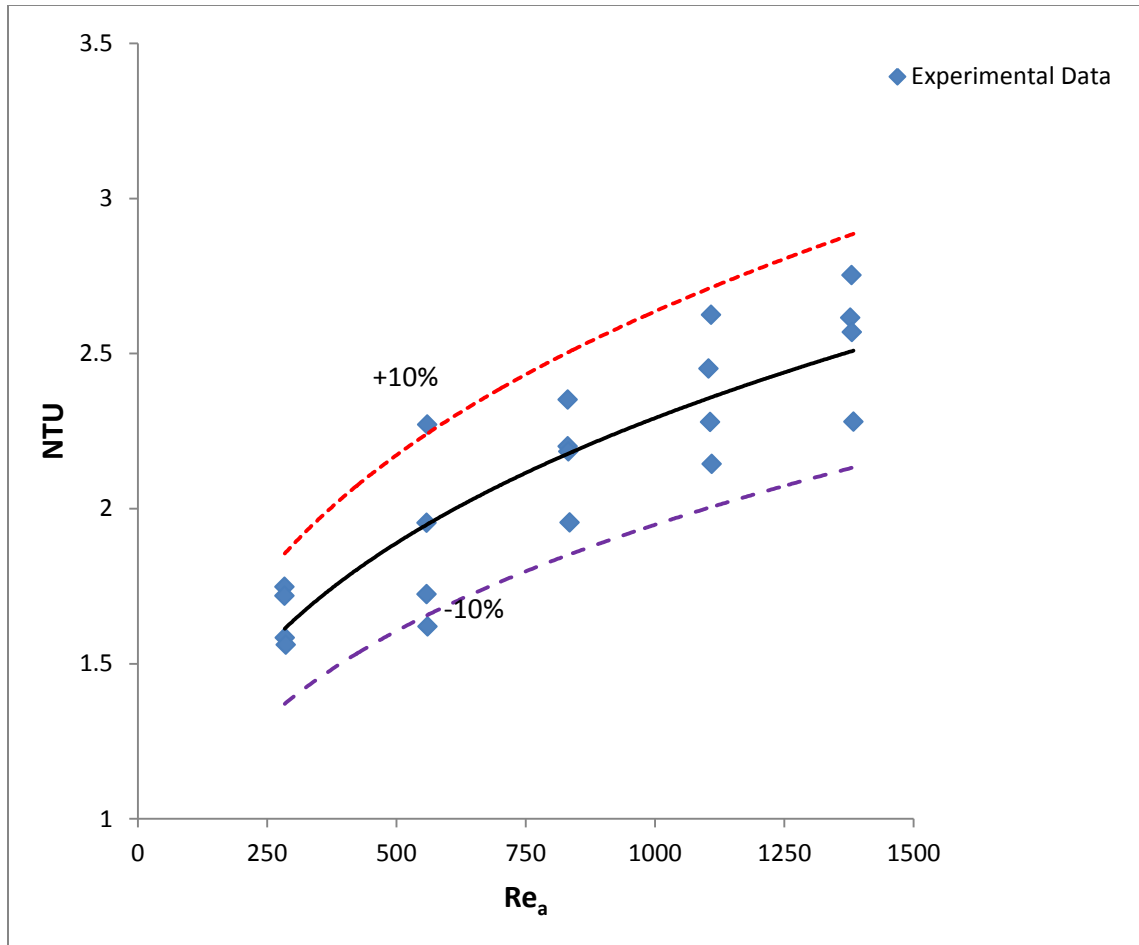


Figure 5.17: Comparison to current NTU- Re_a correlation with experimental data

5.3.4 Effective-NTU relationship

The effectiveness (ϵ) versus NTU is plotted in Fig.5.18 for all operating conditions. The figure indicates that effectiveness increases with increasing NTU almost linearly, and the effectiveness value is higher at lower water-side Reynolds number for particular NTU since the low water mass flow rate having greater effectiveness. The general ϵ -NTU correlation equation is achieved by combining all operating conditions through power law relationship as

$$\epsilon = 0.5091(NTU)^{0.6286} \quad 283 \leq Re_a \leq 1384 \quad (5.15)$$

The Eq.(5.15) can predict all experimental data within $\pm 10\%$, and it is shown in Fig.19.

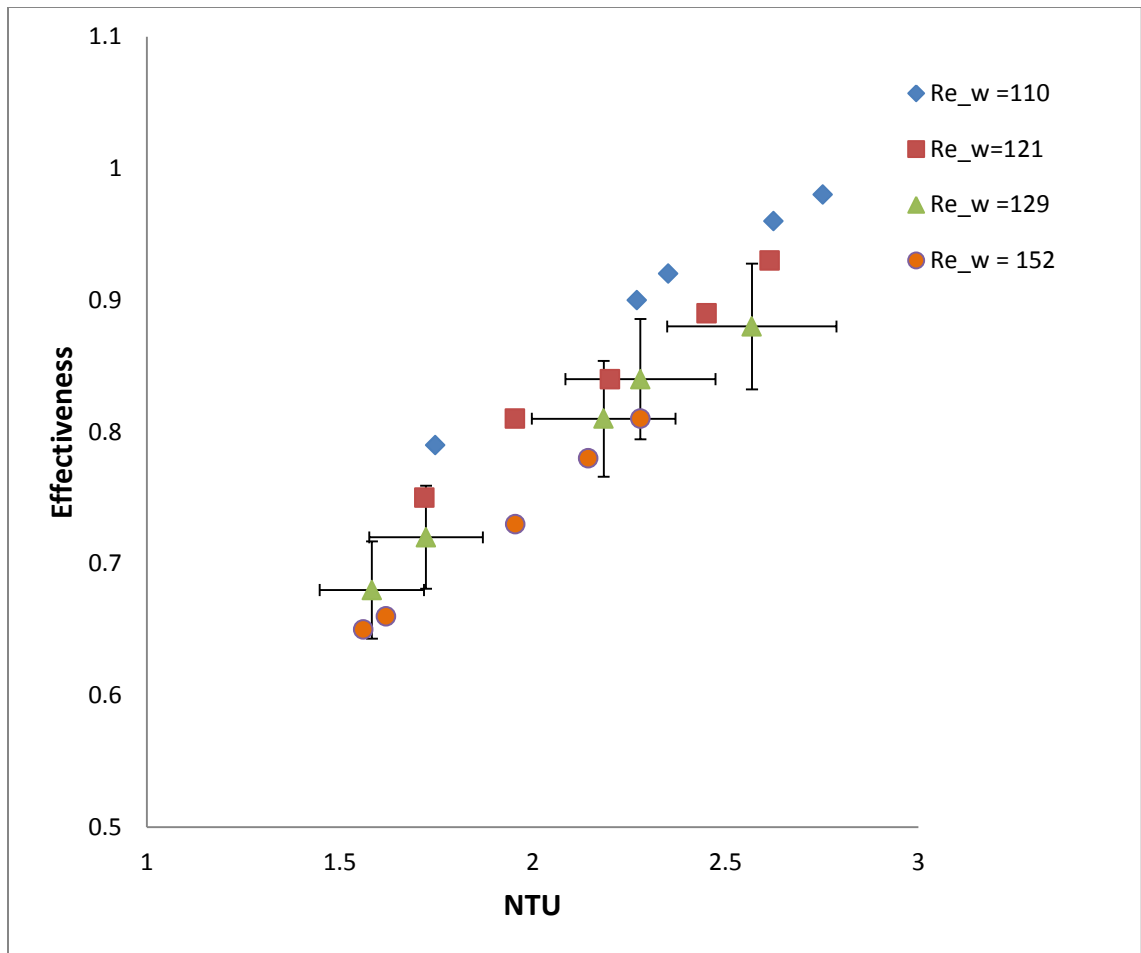


Figure 5.18: The effect NTU on effectiveness (ϵ)

CHAPTER VI

CONCLUSIONS AND RECOMMENDATIONS

An experimental study was performed to characterize air-side heat transfer and fluid flow behaviors via cross-flow microchannel heat exchangers during air cooling. Twenty distinct operating conditions were maintained to obtain the key heat transfer and fluid flow parameters. The deionized water temperature, as the cold side working fluid inlet, was maintained at a constant 9 ± 0.5 °C by a chiller, and the air temperature for the hot side working fluid inlet was kept at a constant 38 ± 5 °C by a built in heat exchanger inside the wind tunnel. The mass flow rates of deionized water were varied in four levels, from 0.0169 kg/s to 0.024 kg/s, and air face velocities were changed in five steps from 1m/s to 5m/s at each deionized mass flow rate. The hydraulic diameter of the microchannel was used to compute the water-side Reynolds number. The air-side Reynolds number was based on the air-side hydraulic diameter, which was obtained for air-side matrix flow passages as proposed by Kays and London (1984). The range of water and air-side Reynolds numbers in the experiment were $110 \leq Re_w \leq 152$ and $283 \leq Re_a \leq 1384$ respectively. The conclusions and recommendations are furnished in the current study on the basis of the experimental data as well as analytical findings.

6.1 Conclusions

The aim of this study was to determine the heat transfer, fluid flow, and key parameters of microchannel heat exchanger performance, such as heat transfer rates, Nusselt numbers, Colburn factors, Reynolds numbers, friction factors, overall thermal resistance, effectiveness, and NTU. The effects of air- and water-side Reynolds numbers on these key parameters were examined and general correlations are proposed. The Nu_a -

Re_a - Pr_a relationship of the present study is compared to correlations available in the open literature.

- The differences between the rate of heat released by the hot air and the rate of heat gained by the cold de-ionised water were less than 4%, which indicates that there was negligible heat loss to the surroundings.
- Air-side Reynolds (Re_a) played a major role in heat transfer, and water-side Reynolds (Re_w) had less influence on heat transfer. The average heat transfer rate (\dot{Q}) increased with the increasing of air-side Reynolds in power law relationship, and the heat transfer rate showed higher as the water-side Reynolds number increased for a certain air-side Reynolds number. The $\dot{Q} - Re_a$ general correlation was obtained in the current study as

$$\dot{Q} = 575.83 Re_a^{0.1855} \quad 283 \leq Re_a \leq 1384 \quad (6.1)$$

- The air-side Nusselt number (Nu_a) intuitively increased as the air-side Reynolds number (Re_a) increased in power law relationship. The air-side Colburn factor (j_a) decreased with increasing Re_a non-linearly with a negative exponent. The effect of water-side Reynolds (Re_w) on Nu_a and j_a was also observed, but not as much as Re_a due to higher air-side thermal resistance. The following heat transfer correlations were obtained by combining all operating conditions, and they can predict $\pm 10\%$ experimental data:

$$Nu_a = 0.5925 Re_a^{0.2743} Pr_a^{\frac{1}{3}} \quad 283 \leq Re_a \leq 1384 \text{ and } 0.70 < Pr_a < 0.72 \quad (6.2)$$

$$j_a = 0.5925 Re_a^{-0.726} \quad 283 \leq Re_a \leq 1384 \quad (6.3)$$

The Nu_a - Re_a - Pr_a correlation of the current study [Eq. (6.3)] is compared with the correlations of Taler (2005) and Tang & Yang (2005), proposed for conventional

compact cross-flow heat exchangers. The Nu_a of the present study is observed as higher in comparison to their Nusselt number value within the range of experimental Reynolds number ($283 \leq Re_a \leq 1384$).

- The air-side pressure drop (ΔP_a) and friction factor (f_a) across the heat exchanger core increased with increasing Re_a , in accordance with power law, but there was little influence of Re_w on ΔP_a and f_a . The f_a - Re_a general correlation was obtained by combining all operating conditions through the power law curve as

$$f_a = 5.6619(Re_a)^{-0.646} \quad 283 \leq Re_a \leq 1384 \quad (6.5)$$

- The air-side Reynolds number (Re_a) governed the overall thermal resistance (R_{Total}). The R_{Total} decreased with increasing Re_a according to power law relationship with a negative exponent. The dominating thermal resistance was observed in the air-side within the range of 89% - 94% of overall thermal resistance. These are quite consistent with other findings for air-side thermal resistance. The R_{Total} - Re_a general correlation is achieved by combining all operating conditions (all data points) through the power law curve as

$$R_{Total} = 0.03 (Re_a)^{-0.254} \quad 283 \leq Re_a \leq 1384 \quad (6.6)$$

- The effectiveness (ϵ) and NTU increased with increasing Re_a non-linearly, and ϵ & NTU were found to be higher at lower Re_w for a certain Re_a , because the \dot{m}_w is the dominating factor for ϵ & NTU. The $\epsilon - Re_a$, $NTU - Re_a$, and $\epsilon - NTU$ correlations are obtained by combining all operating conditions (all data points) through the power law curve.

The downsize flow passages ($D_h \leq 1\text{mm}$) have greater ability to transfer heat with moderate pressure drop, among other reasons, to their high area density. In addition to

the narrow flow passage benefits, the slab serpentine geometry provides a flat heating surface on the top and bottom faces of each slab, which eliminates the wake region formation behind the tube of inline conventional heat exchangers. The flat heating surfaces make good contact with flowing air, and it provides uniform temperature distribution on the air-side of the MCHX core. The serpentine parts of the slabs help to break the thermal boundary layer. All of these features could lead to greater heat transfer.

Several key correlations were achieved on heat transfer and fluid flow for multiport cross-flow microchannel heat exchanger. Air cooling through chilled water is a common method in HVAC fields. Some air face velocities were maintained in the present study, such as practical air face velocities over the cooling coil of the HVAC system. The outcomes of the present study will help to incorporate such MCHX cores in many engineering applications, contributing to savings in energy, space, cost, and materials.

6.2 Recommendations

The findings and observations of the current study can contribute to further research and investigation in the field of heat transfer and fluid flow area, especially with respect to the air-side of cross-flow heat exchangers. Several correlation equations were obtained through the experiment, which may be worthwhile for practical engineering applications in HVAC, automotive, and other areas. The outcomes of the present study can be corroborated and developed by extending the range of operating conditions such as flow regimes and heat transfers. The findings and results can also be improved by

optimizing the geometric design parameters, i.e. shape, orientation, and spacing of channels, fin parameters, etc.

The current study can be advanced in the following ways:

- Experimental investigation of air heating via the current MCHX core and experimental setup.
- Numerical studies using the current MCHX geometries, while maintaining similar operating conditions, and comparing the numerical investigations with experimental findings.
- Investigation of the effect of different fin types, fin arrangements, fin heights, fin thicknesses, and fin densities on air-side heat transfer and flow characteristics, and comparing these findings to the results of the current study.
- Experimental investigation of the current MCHX core and experimental setup by maintaining wide operating conditions such as larger temperature differences between the two fluids, greater mass flow rates of water, more steps of air velocity, etc.
- Comparison to the present results with in-line and staggered tube rows compact heat exchangers with different fin geometries.
- Comparison of the findings of the current study with the air-cooling coil of the HVAC system under similar operating conditions.

Some significant limitations exist in the present experimental setup. Hence, the following recommendations are proposed to improve the current experimental setup for better accuracy in data collection and overall correctness of different heat transfer, fluid flow and other key parameters.

1. Building hot and cold water supplies are used in the experimental setup to maintain air inlet temperature through the wind tunnel's built-in heat exchanger. Supply water cannot be controlled precisely through the gate valves. Besides this, fluctuations of water supply occur frequently because the supply pressure depends on the use of water in the building. Replacement of the existing arrangement by a heater and cooler with water reservoir tank and pump can give more accurate and controlled air inlet temperatures.
2. Replacement of existing chillier by a chillier with a capacity of 6kW or more, as well as a liquid source tank that would increase the stable deionized water inlet temperature and comprehensive operating conditions.
3. Replacement of the current gear pump by a higher capacity gear pump that would increase the mass flow rates. This might facilitate investigations on turbulent flow through the microchannel.

APPENDIX-A

EXPERIMENTAL UNCERTAINTY ANALYSIS

The experimental study encompasses with a lot of measurements in each and every stage such as measurement of geometrical dimensions, a number of fluid flow and heat transfer parameters. Errors may come through these different measurement processes. Dependent parameters involve with independent parameters. Thus errors of independent parameters have an effect on derived parameters. Consequently it influences on the final outcomes of the experimental study. Hence, the estimation of uncertainties is one of the key issues for integrity and authenticity of experimental findings. It is also a general convention that experimental findings cannot be acceptable without estimation of uncertainties. Several researchers accomplished the methodology and procedures to find out experimental uncertainties. Kline and McClintock (1953) illustrated uncertainties in single sample experiments. Moffat (1988) described the uncertainties in experimental results. Coleman and Steel (1995) stated experimental uncertainty analysis for engineering applications.

A.1 Uncertainty analysis methodology

The uncertainties analyses in the present study are based on the mentioned notable works of Moffat (1985), Coleman and Steel (1989, 1995) and Figliola and Beasley (1995) as well as standard procedures on this regard. Mainly two kinds of parameters are involved in the experiment, one is independent parameters and another is dependent parameters. The independent parameters are the basic dimensions of different geometries such as length, width and height of the fluid flow passages, fins etc., measured variables such as temperatures, pressure, velocity, mass and time. The dependent parameters are air-side hydraulic diameter,

mass flow rate, Reynolds number, heat transfer rate, Nusselt number, Colburn factor and so on. The dependent parameters are reliant on independent parameters for their functional relationship.

A.1.1 Uncertainty analysis for independent parameters

The source of errors is broadly divided in three groups: calibration error, data acquisition error and data reduction error. Each group has many sources of elements for errors. The manufacturer of the measured tools/instruments and system provided various information as in the specification list such as accuracy, linearity, drifts, hysteresis, repeatability. The source bias limit (B_i) and source precision index (P_i) are evaluated by using the root sum square (RSS) method as

$$B_i = \pm \sqrt{B_{i1}^2 + B_{i2}^2 \pm \dots + B_{ik}^2} \quad i = 1, 2, 3 \quad (\text{A.1})$$

$$P_i = \pm \sqrt{P_{i1}^2 + P_{i2}^2 + \dots + P_{ik}^2} \quad i = 1, 2, 3 \quad (\text{A.2})$$

Where $i=1,2,3$ refer to the error source groups i.e. calibration error, $i=1$, data-acquisition error, $i=2$ and data - reduction error, $i=3$.

The measurement bias limit (B) and measurement precision index (P) are calculated by using the root sum square (RSS) method as

$$B = \pm \sqrt{B_1^2 + B_2^2 + B_3^2} \quad (\text{A.3})$$

$$P = \pm \sqrt{P_1^2 + P_2^2 + P_3^2} \quad (\text{A.4})$$

The measurement uncertainty combining of bias and precision uncertainty is found through the RSS method as

$$U_x = \pm \sqrt{B^2 + (t_{v,95}P)^2} \quad (95\%) \quad (\text{A.5})$$

Where, $(t_{v, 95P})$ is the precision uncertainty in x at 95% confidence and v is the degree of freedom which is evaluated by using the Welch-Satterthwaite formula as

$$v = \frac{\left(\sum_{i=1}^3 \sum_{j=1}^K P_{ij}^2\right)^2}{\sum_{i=1}^3 \sum_{j=1}^K \left(\frac{P_{ij}^4}{v_{ij}}\right)} \quad (\text{A.6})$$

Where, i = source error groups, j =each element error within each source group with $v_{ij} = N_{ij}-1$.

A.1.2 Uncertainty analysis for dependent parameters

The uncertainties of dependent parameters are quantified by using the evaluated uncertainties of independent parameters as well as their functional relationships with the independent parameters through the RSS method. As for example, dependent parameter, Y which depends on independent parameters $X_1, X_2, X_3, \dots, X_n$ as

$$Y = f(X_1, X_2, X_3, \dots, X_n) \quad (\text{A.7})$$

Therefore, the absolute uncertainty of Y can be evaluated as

$$U_Y = \sqrt{\left(\frac{\partial Y}{\partial X_1} U_{X_1}\right)^2 + \left(\frac{\partial Y}{\partial X_2} U_{X_2}\right)^2 + \left(\frac{\partial Y}{\partial X_3} U_{X_3}\right)^2 + \dots + \left(\frac{\partial Y}{\partial X_n} U_{X_n}\right)^2} \quad (\text{A.8})$$

Where, U_Y = absolute uncertainty of Y , U_X = absolute uncertainty of $X_1 \dots X_n$, the partial derivatives, $\frac{\partial Y}{\partial X_1}, \frac{\partial Y}{\partial X_2}, \frac{\partial Y}{\partial X_3}, \dots$, are computed from the functional relationship as in the Eq. (A.7).

The relative uncertainty is evaluated as

$$\frac{U_Y}{\bar{Y}} = \frac{\sqrt{\left(\frac{\partial Y}{\partial X_1} U_{X_1}\right)^2 + \left(\frac{\partial Y}{\partial X_2} U_{X_2}\right)^2 + \left(\frac{\partial Y}{\partial X_3} U_{X_3}\right)^2 + \dots + \left(\frac{\partial Y}{\partial X_n} U_{X_n}\right)^2}}{f(X_1, X_2, X_3, \dots, X_n)} \quad (\text{A.9})$$

A.2 Uncertainties of key dimensional parameters

The uncertainties for key dimensional parameters are presented in Table A.1.

Table A.1: Uncertainties of key dimensional parameters

SL. No.	Description	Mean Value	Uncertainty (%)
1	HT length in air flow direction (L_a)	0.1m	± 0.1
2	Air-side total frontal area ($A_{fr,a}$)	0.09290m ²	± 0.37
3	Air-side minimum free flow area ($A_{min,a}$)	0.07092m ²	± 0.33
4	Air-side total heat transfer area (A_a)	8.12821m ²	± 0.0026
5	Hydraulic diameter of microchannel ($D_{h,w}$)	0.001m	± 3.48
6	Water-side total heat transfer area (A_w)	0.987m ²	± 3.49

A.2.1 Uncertainty estimation for air-side hydraulic diameter

Air-side hydraulic diameter expression for matrix flow passages is defined by Kays and

London (1984) as,
$$D_{h,a} = f(L_a, A_{min,a}, A_a) = \frac{4L_a A_{min,a}}{A_a} \quad (A.10)$$

$$= \frac{(4)(0.1)(0.07092)}{8.1282} = 0.00349\text{m}$$

Absolute uncertainty of air-side hydraulic diameter,

$$U_{Dh} = \pm \sqrt{\left(\frac{\partial D_h}{\partial L} \cdot u_L\right)^2 + \left(\frac{\partial D_h}{\partial A_{min}} \cdot u_{A_{min}}\right)^2 + \left(\frac{\partial D_h}{\partial A} \cdot u_A\right)^2} \quad (A.11)$$

$$= \pm \sqrt{\left(\frac{A_{min}}{A_a} \cdot u_L\right)^2 + \left(\frac{L}{A} \cdot u_{A_{min}}\right)^2 + \left(-\frac{L A_{min}}{A_a^2} \cdot u_A\right)^2}$$

$$= \pm \sqrt{\left(\frac{0.07092}{8.1282} \times 0.0001\right)^2 + \left(\frac{0.1}{8.1282} \times 0.000236\right)^2 + \left(-\frac{(0.1)(0.07092)}{(8.1282)^2} \times 0.000214\right)^2}$$

$$= \pm 0.000003031\text{m}$$

Relative uncertainty of air-side hydraulic diameter (in percentage) is estimated,

$$\frac{U_{Dh}}{D_h} \times 100 \tag{A.12}$$

$$= \pm \frac{0.000003031}{0.00349} \times 100 = \pm 0.87\%$$

A.3 Uncertainties estimation for one operating conditions

The twenty distinct operating conditions were maintained in the current study. The experimental uncertainties are estimated for all of these twenty operating conditions, and the ranges of uncertainties for all operating conditions are provided in Table-A.3. However, the detail of uncertainty analysis for one operating condition (Air velocity (V_a): 3m/s, $T_{a,i} = 38.1^\circ\text{C}$, $T_{w,i} = 8.57^\circ\text{C}$, deionized water mass flow rate = 0.02kg/s) is presented here. The data acquisition system is capable to take 1000 samples per second i.e. the sampling rate 1 kHz during experimental run. During the steady state condition all samples were taken, and the best 108000 samples for each variable are considered for data reduction and analysis purpose. The mean values of all sample data for the mentioned operating condition are shown in Table A.2.

Table A.2: Mean value of different parameters at one operating condition
(V_a : 3m/s, $T_{a,i} = 38.1^\circ\text{C}$, $T_{w,i} = 8.57^\circ\text{C}$, water mass flow rate : 0.02kg/s)

Parameters	Mean Value
Air inlet temperature ($T_{a,i}$)	38.10°C
Air outlet temperature ($T_{a,o}$)	31.55°C
Deionized water inlet temperature ($T_{w,i}$)	8.57°C
Deionized water outlet temperature ($T_{w,o}$)	33.41°C
Deionized water mass flow rate (\dot{m}_w)	0.02kg/s

Air velocity (V_a)	3m/s
Mass flow rate of air (\dot{m}_a)	0.32kg/s
Air-side pressure drop(ΔP_a)	70.80Pa
Air density (ρ_a)	1.146kg/m ³
Specific heat of air ($c_{p,a}$)	1000.67J/kg.°C
Air-side Reynolds number (Re_a)	832.6
Deionized water-side Reynolds number (Re_w)	130.84
Air-side heat transfer rate (\dot{Q}_a)	2107.04 W
Water-side heat transfer rate(\dot{Q}_w)	2074.43 W
Average heat transfer rate (\dot{Q})	2090.74 W
Air-side Nusselt number (Nu_a)	3.35
Air-side Prandtl number (Pr_a)	0.71
Air-side Colburn factor (j_a)	0.00451

A.3.1.1 Uncertainty estimation for air inlet temperature

Nine thermocouples are positioned at different locations [Fig.3.5] at the air inlet cross-section within the test chamber. Mean temperature and standard deviation for 108000 readings of each thermocouple in a particular run is calculated as

$$\bar{T}_m = \frac{1}{N} \sum_{n=1}^{N=108000} T_{mn} \quad (\text{A.13})$$

$$S_{T_m} = \left[\frac{1}{N-1} \sum_{n=1}^{N=108000} (T_{mn} - \bar{T}_m)^2 \right]^{1/2} \quad (\text{A.14})$$

The mean temperature of air inlet is evaluated by averaging the mean values of the 9 thermocouples as

$$\langle \bar{T} \rangle = \frac{1}{m} \sum_{m=1}^m \bar{T}_m \quad (\text{A.15})$$

Where, $m = 9$ for air inlet

Air inlet mean temperature, $\langle \bar{T}_{a,i} \rangle = 38.10^\circ\text{C}$

Among the 3 error source groups, calibration errors [$i = 1$], data-acquisition errors [$i = 2$], and data-reduction errors [$i = 3$]. Calibration and data-reduction errors are ignored in the current study.

Data-acquisition errors

From Data-Acquisition error source group (As on the Table 5.2, Theory and design for mechanical measurements, 2nded, R.S. Figliola, D.E. Beasley, Wiley, 1995), the instrument error [$j = 2$], spatial variation errors [$j = 8$], and temporal variation errors [$j = 9$] are considered here.

Instrument accuracy and errors are collected from manufacture's catalogues.

Step-1: considering sensor thermocouple stage (instrument error) with $i = 2$ and $j = 2$

Accuracy = $\pm 1^\circ\text{C}$

Resolution = $\pm 0.01^\circ\text{C}$

$$\text{Uncertainty caused by bias, } B_{22} = \pm \sqrt{\left[\frac{1}{2}(0.01)\right]^2 + (1)^2} = \pm 1^\circ\text{C} \quad (95) \%$$

$$P_{22} = 0$$

Step-2: Signal conditioning stage (instrument error) with i = 2 and j = 3

$$\text{Accuracy} = \pm 0.06^\circ\text{C}$$

$$\text{Resolution} = \pm 0.038^\circ\text{C}$$

$$\text{Offset error} = \pm 0.025^\circ\text{C}$$

$$\text{System noise error} = \pm 0.125^\circ\text{C}$$

Uncertainty caused by bias,

$$B_{23} = \pm \sqrt{\left[\frac{1}{2}(0.038)\right]^2 + (0.06)^2 + (0.025)^2 + (0.125)^2} = \pm 0.142^\circ\text{C} \quad (95) \%$$

$$P_{23} = 0$$

Step-3: considering the spatial variation errors with i = 2 and j = 8

The spatial variation errors caused due to the positions of thermocouples in several locations in air intake cross section and non-uniformity in inlet air temperature. The standard deviation of the mean temperatures within the inlet thermocouple grid, S_T is evaluated as

$$S_T = \sqrt{\frac{\sum_{m=1}^9 (\bar{T}_m - \langle \bar{T} \rangle)^2}{m-1}}$$

$$S_T = 0.334^\circ\text{C}$$

Hence, the precision index of the air inlet mean temperature is

$$P_{28} = \frac{S_T}{\sqrt{m}}$$

$$P_{28} = \frac{0.334}{\sqrt{9}} = 0.111^\circ\text{C} \text{ with degrees of freedom, } v_{28} = 9 - 1 = 8$$

Assuming no bias in this element, $B_{28} = 0$

Step-4: Considering temporal variation errors with i = 2 and j = 9

Error caused by the time variations for taking measurements by each thermocouple, and it can be determined by using the pooled standard deviation as

$$S_T = \sqrt{\frac{\sum_{m=1}^9 \sum_{n=1}^{108000} (\bar{T}_{mn} - \bar{T})^2}{M(N-1)}} = \sqrt{\frac{1}{M} \sum_{m=1}^9 (S_{T_m})^2} \quad (\text{A.16})$$

$$S_T = \sqrt{\frac{1}{9} \times 0.02341} = 0.051^\circ\text{C}$$

$$\text{So, precision index, } P_{29} = \frac{S_T}{\sqrt{9 \times 108000}} = \frac{0.051}{\sqrt{972000}} = \frac{0.051}{986} = 0.00005^\circ\text{C}$$

with degrees of freedom, $v_{29} = 9 \times 107999 = 971991$ and $B_{29} = 0$

Step-5

Bias limit,

$$\text{Since } B_1 = B_3 = 0$$

$$B = B_2 = \sqrt{B_{22}^2 + B_{23}^2 + B_{28}^2 + B_{29}^2}$$

$$B = \pm \sqrt{(1)^2 + (0.142)^2 + 0 + 0} = \pm 1.01^\circ\text{C}$$

Precision index,

$$P_2 = \sqrt{P_{22}^2 + P_{23}^2 + P_{28}^2 + P_{29}^2}$$

$$P_2 = \pm \sqrt{0 + 0 + (0.111)^2 + (0.00005)^2} = 0.111^\circ\text{C}$$

$$\text{Since, } P_1 = P_3 = 0$$

$$P = P_2 = \pm 0.111^\circ\text{C}$$

Degrees of freedom, v is evaluated by using the Welch-Satterthwaite equation as

$$v = \frac{(\sum_{i=1}^3 \sum_{j=1}^k P_{ij}^2)^2}{\sum_{i=1}^3 \sum_{j=1}^k \left(\frac{P_{ij}^4}{v_{ij}} \right)}$$

Where i and j represent source error groups and each elemental error respectively.

$$v = \frac{[(0.111)^2 + (0.00005)^2]^2}{\frac{(0.111)^4}{8} + \frac{(0.00005)^4}{971991}} = 8$$

$$U_{T_{a,i}} = \sqrt{B^2 + (t_{8,95}P)^2} \quad (95\%)$$

Absolute uncertainty for air inlet temperature is estimated as

$$U_{T_{a,i}} = \pm \sqrt{(1.01)^2 + (2.306 \times 0.111)^2} = \pm 1.04^\circ\text{C} \quad (95\%)$$

with $t_{8,95} = 2.306$

Relative uncertainty (in percentage) is estimated as

$$\frac{U_{T_{a,i}}}{T_{a,i}} \times 100 = \pm \frac{1.04}{38.10} \times 100 = \pm 2.73\%$$

A.3.1.2 Uncertainty estimation for air outlet temperature

The mean temperature of air outlet is evaluated by averaging the mean values of the 25 thermocouples:

$$\langle \bar{T} \rangle = \frac{1}{m} \sum_{m=1}^m \bar{T}_m \quad (A.17)$$

Where, $m = 25$ for air outlet

Air outlet mean temperature, $\langle \bar{T}_{a,o} \rangle = 31.55^\circ\text{C}$

Data-acquisition errors

Sensor thermocouple stage (instrument error) with $i = 2$ and $j = 2$

Bias limit, $B_{22} = \pm 1^\circ\text{C} \quad (95)\%$

Precision index, $P_{22} = 0$

Signal conditioning stage (instrument error) with $i = 2$ and $j = 3$

Bias limit, $B_{23} = \pm 0.142^\circ\text{C} \quad (95)\%$

Precision index, $P_{23} = 0$

Spatial variation errors with $i = 2$ and $j = 8$

$$S_T = \sqrt{\frac{\sum_{m=1}^{25} (\bar{T}_m - \langle \bar{T} \rangle)^2}{m-1}} = 2.52^\circ\text{C}$$

$$\text{Precision index, } P_{28} = \frac{S_T}{\sqrt{25}} = \frac{2.52^\circ\text{C}}{5} = 0.504^\circ\text{C}$$

with degrees of freedom, $\nu_{28} = 25 - 1 = 24$

Assuming no bias in this element, $B_{28} = 0$

Temporal variation errors with $i = 2$ and $j = 9$

$$S_T = \sqrt{\frac{\sum_{m=1}^{25} \sum_{n=1}^{54000} (T_{mn} - \langle \bar{T} \rangle)^2}{M(N-1)}} = \sqrt{\frac{1}{M} \sum_{m=1}^{25} (S_{T_m})^2} \quad (\text{A.18})$$

$$S_T = \sqrt{\frac{1}{25} \times 0.0739} = 0.054^\circ\text{C}$$

$$\text{So, precision index, } P_{29} = \frac{S_T}{\sqrt{25 \times 108000}} = \frac{0.054}{\sqrt{2700000}} = \frac{0.054}{1643} = 0.000032^\circ\text{C}$$

with degrees of freedom, $\nu_{29} = 25 \times 107999 = 2699975$ and $B_{29} = 0$

Bias limit,

Since $B_1 = B_3 = 0$

$$B = B_2 = \sqrt{B_{22}^2 + B_{23}^2 + B_{28}^2 + B_{29}^2} = \sqrt{(1)^2 + (0.142)^2 + 0} = \pm 1.01^\circ\text{C}$$

Precision index,

$$P_2 = \sqrt{P_{22}^2 + P_{23}^2 + P_{28}^2 + P_{29}^2} = \sqrt{0 + 0 + (0.504)^2 + (0.000032)^2} = 0.504^\circ\text{C}$$

Since, $P_1 = P_3 = 0$

$$P = P_2 = \pm 0.504^\circ\text{C}$$

$$\text{with degrees of freedom, } \nu = \frac{(\sum_{i=1}^3 \sum_{j=1}^K P_{ij}^2)^2}{\sum_{i=1}^3 \sum_{j=1}^k \left(\frac{P_{ij}^4}{\nu_{ij}}\right)} \quad (\text{A.19})$$

$$\therefore \nu = \frac{[(0.504)^2 + (0.000032)^2]^2}{\frac{(0.504)^4}{24} + \frac{(0.000032)^4}{2699999}} = \frac{0.07368}{0.00307} = 24$$

The estimated absolute uncertainty for mean air outlet temperature,

$$U_{T_{a,o}} = \sqrt{B^2 + (t_{26,95}P)^2} \quad (95\%)$$

$$\begin{aligned} \therefore U_{T_{a,o}} &= \pm \sqrt{(1.01)^2 + (2.064 \times 0.504)^2} && \text{with } t_{24,95} = 2.064 \\ &= \pm 1.44^\circ\text{C} \end{aligned}$$

Relative uncertainty (in percentage) is estimated as

$$\frac{U_{T_{a,o}}}{T_{a,o}} \times 100 = \pm \frac{1.44}{31.55} \times 100 = \pm 4.56\%$$

A.3.1.3 Uncertainty estimation for air-side pressure drop

Mean differential pressure, $\overline{\Delta P} = 71.20$ Pa

Data-acquisition errors

Sensor pressure transducer stage (instrument error) with $i = 2$ and $j = 2$

Bias limit:

For Omega pressure transducer -PX277

Accuracy = $\pm 0.1\%$ of full scale

$$e_1 = \pm \frac{0.1}{100} \times 5 \times 249.1 \text{ Pa} = \pm 1.25 \text{ Pa}$$

Thermal effect = $\pm 0.02\%$ FS/ $^\circ\text{C}$

$$e_2 = \pm 3.71 \text{ Pa}$$

$$\text{Bias limit, } B_{22} = \pm\sqrt{e_1^2 + e_2^2} = \pm\sqrt{(1.25)^2 + (3.71)^2} = \pm 3.91 \text{ Pa}$$

$$\text{Precision index, } P_{22} = 0$$

Signal conditioning stage (instrument error) with $i = 2$ and $j = 3$

$$\text{Accuracy} = \pm 0.0003 \text{ Pa}$$

$$\text{Resolution} = \pm 0.0002 \text{ Pa}$$

$$\text{Offset error} = \pm 0.0001 \text{ Pa}$$

$$\text{System noise error} = \pm 0.0011 \text{ Pa}$$

Uncertainty caused by bias,

$$B_{23} = \pm\sqrt{\left[\frac{1}{2}(0.0002)\right]^2 + (0.0003)^2 + (0.0001)^2 + (0.0011)^2} = \pm 0.0008 \text{ Pa} \quad (95) \%$$

$$P_{23} = 0$$

Signal conditioning stage (instrument error) with $i = 2$ and $j = 9$

$$\text{Bias limit, } B_{29} = 0$$

$$\text{No. of data points, } N = 108000$$

$$\text{Degrees of freedom, } \nu = N - 1 = 107999$$

$$\text{Standard deviation, } S_{\Delta P} = 0.30655749$$

$$\therefore \text{Precision index, } P_{29} = \frac{S_{\Delta P}}{\sqrt{N}} = \pm \frac{0.30655749}{\sqrt{108000}} = \pm 0.000937 \text{ Pa}$$

$$\text{Degrees of freedom, } \nu = 107999$$

$$\text{Bias limit, } B = \sqrt{B_{22}^2 + B_{23}^2} = \pm\sqrt{(3.91)^2 + (0.0008)^2} = \pm 3.91 \text{ Pa}$$

$$\text{Precision index, } P = P_{29} = \pm 0.000937 \text{ Pa}$$

Absolute uncertainty is estimated as,

$$\begin{aligned}
 U_{\Delta P} &= \sqrt{B^2 + (t_{v,p} P)^2} && (95\%) \\
 &= \pm \sqrt{(3.91)^2 + [(1.96)(0.00093)]^2} && \text{with } t_{107999,95} = 1.960 \\
 &= \pm 3.91 \text{ Pa}
 \end{aligned}$$

Relative uncertainty is estimated as

$$\frac{U_{\Delta P}}{\Delta P} \times 100 = \pm \frac{3.91}{71.20} \times 100 = \pm 5.49\%$$

A.3.1.4 Uncertainty estimation for air velocity

We found one unique value, 3m/s for frontal air velocity (v) throughout the particular experimental run; therefore only bias errors are involved, and no precision error is considered.

Resolution of the velocity measuring apparatus = 0.01m/s and accuracy = ± 0.05 m/s

Absolute uncertainty

$$U_v = \pm \sqrt{(0.005)^2 + (0.05)^2} = \pm 0.05 \text{ m/s}$$

Relative uncertainty for frontal air velocity (in percentage) is estimated,

$$\frac{U_v}{v} \times 100 = \pm \frac{0.05}{3} \times 100 = \pm 1.66\%$$

A.3.1.5 Uncertainties estimation for thermophysical properties of air

The thermophysical properties ($\rho_a, \mu_a, c_{p,a}$ and k_a) of air are evaluated at the average air inlet and outlet temperature.

$$T_b = \frac{T_{a,i} + T_{a,o}}{2} = \frac{38.1^\circ\text{C} + 31.55^\circ\text{C}}{2} = 34.8^\circ\text{C} \quad (20)$$

The mean value of $\rho_a, \mu_a, c_{p,a}$ and k_a at average air temperature :

$$\rho_a = 1.147 \text{ kg/m}^3$$

$$\mu_a = 1.89066 \times 10^{-5} \text{ kg/m.s}$$

$$c_{p,a} = 1006.67 \text{ J/kg} \cdot ^\circ\text{C}$$

$$k_a = 0.0267 \text{ W/m} \cdot ^\circ\text{C}$$

a) Uncertainty estimation for density (ρ_a)

$$\begin{aligned} U_{\rho,a} &= \pm \frac{\rho_{a,o} - \rho_{a,i}}{T_{a,i} - T_{a,o}} & (\text{A.21}) \\ &= \pm \frac{1.1589 - 1.1345}{38.1 - 31.55} \\ &= \pm 0.0037 \text{ kg/m}^3 \end{aligned}$$

b) Uncertainty estimation for dynamic viscosity (μ_a)

$$\begin{aligned} U_{\mu,a} &= \pm \frac{\mu_{a,i} - \mu_{a,o}}{T_{a,i} - T_{a,o}} & (\text{A.22}) \\ &= \pm \frac{(1.90 - 1.87) 10^{-5}}{38.1 - 31.55} \\ &= \pm 0.0045 \times 10^{-5} \text{ kg/m} \cdot \text{s} \end{aligned}$$

c) Uncertainty estimation for specific heat ($c_{p,a}$)

$$\begin{aligned} U_{c_{p,a}} &= \pm \frac{c_{p_{a,i}} - c_{p_{a,o}}}{T_{a,i} - T_{a,o}} & (\text{A.23}) \\ &= \pm \frac{(1006.82 - 1006.52)}{38.1 - 31.55} \\ &= \pm 0.045 \text{ J/kg} \cdot ^\circ\text{C} \end{aligned}$$

d) Uncertainty estimation for Thermal Conductivity (k_a)

$$\begin{aligned} U_{k,a} &= \pm \frac{k_{a,i} - k_{a,o}}{T_{a,i} - T_{a,o}} & (\text{A.24}) \\ &= \pm \frac{(0.026937022 - 0.026455411)}{38.1 - 31.55} \\ &= \pm 0.000074 \text{ W/m} \cdot ^\circ\text{C} \end{aligned}$$

A.3.1.6 Uncertainty estimation for air mass flow rate

$$\dot{m}_a = f(A_{fr}, v_a, \rho_a) = A_{fr} v_a \rho_a \quad (\text{A.25})$$

$$= (0.0929) (3) (1.147)$$

$$= 0.32 \text{ kg/s}$$

Absolute uncertainty for air-side mass flow rate

$$U_{\dot{m}_a} = \pm \sqrt{\left(\frac{\partial \dot{m}}{\partial A_{fr}} \cdot U_{A_{fr}}\right)^2 + \left(\frac{\partial \dot{m}}{\partial v_a} \cdot U_{v,a}\right)^2 + \left(\frac{\partial \dot{m}}{\partial \rho} \cdot U_{\rho,a}\right)^2} \quad (\text{A.26})$$

$$= \pm \sqrt{(\rho_a \cdot v_a \cdot U_{A_{fr}})^2 + (A_{fr} \rho_a \cdot U_{v,a})^2 + (A_{fr} v_a \cdot U_{\rho,a})^2}$$

$$= \pm \sqrt{[(1.147)(3)(0.000345)]^2 + [(0.0929)(1.147)(0.05)]^2 + [(0.0929)(3)(0.0037)]^2}$$

$$= \pm 0.005 \text{ kg/s}$$

Relative uncertainty (in percentage) is estimated as

$$\frac{U_{\dot{m}_a}}{\dot{m}_a} \times 100 = \pm \frac{0.005}{0.32} \times 100 = \pm 1.73\%$$

A.3.1.7 Uncertainty estimation for air-side Reynolds number

$$\text{Reynolds number, } Re_a = \frac{\rho_a v_a D_{h,a}}{\mu_a} = 833 \quad (\text{A.27})$$

Absolute uncertainty,

$$U_{Re_a} = \pm \sqrt{\left(\frac{\partial Re_a}{\partial \rho_a} U_{\rho_a}\right)^2 + \left(\frac{\partial Re_a}{\partial v_a} U_{v,a}\right)^2 + \left(\frac{\partial Re_a}{\partial D_{h,a}} U_{D_{h,a}}\right)^2 + \left(\frac{\partial Re_a}{\partial \mu_a} U_{\mu_a}\right)^2} \quad (\text{A.28})$$

$$\text{Where } \frac{\partial Re_a}{\partial \rho} = \frac{v_a D_{h,a}}{\mu_a} = \frac{(3)(0.00349)}{1.89 \times 10^{-5}} = 554$$

$$\frac{\partial Re_a}{\partial v_a} = \frac{\rho_a D_{h,a}}{\mu_a} = \frac{(1.147)(0.00349)}{1.89 \times 10^{-5}} = 211.8$$

$$\frac{\partial Re_a}{\partial D_{h,a}} = \frac{\rho_a v_a}{\mu_a} = \frac{(1.147)(3)}{1.89 \times 10^{-5}} = 1.82 \times 10^5$$

$$\frac{\partial Re_a}{\partial \mu_a} = -\frac{\rho_a v_a D_{h,a}}{\mu_a^2} = -\frac{(1.147)(3)(0.00349)}{(1.89 \times 10^{-5})^2} = -336.19 \times 10^5$$

$$U_{\rho_a} = 0.0037 \frac{\text{m}}{\text{s}}, U_{v_a} = 0.05 \frac{\text{m}}{\text{s}}, U_{D_{h,a}} = 0.3 \times 10^{-5} \text{ m}, \text{ and } U_{\mu_a} = 0.0045 \times 10^{-5} \text{ m}$$

$$\begin{aligned} \therefore U_{\text{Re}} &= \pm \sqrt{(554 \times 0.0037)^2 + (211.8 \times 0.05)^2 + (1.82 \times 10^5 \times 0.3 \times 10^{-5})^2} \\ &\quad + (-336.19 \times 10^5 \times 0.0045 \times 10^{-5})^2 \\ &= \pm 26 \end{aligned}$$

Relative uncertainty for air-side Reynolds number (in percentage) is estimated as

$$\frac{U_{\text{Re}_a}}{\text{Re}_a} \times 100 = \pm \frac{26}{833} \times 100 = \pm 3.12\%$$

A.3.1.8 Uncertainty estimation for air-side heat transfer rate

$$\text{Air-side heat transfer rate, } \dot{Q}_a = \dot{m}_a c_{p,a} \Delta T_a = 2107 \text{ W} \quad (\text{A.29})$$

Absolute uncertainty for air-side heat transfer rate is estimated as

$$U_{\dot{Q}_a} = \pm \sqrt{\left(\frac{\partial \dot{Q}_a}{\partial \dot{m}_a} U_{\dot{m}_a}\right)^2 + \left(\frac{\partial \dot{Q}_a}{\partial c_{p,a}} U_{c_{p,a}}\right)^2 + \left(\frac{\partial \dot{Q}_a}{\partial \Delta T_a} U_{\Delta T_a}\right)^2} \quad (\text{A.30})$$

$$\text{Where } \frac{\partial \dot{Q}_a}{\partial \dot{m}_a} = c_{p,a} \Delta T_a = 1006.67 \times 6.55 = 6593.69$$

$$\frac{\partial \dot{Q}_a}{\partial c_{p,a}} = \dot{m}_a \Delta T_a = 0.32 \times 6.55 = 2.1$$

$$\frac{\partial \dot{Q}_a}{\partial \Delta T_a} = \dot{m}_a c_{p,a} = 0.32 \times 1006.67 = 322.13$$

$$U_{\dot{m}_a} = 0.005 \frac{\text{kg}}{\text{s}}, U_{c_{p,a}} = 0.045 \frac{\text{J}}{\text{kg}} \text{ } ^\circ\text{C}, \text{ and } U_{\Delta T_a} = 0.44^\circ\text{C}$$

$$\begin{aligned} \therefore U_{\dot{Q}_a} &= \pm \sqrt{(6593.69 \times 0.005)^2 + (2.1 \times 0.045)^2 + (322.13 \times 0.44)^2} \\ &= \pm 145.5 \text{ W} \end{aligned}$$

Relative uncertainty for air-side heat transfer rate (in percentage) is estimated as

$$\frac{U_{\dot{Q}_a}}{\dot{Q}_a} \times 100 = \pm \frac{145.5}{2107} \times 100 = \pm 6.9\%$$

A.3.1.9 Uncertainty estimation for air-side Prandtl number

$$\text{Prandtl number, } Pr_a = \frac{\mu_a c_{p,a}}{k_a} \quad (\text{A.31})$$

$$U_{Pr_a} = \pm \sqrt{\left(\frac{\partial Pr_a}{\partial \mu_a} U_{\mu_a}\right)^2 + \left(\frac{\partial Pr_a}{\partial c_{p,a}} U_{c_{p,a}}\right)^2 + \left(\frac{\partial Pr_a}{\partial k_a} U_{k_a}\right)^2} \quad (\text{A.32})$$

Where,

$$\frac{\partial Pr_a}{\partial \mu_a} = \frac{c_{p,a}}{k_a} = 37707$$

$$\frac{\partial Pr_a}{\partial c_{p,a}} = \frac{\mu_a}{k_a} = 70.8 \times 10^{-5}$$

$$\frac{\partial Pr_a}{\partial k_a} = -\frac{\mu_a c_{p,a}}{(k_a)^2} = -26.69$$

$$U_{\mu_a} = \pm 0.0045 \times 10^{-5} \text{ kg/m.s}$$

$$U_{c_{p,a}} = \pm 0.045 \frac{\text{J}}{\text{kg}} \text{ } ^\circ\text{C}$$

$$U_{k_a} = \pm 7.4 \times 10^{-5} \text{ W/m. } ^\circ\text{C}$$

$$U_{Pr_a}$$

$$= \pm \sqrt{(37707 \times 0.0045 \times 10^{-5})^2 + (70.8 \times 10^{-5} \times 0.045)^2 + (-26.69 \times 7.4 \times 10^{-5})^2}$$

$$= \pm 0.02$$

Relative uncertainty for air-side heat Prandtl number (in percentage) is estimated as

$$\frac{U_{Pr_a}}{Pr_a} \times 100 = \pm \frac{0.02}{0.713} \times 100 = \pm 2.8\%$$

A.3.2.1 Uncertainty estimation for water inlet temperature

Mean deionized water inlet temperature, $T_{w,i} = 8.57^\circ\text{C}$

Data-acquisition errors

Sensor RTD stage (instrument error) with $i = 2$ and $j = 2$

Bias limit:

For Omega Resistance Temperature Detector –Pt100

Accuracy = $\pm 0.012^\circ\text{C}$

Bias limit, B_{22} = $\pm 0.012^\circ\text{C}$

Precision index, P_{22} = 0

Signal conditioning stage (instrument error) with $i = 2$ and $j = 3$

Accuracy = $\pm 0.06^\circ\text{C}$

Resolution = $\pm 0.038^\circ\text{C}$

Offset error = $\pm 0.025^\circ\text{C}$

System noise error = $\pm 0.125^\circ\text{C}$

Uncertainty caused by bias,

$$B_{23} = \pm \sqrt{\left[\frac{1}{2}(0.038)\right]^2 + (0.06)^2 + (0.025)^2 + (0.125)^2} = \pm 0.142^\circ\text{C} \quad (95) \%$$

$P_{23} = 0$

Signal conditioning stage (instrument error) with $i = 2$ and $j = 9$

Bias limit, $B_{29}=0$

No. of data points, $N = 108000$

Degrees of freedom, $\nu = N - 1 = 107999$

Standard deviation, $S_{T_w,i} = 0.027625463^\circ\text{C}$

$$\therefore \text{Precision index, } P_{29} = \frac{S_{T_w,i}}{\sqrt{N}} = \pm \frac{0.027625463}{\sqrt{108000}} = \pm 0.00008^\circ\text{C}$$

Degrees of freedom, $\nu = 107999$

$$\text{Bias limit, } B = \sqrt{B_{22}^2 + B_{23}^2} = \pm\sqrt{(0.142)^2 + (0.012)^2} = \pm 0.142^\circ\text{C}$$

$$\text{Precision index, } P = P_{29} = \pm 0.00008^\circ\text{C}$$

Absolute uncertainty is estimated as,

$$U_{T_{w,i}} = \pm\sqrt{B^2 + (t_{v,p} P)^2} \quad (95\%)$$

$$= \pm\sqrt{(0.142)^2 + [(1.96)(0.00008)]^2} \quad \text{with } t_{107999,95} = 1.960$$

$$= \pm 0.142^\circ\text{C}$$

Relative uncertainty is estimated as

$$\frac{U_{T_{w,i}}}{T_{w,i}} \times 100 = \pm \frac{0.142}{8.57} \times 100 = \pm 1.66\%$$

A.3.2.2 Uncertainty estimation for water outlet temperature

Mean deionized water outlet temperature, $T_{w,o} = 33.41^\circ\text{C}$

Data-acquisition errors

Sensor RTD stage (instrument error) with $i = 2$ and $j = 2$

Bias limit:

For Omega Resistance Temperature Detector –Pt100

$$\text{Accuracy} = \pm 0.012^\circ\text{C}$$

$$\text{Bias limit, } B_{22} = \pm 0.012^\circ\text{C}$$

$$\text{Precision index, } P_{22} = 0$$

Signal conditioning stage (instrument error) with $i = 2$ and $j = 3$

$$\text{Accuracy} = \pm 0.06^\circ\text{C}$$

$$\text{Resolution} = \pm 0.038^\circ\text{C}$$

$$\text{Offset error} = \pm 0.025^\circ\text{C}$$

System noise error = $\pm 0.125^{\circ}\text{C}$

Uncertainty caused by bias,

$$B_{23} = \pm \sqrt{\left[\frac{1}{2}(0.038)\right]^2 + (0.06)^2 + (0.025)^2 + (0.125)^2} = \pm 0.142^{\circ}\text{C} \quad (95) \%$$

$$P_{23} = 0$$

Signal conditioning stage (instrument error) with $i = 2$ and $j = 9$

Bias limit, $B_{29}=0$

No. of data points, $N = 108000$

Degrees of freedom, $\nu = N - 1 = 107999$

Standard deviation, $S_{T_{w,o}} = 0.027625463^{\circ}\text{C}$

$$\therefore \text{Precision index, } P_{29} = \frac{S_{T_{w,o}}}{\sqrt{N}} = \pm \frac{0.049949931}{\sqrt{108000}} = \pm 0.0002^{\circ}\text{C}$$

Degrees of freedom, $\nu = 107999$

$$\text{Bias limit, } B = \sqrt{B_{22}^2 + B_{23}^2} = \pm \sqrt{(0.012)^2 + (0.142)^2} = \pm 0.1425^{\circ}\text{C}$$

Precision index, $P = P_{29} = \pm 0.0002^{\circ}\text{C}$

Absolute uncertainty is estimated as,

$$\begin{aligned} U_{T_{w,o}} &= \sqrt{B^2 + (t_{\nu,p} P)^2} \quad (95\%) \\ &= \pm \sqrt{(0.1425)^2 + [(1.96)(0.0002)]^2} \quad \text{with } t_{107999,95} = 1.960 \\ &= \pm 0.143^{\circ}\text{C} \end{aligned}$$

Relative uncertainty for outlet temperature ($T_{w,o}$) is estimated as

$$\frac{U_{T_{w,o}}}{T_{w,o}} \times 100 = \pm \frac{0.142}{33.71} \times 100 = \pm 0.42\%$$

A.3.2.3 Uncertainty estimation for thermophysical properties of water

The thermophysical properties ($\mu_w, \rho_w, c_{p,w}$ and k_w) of deionized water are evaluated at the average inlet and outlet temperatures for the particular operating condition.

$$T_{b,w} = \frac{T_{w,i} + T_{w,o}}{2} = \frac{8.57 + 33.41}{2} = 20.99^\circ\text{C} \quad (\text{A.33})$$

The mean value of $\rho_w, \mu_w, c_{p,w}$ and k_w at average air temperature :

$$\rho_w = 997.56 \text{ kg/m}^3$$

$$\mu_w = 0.000954056 \text{ kg/m.s}$$

$$c_{p,w} = 4175.58 \text{ J/kg.}^\circ\text{C}$$

$$k_w = 0.606 \text{ W/m.}^\circ\text{C}$$

a) Uncertainty estimation for density (ρ_w)

$$U_{\rho,w} = \pm \frac{\rho_{w,i} - \rho_{w,o}}{T_{w,i} - T_{w,o}} \quad (\text{A.34})$$

$$= \pm \frac{999.75 - 994.12}{8.57 - 33.41}$$

$$= \pm 0.22 \text{ kg/m}^3$$

b) Uncertainty estimation for dynamic viscosity (μ_w)

$$U_{\mu,w} = \pm \frac{\mu_{w,i} - \mu_{w,o}}{T_{w,i} - T_{w,o}} \quad (\text{A.35})$$

$$= \pm \frac{1.3177 \times 10^{-3} - 7.236 \times 10^{-4}}{8.57 - 33.41}$$

$$= \pm 2.39 \times 10^{-5} \text{ kg/m.s}$$

c) Uncertainty estimation for specific heat ($c_{p,w}$)

$$U_{c_{p,w}} = \pm \frac{c_{p,w,i} - c_{p,w,o}}{T_{w,i} - T_{w,o}} \quad (\text{A.36})$$

$$= \pm \frac{(4192.56 - 4168.94)}{(8.57 - 33.41)}$$

$$= \pm 0.95 \text{ J/kg.}^\circ\text{C}$$

d) Uncertainty Estimation for Thermal Conductivity (k_w)

$$\begin{aligned} U_{k,w} &= \pm \frac{k_{w,i} - k_{w,o}}{T_{w,i} - T_{w,o}} \\ &= \pm \frac{(0.5859 - 0.62404)}{8.57 - 33.41} \\ &= \pm 0.00153 \text{ W/m. } ^\circ\text{C} \end{aligned} \quad (\text{A.37})$$

A.3.2.4 Uncertainty estimation for water mass flow rate

The deionized water-side mass flow rate, $\dot{m}_w = \frac{m_w}{t} = 0.02 \text{ kg/s}$

(A.38)

Therefore, the absolute uncertainty of deionized water mass flow rate is evaluated as,

$$U_{\dot{m}_w} = \pm \sqrt{\left(\frac{\partial \dot{m}_w}{\partial m_w} U_{m_w}\right)^2 + \left(\frac{\partial \dot{m}_w}{\partial t} U_t\right)^2} \quad (\text{A.39})$$

Where,

$$\frac{\partial \dot{m}_w}{\partial m_w} = \frac{1}{t}, \quad \frac{\partial \dot{m}_w}{\partial t} = -\frac{m_w}{t^2}, \quad m_w = 3.9 \text{ kg}, \quad t = 195 \text{ s}$$

$$U_{m_w} = \pm 0.09483 \text{ kg}, \quad U_t = \pm 0.0518 \text{ s}$$

$$\begin{aligned} U_{\dot{m}_w} &= \pm \sqrt{\left(\frac{1}{195} \times 0.09483\right)^2 + \left(-\frac{3.9}{195} \times 0.051\right)^2} \\ &= \pm 0.0006 \text{ kg/s} \end{aligned}$$

Relative uncertainty for water-side mass flow rate (in percentage) is estimated as

$$\frac{U_{\dot{m}_w}}{\dot{m}_w} \times 100 = \pm \frac{0.0006}{0.02} \times 100 = \pm 3\%$$

A.3.2.5 Uncertainty estimation for water-side heat transfer rate

$$\text{De-ionized water-side heat transfer rate, } \dot{Q}_w = \dot{m}_w c_{p_w} \Delta T_w = 2074.43 \text{ W} \quad (\text{A.40})$$

Absolute uncertainty for de-ionized water-side heat transfer rate is estimated as

$$U_{\dot{Q}_w} = \pm \sqrt{\left(\frac{\partial \dot{Q}_w}{\partial \dot{m}_w} U_{\dot{m}_w}\right)^2 + \left(\frac{\partial \dot{Q}_w}{\partial c_{p,w}} U_{c_{p,w}}\right)^2 + \left(\frac{\partial \dot{Q}_w}{\partial \Delta T_w} U_{\Delta T_w}\right)^2} \quad (\text{A.41})$$

Where $\frac{\partial \dot{Q}_w}{\partial \dot{m}_w} = c_{p,w} \Delta T_w = 4175.58 \times 24.84 = 103721.4$

$$\frac{\partial \dot{Q}_w}{\partial c_{p,w}} = \dot{m}_w \Delta T_w = 0.02 \times 24.84 = 0.4968$$

$$\frac{\partial \dot{Q}_w}{\partial \Delta T_w} = \dot{m}_w c_{p,w} = 0.02 \times 4175.58 = 83.51$$

$$U_{\dot{m}_w} = \pm 0.0011 \frac{\text{kg}}{\text{s}}, \quad U_{c_{p,w}} = \pm 0.95 \frac{\text{J}}{\text{kg}} \text{ } ^\circ\text{C}, \quad \text{and} \quad U_{\Delta T_w} = \pm 0.20 \text{ } ^\circ\text{C}$$

$$\begin{aligned} \therefore U_{\dot{Q}_w} &= \pm \sqrt{(103721.4 \times 0.0011)^2 + (0.4968 \times 0.95)^2 + (83.51 \times 0.20)^2} \\ &= \pm 115.31 \text{ W} \end{aligned}$$

Relative uncertainty for water-side heat transfer rate (in percentage) is estimated as

$$\frac{U_{\dot{Q}_w}}{\dot{Q}_w} \times 100 = \pm \frac{115.31}{2074.43} \times 100 = \pm 5.56\%$$

A.3.2.6 Uncertainty estimation for water-side Reynolds number

The deionized water-side Reynolds number (Re_w) is expressed as

$$Re_w = \frac{\dot{m}_w}{51\pi\mu_w D_{h,MC}} \quad (\text{A.42})$$

The absolute uncertainty is estimated for Re_w as

$$U_{Re_w} = \pm \sqrt{\left(\frac{\partial Re_w}{\partial \dot{m}_w} U_{\dot{m}_w}\right)^2 + \left(\frac{\partial Re_w}{\partial \mu_w} U_{\mu_w}\right)^2 + \left(\frac{\partial Re_w}{\partial D_{h,MC}} U_{D_{h,MC}}\right)^2} \quad (\text{A.43})$$

Where, $\frac{\partial Re_w}{\partial \dot{m}_w} = \frac{1}{51\pi\mu_w D_{h,MC}} = 6542.31$

$$\frac{\partial Re_w}{\partial \mu_w} = -\frac{\dot{m}_w}{51\pi(\mu_w)^2 D_{h,MC}} = 137155.5$$

$$\frac{\partial Re_w}{\partial D_{h,MC}} = -\frac{\dot{m}_w}{51\pi\mu_w (D_{h,MC})^2} = 130846$$

$$U_{Re_w} = \pm \sqrt{(6542.31 \times 0.0006)^2 + (137155.5 \times 2.39 \times 10^{-5})^2 + (130846 \times 0.0000348)^2}$$

$$= 6.85$$

The relative uncertainty for deionized water-side Reynolds number (in percentage) is estimated as

$$\frac{U_{Re_w}}{Re_w} \times 100 = \pm \frac{6.85}{130} \times 100 = \pm 5.26\%$$

A.3.2.7 Uncertainty estimation for water-side Prandtl number

$$\text{Prandtl number, } Pr_w = \frac{\mu_w c_{p,w}}{k_w} = 6.57 \quad (\text{A.43})$$

$$U_{Pr_w} = \pm \sqrt{\left(\frac{\partial Pr_w}{\partial \mu_w} U_{\mu_w}\right)^2 + \left(\frac{\partial Pr_w}{\partial c_{p,w}} U_{c_{p,w}}\right)^2 + \left(\frac{\partial Pr_w}{\partial k_w} U_{k_w}\right)^2} \quad (\text{A.44})$$

Where,

$$\frac{\partial Pr_w}{\partial \mu_w} = \frac{c_{p,w}}{k_w} = 6890.4$$

$$\frac{\partial Pr_w}{\partial c_{p,w}} = \frac{\mu_w}{k_w} = 1.574 \times 10^{-3}$$

$$\frac{\partial Pr_w}{\partial k_w} = -\frac{\mu_w c_{p,w}}{(k_w)^2} = -10.85$$

$$U_{\mu_w} = \pm 2.39 \times 10^{-5} \text{ kg/m.s}$$

$$U_{c_{p,w}} = \pm 0.95 \frac{\text{J}}{\text{kg}} \text{ } ^\circ\text{C}$$

$$U_{k_w} = \pm 0.00153 \text{ W/m. } ^\circ\text{C}$$

$$U_{Pr_w} = \pm \sqrt{(6890.4 \times 2.39 \times 10^{-5})^2 + (1.574 \times 10^{-3} \times 0.95)^2 + (-10.85 \times 0.00153)^2}$$

$$= \pm 0.17$$

Relative uncertainty for deionized water-side Prandtl number (in percentage) is estimated as

$$\frac{U_{Pr_w}}{Pr_w} \times 100 = \pm \frac{0.17}{6.57} \times 100 = \pm 2.6\%$$

A.3.2.8 Uncertainty estimation for deionised water-side Peclet number

The Peclet number is defined as

$$Pe_w = (Re_w)(Pr_w) \quad (A.45)$$

The absolute uncertainty is estimated for Pe_w as

$$U_{Pe_w} = \pm \sqrt{\left(\frac{\partial Pe_w}{\partial Re_w} U_{Re_w}\right)^2 + \left(\frac{\partial Pe_w}{\partial Pr_w} U_{Pr_w}\right)^2} \quad (A.46)$$

$$\frac{\partial Pe_w}{\partial Re_w} = Pr_w = 6.57$$

$$\frac{\partial Pe_w}{\partial Pr_w} = Re_w = 145.67$$

$$U_{Pe_w} = \pm \sqrt{(6.57 \times 9.12)^2 + (145.67 \times 0.17)^2}$$

$$= \pm 64$$

The relative uncertainty for deionized water-side Reynolds number (in percentage) is estimated as

$$\frac{U_{Pe_w}}{Pe_w} \times 100 = \pm \frac{64}{957} \times 100 = \pm 6.69\%$$

A.3.2.9 Uncertainty estimation for water-side Nusselt number

The following Gnielinski correlation is used to evaluate the deionized water-side Nusselt number

(Nu_w):

$$Nu_w = \left[3.66^3 + 1.61^3 \left(\frac{Pe_w D_{MC}}{L_{MC}}\right)\right]^{\frac{1}{3}} \quad (A.47)$$

The absolute uncertainty is estimated for Nu_w as

$$U_{Nu_w} = \pm \sqrt{\left(\frac{\partial Nu_w}{\partial Pe_w} U_{Pe_w}\right)^2 + \left(\frac{\partial Nu_w}{\partial D_{MC}} U_{D_{MC}}\right)^2 + \left(\frac{\partial Nu_w}{\partial L_{MC}} U_{L_{MC}}\right)^2} \quad (A.48)$$

$$\frac{\partial Nu_w}{\partial Pe_w} = \frac{1.61^3}{3} \left[3.66^3 + 1.61^3 \left(\frac{Pe_w D_{MC}}{L_{MC}}\right)\right]^{-\frac{2}{3}} \left(\frac{D_{MC}}{L_{MC}}\right) = 5.64 \times 10^{-5}$$

$$\frac{\partial Nu_w}{\partial D_{MC}} = \frac{1.61^3}{3} \left[3.66^3 + 1.61^3 \left(\frac{Pe_w D_{MC}}{L_{MC}} \right) \right]^{-\frac{2}{3}} \left(\frac{Pe_w}{L_{MC}} \right) = 41.2$$

$$\frac{\partial Nu_w}{\partial L_{MC}} = -\frac{1.61^3}{3} \left[3.66^3 + 1.61^3 \left(\frac{Pe_w D_{MC}}{L_{MC}} \right) \right]^{-\frac{2}{3}} \left(\frac{Pe_w D_{MC}}{L_{MC}^2} \right) = -0.14$$

Therefore,

$$U_{Nu_w} = \pm \sqrt{(5.64 \times 10^{-5} \times 64)^2 + (41.2 \times 0.008)^2 + (-0.14 \times 0.0000348)^2}$$

$$= \pm 0.31$$

The relative uncertainty for deionized water-side Nusselt number (in percentage) is estimated as

$$\frac{U_{Nu_w}}{Nu_w} \times 100 = \pm \frac{0.31}{3.66} \times 100 = \pm 8.46\%$$

A.3.2.10 Uncertainty estimation for water-side heat transfer coefficient

The de-ionized water-side heat transfer coefficient (h_w) is the function of water-side Nusselt number (Nu_w), thermal conductivity (k_w) and hydraulic diameter ($D_{h,MC}$) as

$$h_w = \frac{Nu_w k_w}{D_{h,MC}} \quad (A.49)$$

The absolute uncertainty is estimated for h_w as

$$U_{h_w} = \pm \sqrt{\left(\frac{\partial h_w}{\partial Nu_w} U_{Nu_w} \right)^2 + \left(\frac{\partial h_w}{\partial k_w} U_{k_w} \right)^2 + \left(\frac{\partial h_w}{\partial D_{h,MC}} U_{D_{h,MC}} \right)^2} \quad (A.50)$$

$$\frac{\partial h_w}{\partial Nu_w} = \frac{k_w}{D_{h,MC}} = 606$$

$$\frac{\partial h_w}{\partial k_w} = \frac{Nu_w}{D_{h,MC}} = 3660.88$$

$$\frac{\partial h_w}{\partial D_{h,MC}} = -\frac{Nu_w k_w}{(D_{h,MC})^2} = -2.21 \times 10^6$$

$$U_{h_w} = \pm \sqrt{(606 \times 0.31)^2 + (3660.88 \times 0.00153)^2 + (-2.21 \times 10^6 \times 0.0000348)^2}$$

$$= \pm 178 \text{ W/m}^2 \cdot \text{°C}$$

The relative uncertainty for deionized water-side heat transfer coefficient (in percentage) is estimated as

$$\frac{U_{h_w}}{h_w} \times 100 = \pm \frac{178}{2219.5} \times 100 = \pm 8.01\%$$

A.3.2.11 Uncertainty estimation for deionised water-side thermal resistance

The liquid side thermal resistance can be expressed as

$$R_w = \frac{1}{h_w A_w} \quad (\text{A.51})$$

Therefore the absolute uncertainty for liquid side thermal resistance is estimated as

$$U_{R_w} = \pm \sqrt{\left(\frac{\partial R_w}{\partial h_w} U_{h_w}\right)^2 + \left(\frac{\partial R_w}{\partial A_w} U_{A_w}\right)^2} \quad (\text{A.52})$$

$$\frac{\partial R_w}{\partial h_w} = -\frac{1}{h_w^2 A_w} = 2.08 \times 10^{-7}$$

$$\frac{\partial R_w}{\partial A_w} = -\frac{1}{A_w^2 h_w} = 0.00047$$

$$\begin{aligned} U_{R_w} &= \pm \sqrt{(2.08 \times 10^{-7} \times 208)^2 + (0.00047 \times 0.034)^2} \\ &= \pm 0.000046^\circ\text{C/W} \end{aligned}$$

The relative uncertainty for overall thermal resistance (in percentage) is estimated as

$$\frac{U_{R_w}}{R_w} \times 100 = \pm \frac{0.000046}{0.000462268} \times 100 = \pm 9.97\%$$

A.3.3.1 Uncertainty estimation for LMTD

The log mean temperature difference (LMTD) is the function of two temperature differentials,

ΔT_1 and ΔT_2 as

$$\Delta T_1 = T_{a,o} - T_{w,i}$$

$$\Delta T_2 = T_{a,i} - T_{w,o}$$

The uncertainty for ΔT_1 is estimated as

$$U_{\Delta T_1} = \pm \sqrt{\left(\frac{\partial \Delta T_1}{\partial T_{a,o}} U_{T_{a,o}}\right)^2 + \left(\frac{\partial \Delta T_2}{\partial T_{w,i}} U_{T_{w,i}}\right)^2} \quad (\text{A.53})$$

Where, $\frac{\partial \Delta T_1}{\partial T_{a,o}} = 1$

$$\frac{\partial \Delta T_2}{\partial T_{w,i}} = 1$$

$$U_{T_{a,o}} = 1.44^\circ\text{C} \quad U_{T_{w,i}} = 0.142^\circ\text{C}$$

$$U_{\Delta T_1} = \pm \sqrt{(1 \times 1.44)^2 + (1 \times 0.142)^2}$$

$$= \pm 1.45^\circ\text{C}$$

The uncertainty for ΔT_2 is estimated as

$$U_{\Delta T_2} = \pm \sqrt{\left(\frac{\partial \Delta T_2}{\partial T_{a,i}} U_{T_{a,i}}\right)^2 + \left(\frac{\partial \Delta T_2}{\partial T_{w,o}} U_{T_{w,o}}\right)^2} \quad (\text{A.54})$$

Where, $\frac{\partial \Delta T_1}{\partial T_{a,i}} = 1$

$$\frac{\partial \Delta T_2}{\partial T_{w,o}} = 1$$

$$U_{T_{a,i}} = 1.04^\circ\text{C} \quad U_{T_{w,o}} = 0.143^\circ\text{C}$$

$$U_{\Delta T_2} = \pm \sqrt{(1 \times 1.04)^2 + (1 \times 0.143)^2}$$

$$= \pm 1.05^\circ\text{C}$$

$$\Delta T_{LM} = \frac{\Delta T_1 - \Delta T_2}{\ln \frac{\Delta T_1}{\Delta T_2}}$$

$$U_{\Delta T_{LM}} = \pm \sqrt{\left(\frac{\partial \Delta T_{LM}}{\partial \Delta T_1} U_{\Delta T_1}\right)^2 + \left(\frac{\partial \Delta T_{LM}}{\partial \Delta T_2} U_{\Delta T_2}\right)^2} \quad (\text{A.55})$$

Here,

$$\frac{\partial \Delta T_{LM}}{\partial \Delta T_1} = \frac{\ln \frac{\Delta T_1}{\Delta T_2} - \left(1 - \frac{\Delta T_2}{\Delta T_1}\right)}{\left(\ln \frac{\Delta T_1}{\Delta T_2}\right)^2} = 0.42$$

$$\frac{\partial \Delta T_{LM}}{\partial \Delta T_2} = - \frac{\ln \frac{\Delta T_1}{\Delta T_2} - \left(\frac{\Delta T_1}{\Delta T_2} - 1\right)}{\left(\ln \frac{\Delta T_1}{\Delta T_2}\right)^2} = 0.6$$

Therefore,

$$\begin{aligned} U_{\Delta T_{LM}} &= \pm \sqrt{(0.42 \times 1.45)^2 + (0.6 \times 1.05)^2} \\ &= \pm 0.87^\circ\text{C} \end{aligned}$$

The relative uncertainty for LMTD (in percentage) is estimated as

$$\frac{U_{\Delta T_{LM}}}{\Delta T_{LM}} \times 100 = \pm \frac{0.87}{11.51} \times 100 = \pm 7.61\%$$

A.3.3.2 Uncertainty estimation for average heat transfer rate

The average heat transfer rate (\dot{Q}) is used to evaluate the other heat transfer parameters such as Nusselt number, NTU, effectiveness, Colburn factor etc. The average heat transfer is obtained as

$$\dot{Q} = \frac{\dot{Q}_a + \dot{Q}_w}{2} = 2090.74\text{W} \quad (\text{A.56})$$

Absolute uncertainty of average heat transfer rate is estimated as

$$U_{\dot{Q}} = \pm \sqrt{\left(\frac{\partial \dot{Q}}{\partial \dot{Q}_a} U_{\dot{Q}_a}\right)^2 + \left(\frac{\partial \dot{Q}}{\partial \dot{Q}_w} U_{\dot{Q}_w}\right)^2} \quad (\text{A.57})$$

$$\text{Where } \frac{\partial \dot{Q}}{\partial \dot{Q}_a} = \frac{1}{2} = 0.5$$

$$\frac{\partial \dot{Q}}{\partial \dot{Q}_w} = \frac{1}{2} = 0.5$$

$$\begin{aligned} U_{\dot{Q}} &= \pm \sqrt{(0.5 \times 145.5)^2 + (0.5 \times 115.31)^2} \\ &= \pm 92.83\text{W} \end{aligned}$$

The relative uncertainty for average heat transfer rate (in percentage) is estimated as

$$\frac{U\dot{Q}}{\dot{Q}} \times 100 = \pm \frac{92.83}{2090.74} \times 100 = \pm 4.44\%$$

A.3.3.3 Uncertainty estimation for overall thermal resistance

The overall thermal resistance can be expressed in the following form for cross-flow heat exchanger:

$$R_{Total} = \frac{1}{UA} = \frac{F\Delta T_{LM}}{\dot{Q}} \quad (A.58)$$

Where, F = Correction factor which is considered here as a constant since the value of F is observed 0.98 throughout the experiment.

Therefore the absolute uncertainty of overall thermal resistance is estimated as

$$U_{R_{Total}} = \pm \sqrt{\left(\frac{\partial R_{Total}}{\partial \Delta T_{LM}} U_{\Delta T_{LM}}\right)^2 + \left(\frac{\partial R_{Total}}{\partial \dot{Q}} U_{\dot{Q}}\right)^2} \quad (A.59)$$

$$\frac{\partial R_{Total}}{\partial \Delta T_{LM}} = \frac{0.98}{\dot{Q}} = 0.000469$$

$$\frac{\partial R_{Total}}{\partial \dot{Q}} = -\frac{0.98\Delta T_{LM}}{(\dot{Q})^2} = 0.00000258$$

$$\begin{aligned} U_{R_{Total}} &= \pm \sqrt{(0.000469 \times 0.87)^2 + (0.00000258 \times 92.83)^2} \\ &= \pm 0.000473^\circ\text{C/W} \end{aligned}$$

The relative uncertainty for overall thermal resistance (in percentage) is estimated as

$$\frac{U_{R_{Total}}}{R_{Total}} \times 100 = \pm \frac{0.000473}{0.005394661} \times 100 = \pm 8.76\%$$

A.3.3.4 Uncertainty estimation for effectiveness

The effectiveness (ε) is expressed as

$$\varepsilon = \frac{\dot{Q}}{\dot{Q}_{max}} = \frac{\dot{Q}}{(\dot{m}c_p)_{min}\Delta T_{max}} \quad (A.60)$$

The minimum heat capacity rate ($\dot{m}c_p$) is found at water-side. The equation (4.18) becomes as

$$\varepsilon = \frac{\dot{Q}}{(\dot{m}c_p)_w (T_{a,i} - T_{w,i})} \quad (\text{A.61})$$

The absolute uncertainty for effectiveness is estimated as

$$U_\varepsilon = \pm \sqrt{\left(\frac{\partial \varepsilon}{\partial \dot{Q}} U_{\dot{Q}}\right)^2 + \left(\frac{\partial \varepsilon}{\partial \dot{m}_w} U_{\dot{m}_w}\right)^2 + \left(\frac{\partial \varepsilon}{\partial c_{p,w}} U_{c_{p,w}}\right)^2 + \left(\frac{\partial \varepsilon}{\partial T_{a,i}} U_{T_{a,i}}\right)^2 + \left(\frac{\partial \varepsilon}{\partial T_{w,i}} U_{T_{w,i}}\right)^2} \quad (\text{A.62})$$

$$\frac{\partial \varepsilon}{\partial \dot{Q}} = \frac{1}{(\dot{m}c_p)_w (T_{a,i} - T_{w,i})}$$

$$\frac{\partial \varepsilon}{\partial \dot{m}_w} = -\frac{\dot{Q}}{\dot{m}_w^2 c_{p,w} (T_{a,i} - T_{w,i})}$$

$$\frac{\partial \varepsilon}{\partial c_{p,w}} = -\frac{\dot{Q}}{\dot{m}_w c_{p,w}^2 (T_{a,i} - T_{w,i})}$$

$$\frac{\partial \varepsilon}{\partial T_{a,i}} = -\frac{\dot{Q}}{(\dot{m}c_p)_w (T_{a,i} - T_{w,i})^2}$$

$$\frac{\partial \varepsilon}{\partial T_{w,i}} = \frac{\dot{Q}}{(\dot{m}c_p)_w (T_{a,i} - T_{w,i})^2}$$

$$U_\varepsilon = 0.042$$

The relative uncertainty for effectiveness (in percentage) is estimated as

$$\frac{U_\varepsilon}{\varepsilon} \times 100 = \pm \frac{0.042}{0.81} \times 100 = \pm 5.2\%$$

A.3.3.5 Uncertainty estimation for NTU

The NTU is defined as

$$NTU = \frac{UA}{c_{min}} = \frac{UA}{(\dot{m}c_p)_w} \quad (\text{A.63})$$

The absolute uncertainty for NTU is estimated as

$$U_{NTU} = \pm \sqrt{\left(\frac{\partial NTU}{\partial UA} U_{UA}\right)^2 + \left(\frac{\partial NTU}{\partial \dot{m}_w} U_{\dot{m}_w}\right)^2 + \left(\frac{\partial NTU}{\partial c_{p,w}} U_{c_{p,w}}\right)^2} \quad (\text{A.64})$$

$$\frac{\partial NTU}{\partial UA} = \frac{1}{(\dot{m}c_p)_w} = 0.012$$

$$\frac{\partial NTU}{\partial \dot{m}_w} = -\frac{UA}{\dot{m}_w^2 c_{p,w}} = 111$$

$$\frac{\partial NTU}{\partial c_{p,w}} = -\frac{UA}{\dot{m}_w c_{p,w}^2} = 0.00053$$

$$U_\varepsilon = \pm \sqrt{(0.011 \times 12)^2 + (111 \times 0.0011)^2 + (0.00053 \times 0.95)^2}$$

$$= \pm 0.17$$

The relative uncertainty for effectiveness (in percentage) is estimated as

$$\frac{U_{NTU}}{NTU} \times 100 = \pm \frac{0.17}{2.18} \times 100 = \pm 7.78\%$$

A.3.4.1 Uncertainty estimation for air-side heat transfer coefficient

The air-side heat transfer coefficient (h_a) is evaluated from overall thermal resistance equation in the following form:

$$h_a = \frac{1}{\eta_a A_a (R_{Total} - R_w)} \quad (A.65)$$

The absolute uncertainty for liquid side thermal resistance is estimated as

$$U_{h_a} = \pm \sqrt{\left(\frac{\partial h_a}{\partial \eta_a} U_{\eta_a}\right)^2 + \left(\frac{\partial h_a}{\partial A_a} U_{A_a}\right)^2 + \left(\frac{\partial h_a}{\partial R_{total}} U_{R_{total}}\right)^2 + \left(\frac{\partial h_a}{\partial R_w} U_{R_w}\right)^2} \quad (A.59)$$

$$\frac{\partial h_a}{\partial \eta_a} = -\frac{1}{\eta_a^2 A_a (R_{Total} - R_w)}$$

$$\frac{\partial h_a}{\partial A_a} = -\frac{1}{A_a^2 \eta_a (R_{Total} - R_w)}$$

$$\frac{\partial h_a}{\partial R_{Total}} = -\frac{1}{\eta_a A_a (R_{Total})^2}$$

$$\frac{\partial h_a}{\partial R_w} = -\frac{1}{\eta_a A_a (R_w)^2}$$

$$U_{h_a} = \pm 2.15 \text{ W/m}^2 \cdot \text{°C}$$

The relative uncertainty for overall thermal resistance (in percentage) is estimated as

$$\frac{U_{h_a}}{h_a} \times 100 = \pm \frac{2.15}{25.64} \times 100 = \pm 8.38\%$$

A.3.4.2 Uncertainty estimation for air-side Nusselt number

The air-side Nusselt number is expressed as

$$Nu_a = \frac{h_a D_{h,a}}{k_a} \quad (\text{A.66})$$

Therefore the absolute uncertainty for air-side Nusselt number is estimated as

$$U_{Nu_a} = \pm \sqrt{\left(\frac{\partial Nu_a}{\partial h_a} U_{h_a}\right)^2 + \left(\frac{\partial Nu_a}{\partial D_{h,a}} U_{D_{h,a}}\right)^2 + \left(\frac{\partial Nu_a}{\partial k_a} U_{k_a}\right)^2} \quad (\text{A.67})$$

$$\frac{\partial Nu_a}{\partial h_a} = \frac{D_{h,a}}{k_a} = 0.130$$

$$\frac{\partial Nu_a}{\partial D_{h,a}} = \frac{h_a}{k_a} = 960.3$$

$$\frac{\partial Nu_a}{\partial k_a} = -\frac{h_a D_{h,a}}{k_a^2} = 125.5$$

$$U_{Nu_a} = \pm \sqrt{(0.130 \times 2.15)^2 + (960.3 \times 0.000003)^2 + (125.5 \times 0.00074)^2}$$

$$= \pm 0.29$$

The relative uncertainty for air-side Nusselt number (in percentage) is estimated as

$$\frac{U_{Nu_a}}{Nu_a} \times 100 = \pm \frac{0.29}{3.35} \times 100 = \pm 8.66\%$$

A.3.4.3 Uncertainty estimation for air-side Stanton number

The Stanton number is the function of heat transfer coefficient, mass velocity and specific heat as

$$St_a = \frac{h_a}{G_a c_{p,a}} \quad (\text{A.68})$$

The air-side mass velocity is expressed as

$$G_a = \frac{\dot{m}_a}{A_{min}} \quad (\text{A.69})$$

The absolute uncertainty of mass velocity of air-side is estimated as

$$U_{G_a} = \pm \sqrt{\left(\frac{\partial G_a}{\partial \dot{m}_a} U_{\dot{m}_a}\right)^2 + \left(\frac{\partial G_a}{\partial A_{min}} U_{A_{min}}\right)^2} \quad (\text{A.70})$$

$$\frac{\partial G_a}{\partial \dot{m}_a} = \frac{1}{A_{min}} = 14.10$$

$$\frac{\partial G_a}{\partial A_{min}} = -\frac{\dot{m}}{(A_{min})^2} = 63.62$$

$$\begin{aligned} U_{G_a} &= \pm \sqrt{(14.10 \times 0.005)^2 + (63.62 \times 0.000236)^2} \\ &= \pm 0.072 \end{aligned}$$

The relative uncertainty for air-side mass velocity (in percentage) is estimated as

$$\frac{U_{G_a}}{G_a} \times 100 = \pm \frac{0.072}{4.5} \times 100 = \pm 1.6\%$$

Therefore the absolute uncertainty for air-side Stanton number is estimated as

$$U_{St_a} = \pm \sqrt{\left(\frac{\partial St_a}{\partial h_a} U_{h_a}\right)^2 + \left(\frac{\partial St_a}{\partial G_a} U_{G_a}\right)^2 + \left(\frac{\partial St_a}{\partial c_{p,a}} U_{c_{p,a}}\right)^2} \quad (\text{A.71})$$

$$\frac{\partial St_a}{\partial h_a} = \frac{1}{G_a c_{p,a}} = 0.00022$$

$$\frac{\partial St_a}{\partial G_a} = -\frac{h_a}{G_a^2 c_{p,a}} = -0.00126$$

$$\frac{\partial St_a}{\partial c_{p,a}} = -\frac{h_a}{G_a c_{p,a}^2} = -0.0000056$$

$$\begin{aligned} U_{St_a} &= \pm \sqrt{(0.00022 \times 2.31)^2 + (-0.00126 \times 0.072)^2 + (-0.0000056 \times 0.045)^2} \\ &= \pm 0.00052 \end{aligned}$$

The relative uncertainty for air-side Stanton number (in percentage) is estimated as

$$\frac{U_{St_a}}{St_a} \times 100 = \pm \frac{0.00052}{0.005651583} \times 100 = \pm 9.2\%$$

A.3.4.4 Uncertainty estimation for air-side Colburn factor

The air-side Colburn factor is evaluated by the following expression:

$$j_a = St_a Pr_a^{\frac{2}{3}} \quad (A.72)$$

$$U_{j_a} = \pm \sqrt{\left(\frac{\partial j_a}{\partial St_a} U_{St_a}\right)^2 + \left(\frac{\partial j_a}{\partial Pr_a} U_{Pr_a}\right)^2} \quad (A.73)$$

$$\frac{\partial j_a}{\partial St_a} = Pr_a^{\frac{2}{3}} = 0.798$$

$$\frac{\partial j_a}{\partial Pr_a} = \frac{2}{3} St_a Pr_a^{-\frac{1}{3}} = 0.0043$$

$$U_{j_a} = \pm \sqrt{(0.798 \times 0.00052)^2 + (0.0043 \times 0.02)^2}$$

$$= \pm 0.00042$$

The relative uncertainty for air-side Stanton number (in percentage) is estimated as

$$\frac{U_{j_a}}{j_a} \times 100 = \pm \frac{0.00042}{0.004510228} \times 100 = \pm 9.3\%$$

A.3.4.5 Uncertainty estimation for air-side friction factor

The friction factor f_a is evaluated on the following equation proposed by Kays and London, 1984, for flow to fin –tube banks:

$$f_a = \left(\frac{A_{min,a}}{A_a}\right) \left(\frac{\rho_{a,b}}{\rho_{a,i}}\right) \left[\left(\frac{2\Delta P_a \rho_{a,i}}{G_a^2} - (1 + \sigma_a^2)\right) \left(\frac{\rho_{a,i}}{\rho_{a,o}} - 1\right)\right] \quad (A.74)$$

The absolute uncertainty for air-side friction factor is estimated as

$$U_{f_a} = \pm \sqrt{\left(\frac{\partial f_a}{\partial A_{min,a}} U_{A_{min,a}}\right)^2 + \left(\frac{\partial f_a}{\partial A_a} U_{A_a}\right)^2 + \left(\frac{\partial f_a}{\partial \rho_{b,a}} U_{\rho_{b,a}}\right)^2 + \left(\frac{\partial f_a}{\partial \rho_{a,i}} U_{\rho_{a,i}}\right)^2 + \left(\frac{\partial f_a}{\partial \rho_{a,o}} U_{\rho_{a,o}}\right)^2 + \left(\frac{\partial f_a}{\partial \Delta P_a} U_{\Delta P_a}\right)^2 + \left(\frac{\partial f_a}{\partial G_a} U_{G_a}\right)^2 + \left(\frac{\partial f_a}{\partial \sigma_a} U_{\sigma_a}\right)^2} \quad (A.75)$$

$$\frac{\partial f_a}{\partial A_{min,a}} = \left(\frac{1}{A_a}\right) \left(\frac{\rho_{a,b}}{\rho_{a,i}}\right) \left[\left(\frac{2\Delta P_a \rho_{a,i}}{G_a^2} - (1 + \sigma_a^2)\right) \left(\frac{\rho_{a,i}}{\rho_{a,o}} - 1\right)\right]$$

$$\frac{\partial f_a}{\partial A_a} = -\left(\frac{A_{min,a}}{A_a^2}\right) \left(\frac{1}{\rho_{i,a}}\right) \left[\left(\frac{2\Delta P_a \rho_{a,i}}{G_a^2} - (1 + \sigma_a^2)\right) \left(\frac{\rho_{a,i}}{\rho_{a,o}} - 1\right)\right]$$

$$\frac{\partial f_a}{\partial \rho_{b,a}} = \left(\frac{A_{min,a}}{A_a}\right) \left(\frac{1}{\rho_{a,i}}\right) \left[\left(\frac{2\Delta P_a \rho_{a,i}}{G_a^2} - (1 + \sigma_a^2)\right) \left(\frac{\rho_{a,i}}{\rho_{a,o}} - 1\right)\right]$$

$$\frac{\partial f_a}{\partial \rho_{i,a}} = \left(\frac{A_{min,a}}{A_a}\right) \left(\left(\left(-\frac{\rho_{a,b}}{\rho_{a,i}^2}\right) \left[\left(\frac{2\Delta P_a \rho_{a,i}}{G_a^2} - (1 + \sigma_a^2)\right) \left(\frac{\rho_{a,i}}{\rho_{a,o}} - 1\right)\right]\right) - \left(\frac{\rho_{a,b}}{\rho_{a,i}}\right) \left[\left(\frac{2\Delta P_a \rho_{a,i}}{G_a^2} - (1 + \sigma_a^2)\right) \left(\frac{\rho_{a,i}}{\rho_{a,o}} - 1\right)\right]\right)$$

$$\frac{\partial f_a}{\partial \rho_{o,a}} = (1 + \sigma_a^2) \left(\frac{A_{min,a}}{A_a}\right) \left(\frac{\rho_{b,a}}{\rho_{a,o}^2}\right)$$

$$\frac{\partial f_a}{\partial \Delta P_a} = \left(\frac{A_{min,a}}{A_a}\right) \left(\frac{\rho_{a,b}}{\rho_{a,i}}\right) \left(\frac{2\rho_{a,i}}{G_a^2}\right)$$

$$\frac{\partial f_a}{\partial G_a} = \left(\frac{A_{min,a}}{A_a}\right) \left(\frac{\rho_{a,b}}{\rho_{a,i}}\right) \left(-\frac{4\Delta P_a \rho_{a,i}}{G_a^3}\right)$$

$$\frac{\partial f_a}{\partial \sigma_a} = -2\sigma_a^2 \left(\frac{A_{min,a}}{A_a}\right) \left(\frac{\rho_{a,b}}{\rho_{a,i}}\right) \left(\frac{\rho_{a,i}}{\rho_{a,o}} - 1\right)$$

Putting all numerical values in the Eq. (A.75), the uncertainty for air-side friction factor is estimated as

$$U_{f_a} = \pm 0.0042$$

The relative uncertainty for air-side Stanton number (in percentage) is estimated as

$$\frac{U_{f_a}}{f_a} \times 100 = \pm \frac{0.0042}{0.070085326} \times 100 = \pm 6\%$$

A.4 Overall uncertainties range for all operating conditions

The uncertainties are estimated accordingly for all operating conditions and they are mentioned in the Table A.3.

TableA.3: Overall Experimental Uncertainty

Key Parameters	Range of uncertainties in percentage of mean value
ΔP_a	5.69 - 5.21
Re_a	3.96 - 3.01
\dot{Q}_a	7.42 - 6.50
h_a	8.74 - 8.01
Nu_a	8.89 - 8.11
j_a	9.61 - 9.01
f_a	6.57 - 5.80
Re_w	5.68 - 5.01
\dot{Q}_w	5.93 - 5.09
\dot{Q}	5.32 - 4.06
h_w	8.53 - 7.65
Nu_w	8.89 - 8.01
R_{Total}	8.94 - 8.22
ε	5.54 - 4.96
NTU	8.91 - 7.34

REFERENCES

- ASME, 1991. An American National Standard, Performance Test Code (PTC) 30-1991, Air cooled heat exchangers, New York.
- Bier, W., 1990. Manufacturing and testing of compact micro heat exchangers with high volumetric heat transfer coefficients. American Society of Mechanical Engineers, dynamic Systems and Control Division (Publication) DSC 19, 189-197.
- Bowman, R.A., Mueller, A.C., Nagle, W.M., 1940. Mean temperature difference in design. Transactions of the ASME 62, 283-294.
- Cao, H., Chen, G., and Yuan, Q., 2010. Thermal performance of crossflow microchannel heat exchangers. Ind. Eng. Chem. Res. 49, 6215-6220.
- Çengel, Y.A., Ghajar, A.J. 2010. Heat and Mass Transfer: Fundamentals and Application, p.374--403. Fourth ed. McGraw Hill, New York.
- Coleman, H.W. and Steele, W.G. 1989. Experimentation and uncertainty analysis for engineers. John Wiley & Sons: New York.
- Dasgupta, E. S., Siddique, F.A. and Fartaj, A. 2011. Experimental study on air-side heat transfer & fluid flow characteristics of microchannel heat exchanger. Published by the Society of the Automotive Engineers Inc.PA, DOI: 10.4271/2011-01-1166. (Originally presented at the SAE 2011 World Congress, April 14, 2011 Detroit, MI, USA, SAE Paper # 2011-01-1166.
- Dasgupta, E. S., Siddique, F.A., Quaiyum, A, Serina Al-Obaidi, S. and Fartaj, A. 2011. Experimental Study on Air Cooling via a Multiport Mesochannel Cross-Flow Heat Exchanger. ASME 9th International Conference on Nanochannels, Mesochannels, and Minichannels (ICNMM), Paper # ICNMM2011-58257, Edmonton, Alberta,

CANADA, June 19-22, 2011.

- Dittus, F.W. and Boelter, L.M.K., 1930. Heat transfer in automobile radiators of the Tubular types. University of California Publication Engineering 12,443.
- Dong, J., Jiangping, C., Zhijiu, C., Yimin, Z., Wenfeng, Z., 2007. Heat transfer and pressure drop correlations for the wavy fin and flat tube heat exchangers. J. Applied Thermal Engineering 27, 2066-2073.
- Dong, J., Jiangping, C., Zhijiu, C., Yimin, Z., 2007b. Air-side thermal hydraulic performance of offset strip fin aluminum heat exchangers. Applied Thermal Engineering 27, 306-313.
- Editorial, 1991. J. Fluids Engineering: Policy on reporting uncertainties in experimental measurements and results. Transactions of the ASME, J. Fluids Engineering 113, 313-314.
- Editorial, 1993. J. Heat Transfer: Policy on reporting uncertainties in experimental measurements and results. Transactions of the ASME, J. Heat Transfer 115, 5-6.
- El-Shaboury, A.M.F., Ormiston, S. J., 2005. Analysis of laminar forced convection of air cross-flow in in-line tube banks with non-square arrangements. Numerical Heat Transfer, Part A, 48, 99-126.
- Figliola, R.S. and Beasley, D.E. 1995. Theory and design for mechanical measurements, p.171-209. 2nd Edition. John Wiley & Sons, Inc.: New York.
- Gnielinski, V. 1976. New equation for heat and mass transfer in turbulent pipe and channel flow. Int. J. of Chemical Engineering 16(2), 359-368.
- Harris, C., Despa, M., Kelly, K., 2000. Design and fabrication of a cross flow micro heat exchanger. J. Microelectromechanical Systems 9, 502-508.

- Hetsroni, G., Mosyak, A., Pogrebnyak, E., Yarin, L.P., 2005. Heat transfer in micro-channels: Comparison of experiments with theory and numerical results. I. J. of Heat and Mass Transfer 48, 5580-5601.
- Incropera, F.P., DeWitt, D.P.2002. Introduction to Heat Transfer.p.347- 350.Fourth ed. John and Sons, New York.
- Kakaç, S., Liu, H., 2002. Heat exchangers: selection, rating, and thermal design. p.84-85,349- 360, CRC Press, New York.
- Kandlikar, S.G., Grande, W.J., 2004. Evaluation of single phase flow in mesochannels for high heat flux chip cooling-thermohydraulic performance enhancement and fabrication technology. Heat Transfer Engineering 25, 5-16.
- Kandlikar, S.G., Upadhye, H.R., 2005. Extending the heat flux limit with enhanced mesochannels in direct single-phase cooling of computer chips. IEEE SEMI-THERM Symposium 21, 8-15.
- Kays, W.M., London, A.L., 1984. Compact Heat Exchangers. p.8-9. 3rd. ed. McGraw-Hill, New York.
- Khan, M.G., Fartaj, A., 2010. Heat Transfer Experiments of Ethylene Glycol-Water Mixture in Multi-Port Serpentine Meso-Channel Heat Exchanger Slab, 3rd Joint US-European Fluids Engineering Summer Meeting (FEDSM) and 8th International Conference on Nanochannels, Mesochannels, and Minichannels (ICNMM). ASME, Montreal, Quebec, CANADA.
- Khan,M.G. and Fartaj, A., “Experiments of ethylene glycol-water mixture in multi-port circular straight microchannel slab,” Proceedings of the Society of Automotive

- Engineers(SAE) World Congress 2010, Paper# 2010-01-0326, Detroit, MI, USA, April 13-15,2010.
- Kline, S.J. and McClintock, F.A. 1953. Describing uncertainties in single-sample side experiments. *Mechanical Engineering* 75, 3-8.
- Li,J., Wang, S. and Zhang, W., 2011. Air-side thermal hydraulic performance of an integrated fin and integrated fin and micro-channel heat exchanger. *Energy Conversion and Management* 52,983-989.
- Luo, L., Fan, Y., Tondeur, D., 2007. Heat Exchanger: From Micro - to Multi - Scale Design Optimization. *I. J. Energy Research* 31, 1266.
- Nuntaphan, A., Kiasiriroat, T., Wang, C.C., 2005. Air side performance at low Reynolds number of cross-flow heat exchanger using crimped spiral fins. *I. Communications in Heat and Mass Transfer* 32, 151.
- Moffat, R.J.1998. Describing the uncertainties in experimental results. *Int.J. of Thermal Fluid Science* 1, 3-7.
- Owhaib, W., Palm, B., 2004. Experimental investigation of single-phase convective heat transfer in circular mesochannels. *J. Experimental Thermal and Fluid Science* 28, 105-110.
- Paeng, J.G., Kim, K.H. and Yoon, Y.H. 2009. Experimental measurement and numerical computation of the air side convective heat transfer coefficients in a plate fin-tube heat exchanger. *J. of Mechanical Science and Technology*, 23, 536-543.
- Park, Y.G., Jacobi, A.M., 2009. The Air-Side thermal-hydraulic performance of flat-tube heat exchangers heat exchangers with louvered, wavy, and plain fins under dry and wet conditions. *J. Heat Transfer* 131, 1-13.

- Petukhov, B.S. 1970. Heat transfer and friction in turbulent pipe flow with variable physical properties. *Advances in Heat Transfer* 6, 503-564.
- Ramshaw, C., 1995. *Process Intensification in the Chemical Industry*. Mechanical Engineering Publications Ltd, London.
- Rugh, J.P., Pearson, J.T., Rarnadhyani, S., 1992. A study of a very compact heat exchanger used for passenger compartment heating in automobiles. *Compact Heat Exchangers for Power and Process Industries*, Heat Transfer Division. ASME 201, 15-24.
- Schmidt, T.E. 1949. Heat transfer calculations for extended surfaces. *Refrigerating Engineering* 57:351-357.
- Siddique, F.A., Dasgupta, E. S. and Fartaj, A.2011. Experimental investigation of air-side heat transfer and fluid flow performances of multi-port serpentine crossflow mesochannel heat exchanger. *Int. Journal of Heat and Fluid Flow* (under review), Paper # HFF – D-11- 00055.
- Shah, R.K., Sekulic, D.P., 2003. Fundamentals of Heat Exchanger Design p.446-448. John Willy & Sons, New Jersey.
- Steinke, M. E., and Kandlikar,S.G.2004. Review of single-phase heat transfer enhancement techniques for application in microchannels, minichannels and microdevices. *Int. J. of Heat Tech.* 22, 3-11.
- Taler, D., 2005. Prediction of heat transfer correlations for compact heat exchangers. *I. J. of Heat and Mass Transfer* 69, 137-150.
- Tang, S. and Yang, K.T., 2005. Thermal performance of a single-row fin-and-tube heat exchanger. *Int. J. of Thermal Science* 14, 172-180.
- Tang, L.H., Zeng, M.and Wang, Q.W., 2009. Experimental and numerical investigation on

- air--side performance of fin-and-tube heat exchangers with various fin patterns. *Experimental Thermal and Fluid Science* 33, 818 – 827.
- Tao, Y.B., He, Y.L., Hung, J., Wu, Z.G., Tao, W.Q., 2007. Numerical study of local heat transfer coefficient and fin efficiency of wavy fin-and-tube heat exchangers. *Int. J. Thermal Sciences* 46, 768-778.
- Tian, L., He, Y., Hung, J., Tao, Y., Tao, W., 2009. A comparative study on the air-side performance of wavy fin-and-tube heat exchanger with punched delta winglets in staggered and in-line arrangements. *Int. J. Thermal Sciences* 48, 1765-1776.
- Tuckerman, D.B. and Pease 1981. High-performance heat sinking for VLSI. *IEEE electron device letters* 2, 126-129.
- Wang, C.C., 2000. Recent progress on the air-side performance of fin-and-tube heat exchangers. *I. J. Heat Exchangers* 1, 49-76.
- Wang, C.C. and Chi, K.Y., 2000. Heat transfer and friction characteristics of plain fin-and-tube heat exchangers, part I: new experimental data. *Int. J. of Heat and Mass Transfer* 43, 2681 – 2691.
- Wang, C.C., Webb, R.L., Chi, K.Y., 2000. Data reduction for air-side performance of fin-and-tube heat exchangers. *J. Experimental Thermal and Fluid Science* 21, 218-226.
- Zhang, Li.Z., 2008. Total heat recovery: heat and moisture recovery from ventilation air, p.1-6. Nova Science Publishers, Inc., New York.

VITA AUCTORIS

- 1963 Born in Bagerhat, Bangladesh
- 1979 Completed 10 years school education from Bagerhat High School, Bagerhat, Bangladesh
- 1981 Completed 2 years higher secondary college education from Government P.C. College, Bagerhat, Bangladesh
- 1987 Obtained the Degree of Bachelor of Science in Mechanical Engineering in May from Bangladesh Institute of Technology, Khulna, Bangladesh (Presently Khulna University of Engineering and Technology)
- 1987-2007 Involved in professional work as a Mechanical Engineer
- 2010 Received the Degree of Master of Engineering (Mechanical Engineering) from the University of Windsor, ON, Canada on June 18
- 2011 A candidate for the Degree of Master of Applied Science (M.A.Sc.) in Mechanical Engineering at the University of Windsor, ON, Canada